JOURNAL OF GEOPHYSICAL RESEARCH: SPACE PHYSICS, VOL. 118, 7119–7150, doi:10.1002/jgra.50557, 2013

Physics-based solar wind driver functions for the magnetosphere: Combining the reconnection-coupled MHD generator with the viscous interaction

Joseph E. Borovsky [1,2,3]

Received 27 January 2013; revised 30 August 2013; accepted 7 September 2013; published 20 November 2013.

[1] Driver functions for the Earth's magnetosphere-ionosphere system are derived from physical principles. Two processes act simultaneously: a reconnection-coupled MHD generator $\mathscr{G}$ and a viscous interaction. $\mathscr{G}$ accounts for the dayside reconnection rate, the length of the reconnection X line, and current saturation limits for the solar wind generator. Two viscous drivers are derived: Bohm viscosity $\mathscr{B}$ and the freestream-turbulence effect $\mathscr{T}$. A problematic proxy effect is uncovered wherein the viscous driver functions also describe the strength of reconnection. Two magnetospheric-driver functions written in terms of upstream solar wind parameters are constructed: $\mathscr{G}+\mathscr{B}$ and $\mathscr{G}+\mathscr{T}$. The driver functions are tested against seven geomagnetic indices. The reaction of the geomagnetic indices to $\mathscr{G}+\mathscr{B}$ and $\mathscr{G}+\mathscr{T}$ is nonlinear: Nonlinear versions of the driver functions are supplied. Applying the driver functions at multiple time steps yields correlation coefficients of ~85% with the *AE* and *Kp* indices; it is argued that multiple time stepping removes high-frequency uncorrelated signal from the drivers. Autocorrelation-function analysis shows strong 1 day and 1 year periodicities in the *AE* index, which are not in the solar wind driver functions; correspondingly, high-pass and low-pass filtering finds uncorrelated signal at 1 day and 1 year timescales. Residuals (unpredicted variance) between the geomagnetic indices and the driver functions are analyzed: The residuals are anticorrelated with the solar wind velocity, the solar $F_{10.7}$ radio flux, and the solar wind current saturation parameter. Removing diurnal, semiannual, and annual trends from the indices improves their correlation with the solar wind driver functions. Simplified versions of the driver functions are constructed: The simplified drivers perform approximately as well as the full drivers.

Citation: Borovsky, J. E. (2013), Physics-based solar wind driver functions for the magnetosphere: Combining the reconnection-coupled MHD generator with the viscous interaction, *J. Geophys. Res. Space Physics*, *118*, 7119–7150, doi:10.1002/jgra.50557.

1. Introduction

[2] The purpose of this report is to develop a physics-based driver function to describe the coupling of the solar wind to the Earth's magnetosphere in terms of solar wind parameters. A driver function $\mathscr{D}(t)$ that is a function of the time t will be obtained, where the time dependence comes from the time dependence of solar and solar wind parameters such as the plasma velocity $u_{sw}(t)$, the plasma number density $n_{sw}(t)$, the interplanetary magnetic field (IMF) clock angle $\theta_{\text{clock}}(t)$, the solar 10.7 cm radio flux $F_{10.7}(t)$, etc. Hence, $\mathscr{D}(t)=\mathscr{D}(u_{sw}(t), n_{sw}(t), \theta_{\text{clock}}(t), F_{10.7}(t),\ldots)$.

[3] It is believed that there are two main physical processes that couple the solar wind to the magnetosphere-ionosphere system: a reconnection-based interaction [*Dungey*, 1961; *Sonnerup*, 1974] and a viscous-type interaction [*Axford*, 1964; *Farrugia et al*., 2001]. The reconnection-based driver is thought to be the dominant processes, with the viscous interaction perhaps being dominant under northward IMF when the total coupling is low [*Mozer*, 1984; *Mozer et al*., 1994; *Tsurutani and Gonzalez*, 1995].

[4] Derivations of those two physical processes are presented, with the two processes combined into a single solar wind driver function for the magnetosphere. To derive the reconnection-coupled MHD generator, (1) a new locally controlled reconnection picture will be used [*Cassak and Shay*, 2007; *Birn et al*., 2008, 2010] to calculate the dayside reconnection rate combined with (2) an estimate of the length of the dayside X line obtained from global MHD simulations, combined with (3) some MHD generator current saturation physics. For the viscous interaction, new derivations appropriate to the shocked flow of the magnetosheath around the magnetosphere will be presented. The locally controlled reconnection picture [*Borovsky*, 2008a, 2008b,

[1]Space Science Institute, Boulder, Colorado, USA.
[2]Atmospheric, Oceanic and Space Sciences, College of Engineering, University of Michigan, Ann Arbor, Michigan, USA.
[3]Visiting professor at Department of Physics, Lancaster University, Lancaster, UK.

Corresponding author: J. E. Borovsky, Space Science Institute, Ste. 205, 4750 Walnut St., Boulder, CO 80301, USA. (jborovsky@spacescience.org)

2169-9380/13/10.1002/jgra.50557

2013; J. E. Borovsky, The solar wind electric field does not control the dayside reconnection rate, submitted to *Journal of Geophysical Research*, 2013] utilized in point 1 above is in contrast to the commonly used boundary condition picture [*Axford*, 1969] in which the solar wind electric field is taken to be the driver of dayside reconnection [*Wygant et al*., 1983; *Gonzalez*, 1990].

[5] The quality of a solar wind driver function for the magnetosphere will be gauged by its ability to describe the variance of geomagnetic activity indices [e.g., *Reiff et al*., 1981; *Baker et al*., 1981; *Reiff and Luhmann*, 1986; *Baker*, 1986; *Finch and Lockwood*, 2007; *Newell et al*., 2007, 2008]. Here correlations between the temporal variance of the driver functions and the temporal variance of seven geomagnetic indices will be used for guidance. The seven indices that will be used are the auroral electrojet indices *AE*, *AU*, and *AL* [*Rostoker*, 1972], the polar cap index PCI [*Troshichev et al*., 2000], the planetary index *Kp* [*Rostoker*, 1972], the midnight boundary index MBI [*Gussenhoven et al*., 1983], and the pressure-corrected *Dst* index *Dst** [*Borovsky and Denton*, 2010a]. When correlating the driver functions with geomagnetic indices, the best correlations are obtained with time lags between the solar wind measurements and the geomagnetic indices. For the seven indices used, the time legs are 1 h for the *AE*, 1 h for *AL*, 1 h for *AU*, 0 h for PCI, 1 h for *Kp*, 1 h for MBI, and 2 h for *Dst**. (Note the optimal time lag for PCI is a few minutes, but to hourly accuracy, the lag is 0 h.) When correlating the viscous driver functions with geomagnetic indices, the best correlations are obtained with the same set of time lags for the seven indices. These time lags are interpreted as response times for the magnetosphere to the driving by the solar wind, with the response times being the same (to within 1 h accuracy) for the reconnection-coupled MHD generator driving as for the viscous driving. For the correlations, hourly averaged values of the indices and hourly averaged solar wind parameters from OMNI2 [*King and Papitashvili*, 2005] will be used. OMNI2 hourly averaged data are a standard for most contemporary statistical studies of solar wind driving [e.g., *Newell et al*., 2007, 2008; *Balikhin et al*., 2010; *Boynton et al*., 2011; *Singh and Badruddin*, 2012; *Guo et al*., 2012; *Milan et al*., 2012; *Luo et al*., 2013], particularly when very long time intervals are utilized [cf. *McPherron et al*., 2013].

[6] Note that the objective is not to obtain the most accurate solar wind driver function for the prediction of geomagnetic indices but rather to obtain a quantified physical picture of solar wind/magnetosphere coupling. Adjustable tuning parameters could improve the performance of the driver functions, but tuning parameters will not be used. Note that there are issues concerning the use of correlations to gauge the quality of the solar wind driver functions for the magnetosphere:

[7] 1. The accuracy of knowing the parameters of the solar wind that hits the Earth inferred from measurements from an upstream solar wind monitor that is off the Sun-Earth line is not perfect; and the accuracy of using geomagnetic indices as a measure of the strength of solar wind/magnetosphere coupling is also less than perfect.

[8] 2. Correlation coefficients quantify how much of the variance of a function can be predicted by the variance of the driver function: With many solar wind parameters strongly correlated with each other, there are physics-versus-mathematics issues in the ability to predict variance. For example, the linear correlation coefficient between hourly values of $u_{sw}B_{\text{south}}$ in the solar wind and hourly values of the *AE* index is +0.626 whereas the linear correlation coefficient between hourly values of $u_{sw}+75B_{\text{south}}$ and *AE* is +0.730 (with u_{sw} in units of km/s and B_{south} in units of nT): Is $u_{sw}+B_{\text{south}}$ a better physical description of solar wind/magnetosphere coupling or does $u_{sw}+B_{\text{south}}$ have a better ability to describe variance in the solar wind and in the *AE* index?

[9] 3. Owing to similarities in their functional forms we will find that the viscous coupling functions are good proxies for the strength of the reconnection-coupled generator, and it is likely that the reconnection-based driving function is also describing the viscous interaction.

[10] Driver functions for the magnetosphere that combine the reconnection-coupled MHD generator plus the viscous interaction are the goal [cf. *Borovsky and Funsten*, 2003a; *Newell et al*., 2008]. The solar wind driver functions here will be derived from physical principles.

[11] This paper is organized as follows. In section 2 the reconnection-coupled MHD generator $\mathscr{G}$ is derived from an estimate of the dayside local reconnection rate, an estimate of the length of the dayside reconnection X line, and a factor that accounts for the quality of the MHD generator. In section 3 two expressions are derived for the viscous interaction between the supersonic solar wind and the magnetosphere based on Bohm viscosity $\mathscr{B}$ and on the freestream-turbulence effect $\mathscr{F}$. In section 4 the reconnection-coupled MHD generator and the Bohm and freestream viscous interactions are combined to produce two solar wind driver functions $\mathscr{G}+\mathscr{B}$ and $\mathscr{G}+\mathscr{F}$ for the magnetosphere, and the properties of those driver functions are studied via their relationships with seven geomagnetic indices. That study involves analysis of correlations, of low-pass and high-pass filtering, of autocorrelation functions, of multi time step drivers, of temporal averaging, of residual errors, and of diurnal and annual trends in the indices. For easier use, simplified mathematical versions $\mathscr{D}_{\mathscr{G}+\mathscr{B}}$ and $\mathscr{D}_{\mathscr{G}+\mathscr{B}}$ of the solar wind driver functions $\mathscr{G}+\mathscr{B}$ and $\mathscr{G}+\mathscr{F}$ are given in section 5. In section 6 physical processes that are missing from the derivations of the solar wind driver functions for the magnetosphere are enumerated and critical work that is needed is identified. The results are summarized in section 7.

2. The Reconnection-Coupled MHD Generator

[12] Magnetic field line reconnection at the dayside magnetopause magnetically connects the MHD generator of the moving solar wind/magnetosheath plasma to the Earth [cf. *Goertz et al*., 1993]. After becoming magnetically connected, the moving plasma drives currents into the polar ionospheres and transports magnetic flux from the dayside magnetosphere to the nightside magnetosphere, both processes driving convection in the magnetosphere-ionosphere system. Changes in the intensity of currents driven (1) directly by the solar wind, (2) by magnetospheric convection, and (3) by changes in the morphology of the magnetosphere are sensed by ground-based magnetometers to produce various geomagnetic indices.

[13] The amount of coupling of the solar wind to the Earth is proportional to the total reconnection rate, which is the local reconnection rate integrated over the length of the dayside reconnection X line. Sometimes (typically when the solar wind Alfven speed is high) the solar wind plasma

has difficulty supplying electrical current to the ionosphere to which it is magnetically connected [*Lavraud and Borovsky*, 2008; *Borovsky et al.*, 2009], leading to the familiar polar cap potential saturation [e.g., *Wygant et al.*, 1983; *Reiff and Luhmann*, 1986; *Weimer et al.*, 1990]. To account for this, the mathematical formulation of the generator must include a generator quality factor. The mathematical expression for the reconnection coupled MHD generator $\mathscr{G}$ is of the form:

$$\mathscr{G} = (\text{local reconnection rate}) \times (\text{length of X line}) \cdot (\text{generator quality}) \quad (1)$$

[14] In sections 2.1–2.3 mathematical expressions for (1) the local reconnection rate, (2) the effective length of the dayside X line, and (3) the quality of the MHD generator will be derived.

2.1. The Dayside Reconnection Rate

[15] In a collisionless plasma, the rate of magnetic reconnection is controlled by the local plasma parameters at the reconnection site: local Alfven speeds and local magnetic field strengths. For antiparallel reconnection between asymmetric plasmas like the magnetosphere and magnetosheath, the rate is given by the Cassak-Shay equation [*Cassak and Shay*, 2007; *Birn et al.*, 2008, 2010]:

$$R_{CS} = \left(0.1/\pi^{1/2}\right) B_m{}^{3/2} B_s{}^{3/2} / \left\{ (B_m\rho_s + B_s\rho_s)^{1/2} (B_m + B_s)^{1/2} \right\} \quad (2)$$

where B and ρ are the magnetic field strength and mass density of the two plasmas and where the subscripts "m" and "s" denote the magnetospheric plasma and magnetosheath plasma, respectively. The factor 0.1 in expression (2) is a geometric factor representing the angular aspect ratio between inflow and outflow at the reconnection site [cf. *Parker*, 1979]: It is chosen to be 0.1 to match the standard result that when the two plasmas are asymmetric ($B_m = B_s$ and $\rho_m = \rho_s$) that $R = 0.1\ v_A B$ [cf. *Borovsky and Hesse*, 2007; *Birn et al.*, 2008]. In addition to a magnetic clock angle dependence which is not in expression (2), four fundamental plasma parameters determine the dayside reconnection rate: B_m, B_s, ρ_m, and ρ_s. Whatever controls those four plasma parameters at the magnetopause controls the reconnection rate between the solar wind and the magnetosphere.

[16] *Borovsky* [2008a] developed a prescription to express three of those four parameters (B_m, B_s, and ρ_s) in terms of upstream solar wind parameters and from the Cassak-Shay equation the derived a "rudimentary" reconnection rate expression R_1 for the magnetosphere. *Borovsky* [2013] followed that prescription and accounted for the twist of the X line orientation in asymmetric reconnection to derive a more correct expression R_2 for the local reconnection rate. Since the mass density ρ_m of the dayside magnetosphere is not easily parameterized in terms of upstream solar wind parameters [*Borovsky et al.*, 2013], ρ_m is taken to be 0 in the derivation of R_2. Equations (30)–(30) of *Borovsky* [2013] give

$$R_2 = 0.8\pi^{1/2} m_p{}^{1/2} n_{sw}{}^{1/2} u_{sw}{}^2 \left(1 + 0.5 M_{ms}{}^{-2}\right) C^{-1/2} (gh)^{3/2} / \left\{ \chi g^{1/2} (g\chi + h)^{1/2} \right\} \quad (3)$$

[17] In expression (3),

$$\chi = (1 + \beta_s)^{1/2} \quad (4a)$$

$$\beta_s = (M_A/6)^{1.92} \quad (4b)$$

$$C = C_\perp \sin^2\theta_{Bn} + C_{||}\left(1 - \sin^2\theta_{Bn}\right) \quad (4c)$$

$$C_\perp = \left\{ 2.44 \times 10^{-4} + [1 + 1.38 \log_e(M_A)]^{-6} \right\}^{-1/6} \quad (4d)$$

$$C_{||} = 4/\left(1 + 3M_s{}^{-2}\right) \quad (4e)$$

$$M_A = u_{sw}/v_A \quad (4f)$$

$$M_s = u_{sw}/C_s \quad (4g)$$

$$M_{ms} = u_{sw}/\left(v_A{}^2 + C_s{}^2\right)^{1/2} \quad (4h)$$

$$g = \sin(\alpha) \quad (4i)$$

$$h = \sin(\theta_{\text{clock}} - \alpha) \quad (4j)$$

$$\alpha \approx \theta/2 - 15^\circ \left(1 - (1 + \chi)^{-1/2}\right) \sin(\theta_{\text{clock}}) \quad (4k)$$

where m_p is the proton mass, θ_{clock} is the IMF clock angle with respect to the Earth's dipole, θ_{Bn} is the angle of the IMF relative to the Sun-Earth line, n_{sw} and u_{sw} are the upstream solar wind number density and velocity, v_A is the Alfven speed in the solar wind upstream of the bow shock, $C_s = (\gamma k_B (T_i + T_e)/m_p)^{1/2}$ is the sound speed in the solar wind upstream of the bow shock, α is the angle of orientation of the reconnection X line from the direction of the magnetospheric magnetic field, and $C_\perp$ and $C_{||}$ are the density compression ratios of the quasi-perpendicular and quasi-parallel bow shock. The solar wind upstream Mach numbers in expressions (4a)–(4k) are the Alfven Mach number M_A, the sonic Mach number M_s, and the magnetosonic Mach number M_{ms}. In expressions (4a)–(4k), β_s is the plasma β value of the magnetosheath near the magnetopause.

[18] Expression (4b) $\beta_s = (M_A/6)^{1.92}$ is central to evaluating χ (expression (4a)), whose value strongly affects the reconnection rate (expression (3)). The expression $\beta_s = (M_A/6)^{1.92}$ will be used repeatedly in the latter sections of this report in pressure balance arguments. This expression [*Borovsky*, 2008a, equation (7)] was obtained by parameterizing the β_s value of the magnetosheath plasma near the nose of the magnetosphere in a series of BATSRUS [*De Zeeuw et al.*, 2000; *Ridley et al.*, 2010] global MHD simulations over a range ($M_A = 1.9$–16.2) of solar wind Alfven Mach numbers [cf. *Borovsky*, 2008a, Figure 3]. In section 2.2 a series of Lyon-Fedder-Mobarry (LFM) [*Lyon et al.*, 2004; *Wiltberger et al.*, 2005] global MHD simulations will be run over a range ($M_A = 2$–35) of solar wind Alfven Mach numbers. Using those LFM simulations, β_s of the magnetosheath plasma is reparameterized as a function of M_A and the fit

$$\beta_s = (M_A/6.7)^{2.05} \quad (5)$$

is obtained. At low Mach numbers, $\beta_s = (M_A/6)^{1.92}$ predicts β_s values that are higher (by 50% at $M_A = 1$); as M_A increases, the two expressions yield β_s values that are closer to each other, with the two β_s values being identical at $M_A = 34$. The LFM parameterization $\beta_s = (M_A/6.7)^{2.05}$ confirms the validity

of the BATSRUS result $\beta_s = (M_A/6)^{1.92}$. In the present study, the expression $\beta_s = (M_A/6)^{1.92}$ will be used.

[19] Expression (3) contains information about how the bow shock modifies the solar wind plasma, about how the magnetosheath flow pattern modifies the solar wind plasma, and about how asymmetric reconnection works. Expression (3) has a strong dependence on the Alfven Mach number M_A of the solar wind, which determines the plasma β of the magnetosheath, which in turn by pressure balance determines the magnetic field strength of the magnetosheath plasma at the magnetopause. It is convenient to rewrite expression (3) as

$$R_2 = {n_{sw}}^{1/2} {u_{sw}}^2 f(M_A, M_{ms}, \theta_{clock}, \theta_{Bn}) \tag{6}$$

with the clock angle and Mach number dependence of R_2 in the function

$$f(M_A, M_{ms}, \theta_{clock}, \theta_{Bn}) = 0.8\pi^{1/2} {m_p}^{1/2} \left(1 + 0.5 {M_{ms}}^{-2}\right) C^{-1/2} (gh)^{3/2} \left\{\chi g^{1/2} (g\chi + h)^{1/2}\right\} \tag{7}$$

[20] Note in *Borovsky* [2013] that a correction to the reconnection rate based on compressibility arguments [*Birn et al*., 2010, 2012] was implemented. That correction led to the Cassak-Shay-Birn equation for asymmetric reconnection. Using the Cassak-Shay-Birn equation as a starting point for the dayside reconnection function led to poorer performance of that function. More will be said about this in section 2.4.

[21] In section 5 a simplified approximation of R_2 from *Borovsky* [2013] will be used to produce mathematically simplified versions of the solar wind driver functions.

2.2. The Length of the Reconnection X Line

[22] For flow shears above the Alfven speed, it is believed that reconnection becomes problematic. At high Mach numbers, the length of the dayside X line may be limited by flow velocities of the magnetosheath plasma exceeding the local Alfven speed, cutting off the efficiency of reconnection. For symmetric reconnection, the argument is that if the shear velocity (total jump in the flow speed between plasma 1 and plasma 2) parallel to the direction of the reconnecting magnetic field exceeds twice the reconnection outflow speed, a stable neutral line will not form [*Mitchell and Kan*, 1978; *Chen et al*., 1997]. Computer simulations support this notion [*Chen et al*., 1997; *La Belle-Hamer et al*., 1994; *Cassak and Otto*, 2011].

[23] The effects of flow shear on magnetic field line reconnection have not been sorted out for reconnection with a guide field, particularly for asymmetric reconnection with a guide field. For a magnetic field clock angle of θ, the asymmetric reconnection outflow speed has an approximately sin (θ/2) dependence [cf. *Swisdak and Drake*, 2007, equation (8)], and the components of the shear velocity parallel to the directions of the magnetic fields in the magnetosphere and in the magnetosheath will also have θ dependences. The velocity shear between the magnetosphere and magnetosheath may also affect the locations on the magnetopause where reconnection occurs, hence it may affect the orientation of the X line. In the estimate of the length of the reconnection X line presented here, all of these unknown dependences on the clock angle θ will be ignored.

[24] For symmetric reconnection, the reconnection outflow speed is v_A. The symmetric plasma reconnection rate as a function of the shear velocity is plotted in Figure 3 of *Cassak and Otto* [2011]: Here the rate falls off to about 70% of its no-shear value when the velocity jump is equal to v_A and the reconnection rate goes to zero when the jump is equal to $2v_A$. For asymmetric reconnection between the magnetosphere (subscript "*m*") and the magnetosheath (subscript "*s*"), ignoring clock angle effects, the reconnection outflow speed $u_{\rm out}$ is given by [cf. *Cassak and Shay*, 2007, equation (13)]

$${u_{\rm out}}^2 = (B_m B_s/4\pi)((B_m + B_s)/(\rho_m B_s + \rho_s B_m)) \tag{8}$$

[25] Taking $\rho_m B_s \ll \rho_s B_m$ (because $B_s \le B_m$ and in general $\rho_m \ll \rho_s$), expression (8) can be written as

$$u_{\rm out} = v_{As}((B_m/B_s) + 1)^{1/2} \tag{9}$$

[26] By pressure balance across the magnetopause, the ratio B_m/B_s can be written [cf. *Borovsky*, 2008a, equations (5) and (6)] as

$$B_m/B_s = (1 + \beta_s)^{1/2} \tag{10}$$

[27] Expression (10) used in expression (9) yields

$$u_{\rm out} = v_{As}\left[(1 + \beta_s)^{1/2} + 1\right]^{1/2} \tag{11}$$

[28] For the magnetosheath flowing around the magnetosphere, the flow shear across the magnetopause increases in intensity with increasing distance from the nose of the magnetosphere. When the flow speed u of the magnetosheath along the magnetopause exceeds the local value of $u_{\rm out}$, the reconnection will be reduced by about 70%, and when the flow speed of the magnetosheath exceeds twice the local value of $u_{\rm out}$, reconnection will be completely cut off. Here we will take the position in the magnetosheath flow along the magnetopause where $u = u_{\rm out}$ to give the effective length of the X line. Writing $u = u_{\rm out}$, using expression (11) for $u_{\rm out}$ and dividing both sides by $v_{As}[(1+\beta_s)^{1/2}+1]^{1/2}$ yields the condition:

$$M_A\left[(1 + \beta_s)^{1/2} + 1\right]^{-1/2} = 1 \tag{12}$$

in the magnetosheath flow along the magnetopause for the effective length of the X line.

[29] In Figure 1 the Alfven Mach number of the flow of the magnetosheath around the Earth is shown for two cases: low-Mach-number solar wind ($M_A = 2.01$; top) and high-Mach-number solar wind ($M_A = 40.2$; bottom). The standoff distance of the bow shock and flow pattern of the magnetosheath differ substantially between the low- and high-Mach-number cases; the current systems in the bow shock and magnetosheath also differ substantially [cf. *Lopez et al*., 2011]. According to expression (4b), for solar wind Alfven Mach numbers $M_A \gg 6$, the plasma β of the magnetosheath is high and the magnetosheath flow can be described by gas dynamics: For solar wind Alfven Mach numbers $M_A \ll 6$,

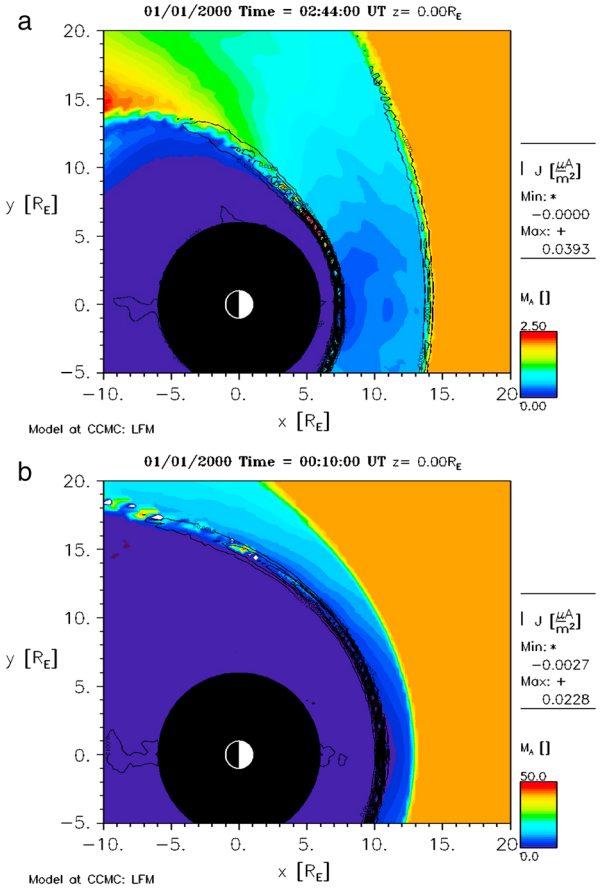

Figure 1. The Alfven Mach number pattern of magnetosheath sheath flow at low and high Alfven Mach numbers of the solar wind. The color contours are the local Alfven Mach number v/v_A of the plasma flow and the black contours are the magnitude of the current density in the plasma (outlining the magnetopause). (top) $M_A = 2.01$ for the upstream solar wind (orange). (bottom) $M_A = 40.2$ in the upstream solar wind (orange). (All panels are from run LFM4 [111412_2] at the CCMC with southward IMF and $T_{sw} = 1$ eV.).

the plasma β of the magnetosheath is lower than unity and the magnetosheath flow must be described by MHD. Note in Figure 1 the difference in the pattern of color contours in the magnetosheath: At low solar wind Mach number, the Mach number contours in the magnetosheath are approximately perpendicular to the magnetosheath, and at high solar wind Mach number, the Mach number contours in the magnetosheath are approximately parallel to the magnetopause. Note also in Figure 1 (top) for low-Mach-number solar wind, there is a slingshot effect in the magnetosheath that accelerates the sheath flow along the magnetopause to speeds above the solar wind speed [cf. *Lavraud et al.*, 2007; *Lavraud and Borovsky*, 2008].

[30] To estimate the length of the reconnection X line, the position at which the magnetosheath flow along the magnetopause goes through $M_A[(1+\beta_s)^{1/2}+1]^{-1/2} = 1$ (cf. expression (12)) will be taken. For a series of computer simulations using the LFM MHD code [*Lyon et al.*, 2004; *Wiltberger et al.*, 2005] at the Community Coordinated Modeling Center [*Bellaire*, 2006; *Rastatter et al.*, 2012], contour plots of the quantity $M_A[(1+\beta_s)^{1/2}+1]^{-1/2}$ were examined and the location where $M_A[(1+\beta_s)^{1/2}+1]^{-1/2} = 1$ in the magnetosheath flow along the magnetopause was measured as a function of the Alfven Mach number M_A of the upstream solar wind. In Figure 2 the position of the $M_A[(1+\beta_s)^{1/2}+1]^{-1/2} = 1$ contour given by expression (12) is shown for three snapshots during a computer simulation in which the magnetic field strength in the solar wind is varied to vary the upstream solar wind Alfven Mach number. Shown in Figure 2 are cuts in the equatorial plane: the black disc around the Earth has a radius of 6 R_E. The color scale is the logarithm of the total electric current density in the plasma, highlighting the magnetopause in red and the bow shock in yellow. Contours of $M_A[(1+\beta_s)^{1/2}+1]^{-1/2}$ are plotted in black. In Figure 2 (top) the solar wind Alfven Mach number is $M_A = 2.01$ and the black contours intersect the magnetopause at a position angle from the Sun-Earth line (nose) of about $\xi = 95°$. In Figure 2 (middle; solar wind $M_A = 5.2$) the black contours intersect the magnetopause at a position angle $\xi = 78°$ from the nose. In Figure 2 (bottom) with solar wind $M_A = 27.9$, the black contours intersect the magnetopause at $\xi = 34°$.

[31] For three computer simulations in which the solar wind magnetic field strength is varied to vary the solar wind Alfven Mach number, the position angle ξ (in degrees) of where the flow goes through the critical condition $M_A[(1+\beta_s)^{1/2}+1]^{-1/2} = 1$ is plotted as a function of the Alfven Mach number M_A of the solar wind in Figure 3. The three simulations have three different temperatures of the solar wind plasma upstream of the bow shock: $T = 1$ eV (blue), $T = 10$ eV (red), and $T = 120$ eV (green). This variation in solar wind temperature varies the relationship between the Alfven Mach number and the magnetosonic Mach number of the solar wind. A definite trend of ξ versus M_A is seen and the value of the upstream temperature of the solar wind does not systematically change the results. A power law fit to the data points in Figure 3 yields

$$\xi = 141° M_A{}^{-0.404} \tag{13}$$

where ξ is in degrees.

[32] As an effective length of the dayside X line, the product of the angle ξ (in radians) and the size of the magnetosphere will be taken. For the size of the magnetosphere, the standoff distance d along the Sun-Earth line will be taken [cf. *Walker and Russell*, 1995, equation (6.21)]:

$$d = d_o \left(n_{sw} u_{sw}{}^2\right)^{-1/6} \tag{14}$$

where $d_o = 6.81 \times 10^{10}$ cm and where d is in units of cm, n_{sw} is in units of cm^{-3}, and u_{sw} is in units of km/s. Taking ξ from expression (13) given by the position where the flow goes through $M_A[(1+\beta_s)^{1/2}+1]^{-1/2} = 1$ (expression (12)), the effective length $L_{\text{X line}}$ of the dayside X line is (with a factor of 2 for the two sides away from the nose)

$$L_{\text{X line}} = 4.9\, d_o \left(n_{sw} u_{sw}{}^2\right)^{-1/6} M_A{}^{-0.404} \tag{15}$$

[33] $L_{\text{X line}}$ is plotted as a function of the solar wind Alfven Mach number M_A in Figure 4.

[34] An indication of the Alfven Mach number dependence of the length of the dayside neutral line can be seen in Figure 5 from an LFM computer simulation of the magnetosphere with an IMF clock angle of 90°. In the three snapshots, the flow

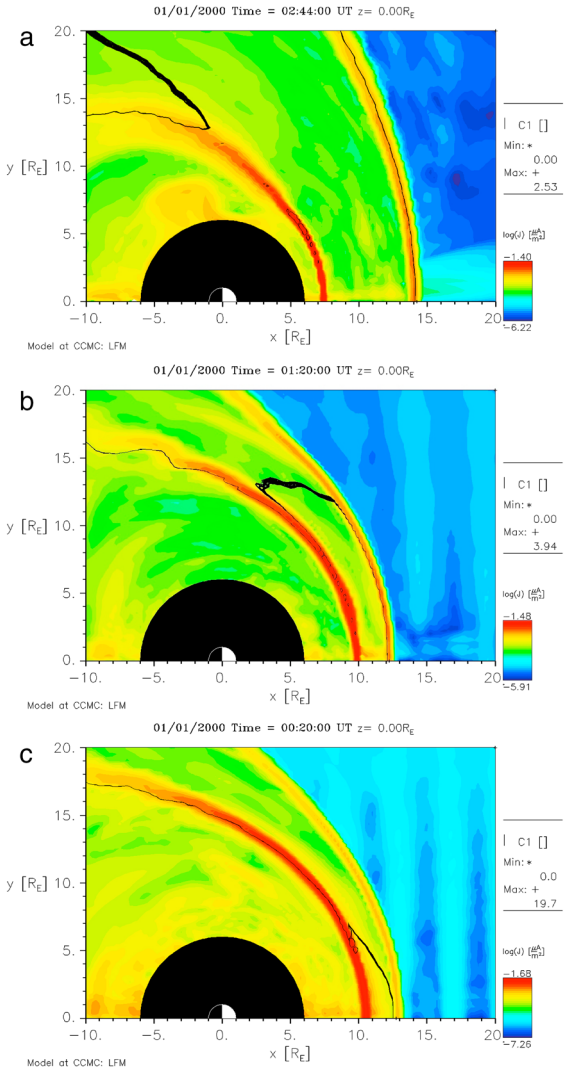

Figure 2. The position of the critical magnetosheath flow $M_A[(1+\beta_s)^{1/2}+1]^{-1/2}=1$ contour along the magnetopause is outlined with black curves in the three panels for three different solar wind Alfven Mach numbers. (top) $M_A = 2.01$ in the upstream solar wind. (middle) $M_A = 5.2$ in the upstream solar wind. (bottom) $M_A = 27.9$ in the upstream solar wind. (All panels from run LFM4 [111412_2] at CCMC with southward IMF and $T_{sw} = 1$ eV.).

streamlines inside the dayside magnetosphere are traced and flow vectors are shown. Figure 5 is for a simulation with $M_A = 2.03$ (top), $M_A = 10.2$ (middle), and $M_A = 27.9$ (bottom). In the higher-Mach-number cases (middle and bottom) the flow streamlines inside the magnetosphere focus toward the nose of the magnetosphere, as if the reconnection intensity is strong at the nose and weak away from the nose. In the low-Mach-number case the streamlines aim sunward, without a focus toward the nose, as if the reconnection X line were strong all across the magnetosphere. The flow vector directions shown by the field of black arrowheads show the same behavior: a dayside magnetospheric flow pattern focused toward the nose when the solar wind Alfven Mach number is high and a dayside magnetosphere flow that does not focus to the nose when the Alfven Mach number of the solar wind is low. One must use caution in the MHD simulations when

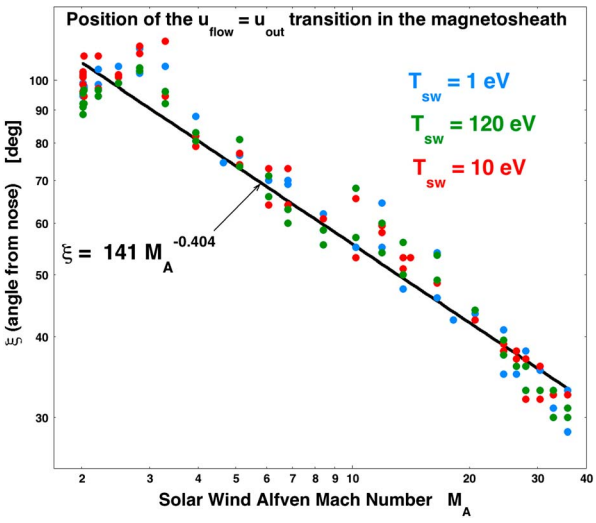

Figure 3. From three LFM computer simulations, the position angle ξ where the magnetosheath flow along the magnetopause goes through the critical value $M_A[(1+\beta_s)^{1/2}+1]^{-1/2}=1$ plotted as a function of the Alfven Mach number M_A of the solar wind. The three simulations have three different temperatures of the solar wind plasma upstream of the bow shock: $T = 1$ eV (blue), $T = 10$ eV (red), and $T = 120$ eV (green).

gauging the strength of reconnection since (1) reconnection is enabled by numerical errors (high-order numerical diffusivity) acting on the magnetic field at current sheets with thicknesses approaching the grid spacing [*Kuznetsova et al.*, 2007] and (2) numerical errors in Faraday's law $\partial B/\partial t = \nabla \times (u \times B)$ at narrow flow gradients prevent the magnetic field from being exactly convected with the flow.

[35] Note that Kelvin-Helmholtz instabilities at the magnetopause for high shear velocities may enhance reconnection via vortex-induced reconnection [cf. *Chen et al.*, 1997; *Zhang et al.*, 2011] (see also section 6.1). This would produce

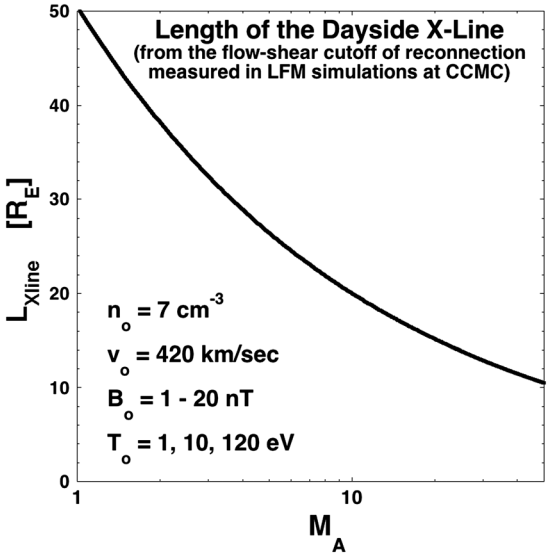

Figure 4. From expression (15) an estimate of the length of the dayside reconnection X line is plotted as a function of the solar wind Alfven Mach number M_A.

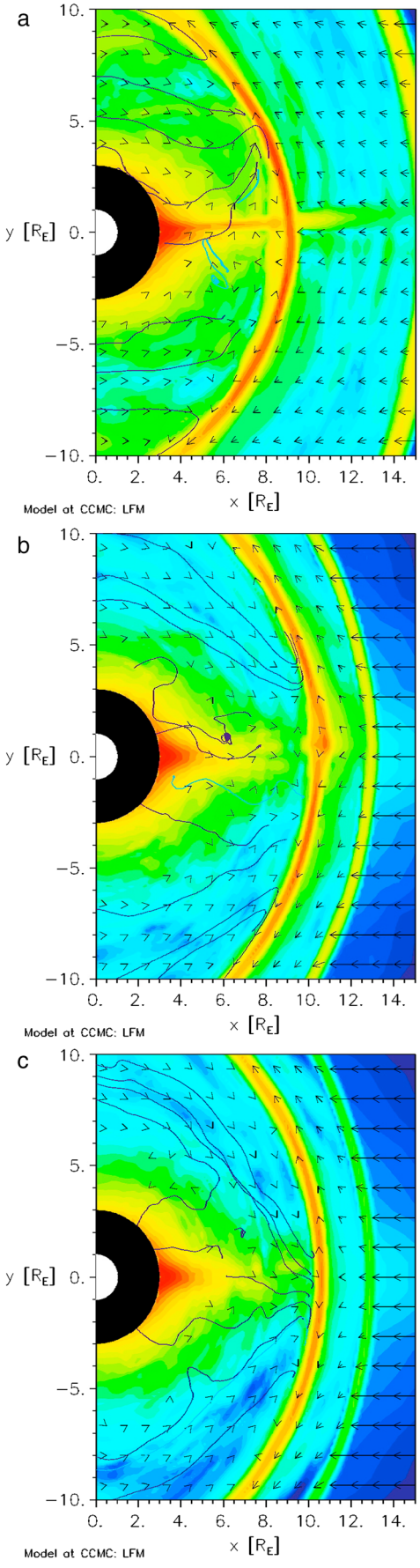

an additional reconnection that increases with solar wind Alfven Mach number, in opposition to the length of the X line scaling given by expression (15).

2.3. MHD Generator Current Saturation

[36] After becoming magnetically connected to the polar ionospheres by dayside reconnection, the moving solar wind/magnetosheath plasma will supply electrical current to each ionosphere producing resistive cross-polar cap electrical potentials. This current couples the MHD generator of the moving solar wind to the ionospheric load, tending to impose the motional voltage from the solar wind onto the polar cap.

[37] The solar wind acts like a "current-limited Voltage generator" [*Borovsky et al.*, 2009]: In the absence of a load it has a fixed voltage and under a direct short it supplies a maximum current. In the nomenclature of section 6 of *Lysak* [1990], when the polar ionosphere has weak conductivity the solar wind act like a fixed-voltage generator and when the polar conductivity is strong, the solar wind acts like a fixed-current generator. For a given solar wind motional potential $\Delta\phi_{sw}$, the maximum field-aligned current that a flux tube of the solar wind can supply is [cf. *Borovsky et al.*, 2009, equation (8)]

$$I_{\max} = (L/W)_{sw}\Delta\phi_{sw}/\mu_o v_A \tag{16}$$

where v_A is the Alfven speed in the solar wind plasma and $(L/W)_{sw}$ is the length to width cross-sectional shape of the solar wind flux tube, with W being in the direction of the potential drop $\Delta\phi_{sw}$. (For $(L/W)_{sw} = 1$ and for a typical solar wind with $v_A = 54$ km/s, expression (16) yields 14.7 A/V as the current the solar wind can supply to one ionosphere.) In order for the collisionless plasma solar wind MHD generator to supply current to the ionosphere, it must undergo a potential drop [cf. *Borovsky et al.*, 2009, Figure 23]: The electrical potential that the collisionless solar wind MHD generator can apply onto the ionospheric load is

$$\Delta\phi_{\text{ion}} = \Delta\phi_{sw}[1 - (I/I_{\max})] \tag{17}$$

[38] The ionospheric potential must also be in agreement with the resistive potential drop in the ionosphere governed by the current I.

[39] For a given potential $\Delta\phi_{\text{ion}}$ applied to the ionosphere, the closure Pedersen current that the ionosphere carries is given by

$$I_{\text{ion}} = L_{\text{ion}}\Delta\textstyle\sum_P(\Delta\phi_{\text{ion}}/W_{\text{ion}}) = (L/W)_{\text{ion}}\textstyle\sum_P\Delta\phi_{\text{ion}} \tag{18}$$

where $\sum_P$ is the height-integrated Pedersen conductivity of the ionosphere, W_{ion} is the dimension over which $\Delta\phi_{\text{ion}}$ falls in the ionosphere, L_{ion} is the dimension perpendicular to W_{ion} in the ionosphere, and $(L/W)_{\text{ion}}$ is the shape of the foot of the

Figure 5. For three different solar wind Alfven Mach numbers M_A, flow vectors and streamlines of flow in the dayside magnetosphere are plotted in the equatorial plane. The Mach numbers are (top) $M_A = 2.03$, (middle) $M_A = 10.2$, and (bottom) $M_A = 27.9$. The color contours are the logarithm of the total current density in the plasma, highlighting the dayside magnetopause in red and the bow shock in yellow. All three panels are from the run LFM7 [111712_2] at the CCMC. All three panels on the right are from the run LFM9 [120812_1] at the CCMC with the top panel at $M_A = 2.02$.

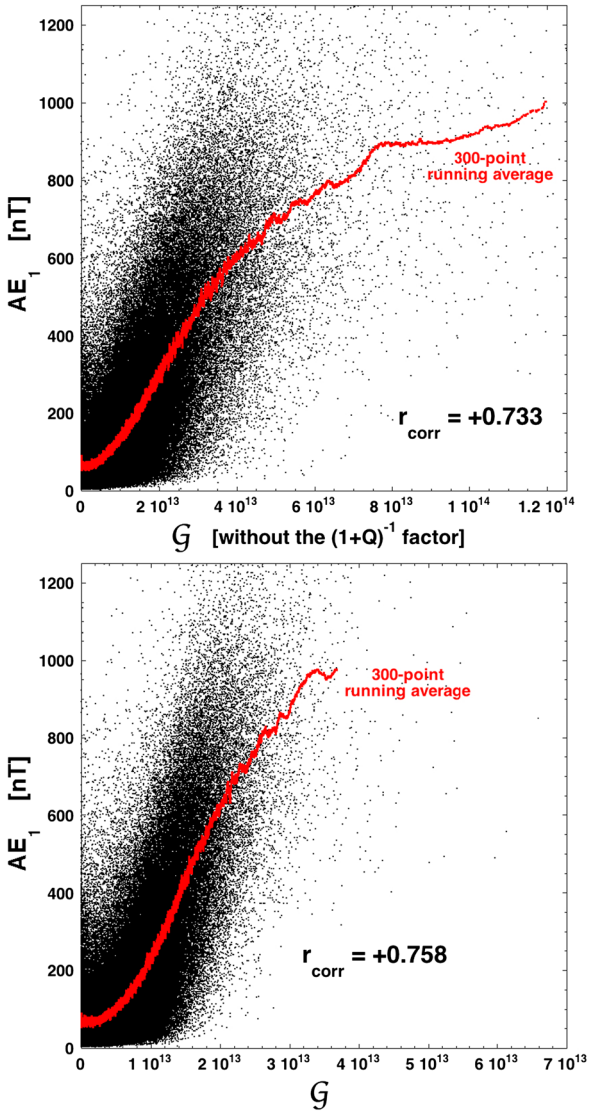

Figure 6. Examining the effect of the $(1+Q)^{-1}$ MHD generator saturation term in the expression for the reconnection-coupled generator $\mathcal{G}$. In the top panel the $(1+Q)^{-1}$ term is not included in the reconnection-couple-generator expression; in the bottom panel it is. In the two panels, the black points are the individual 1 h data points and the red points are 300-point running averages of the black points. The horizontal scales are chosen so that the shapes of the $AE_1 < 400$ nT portions of the two red curves are about the same so the effect of the inclusion of the $(1+Q)^{-1}$ term at large values of the driver functions can be more clearly seen.

solar wind flux tube in the ionosphere. Using expression (18) for I_{ion} in expression (17) as the current I drawn from the solar wind and using expression (16) to eliminate $I_{\max}$, expression (17) becomes

$$\Delta\phi_{\text{ion}} = \Delta\phi_{sw}[1 - Q(\Delta\phi_{\text{ion}}/\Delta\phi_{sw})] \tag{19}$$

for the potential applied by the solar wind to the ionosphere, where

$$Q \equiv \mu_o v_A \Sigma_P (L/W)_{\text{ion}}/(L/W)_{sw} \tag{20}$$

[40] Expression (19) is solved for $\Delta\phi_{\text{ion}}$ to yield

$$\Delta\phi_{\text{ion}} = \Delta\phi_{sw}(1+Q)^{-1} \tag{21}$$

[see also *Gao et al.*, 2012, equation (4)] for the potential applied to the ionosphere by the solar wind. If the solar wind MHD generator was not current limited, the potential applied to the ionosphere would be $\Delta\phi_{sw}$. Instead, the potential is reduced by the generator saturation parameter $(1+Q)^{-1}$. Taking $(L/W)_{\text{ion}} \approx (L/W)_{sw}$ (which has been seen to be approximately true in global MHD simulations [*Borovsky et al.*, 2009]), expression (20) can be written as

$$Q = v_A \Sigma_P / 796 \tag{22}$$

where v_A is expressed in units of km/s and Σ_P is expressed in units of mhos.

[41] Expression (19) is the Hill equation [cf. *Hill et al.*, 1976 equation (3); *Siscoe et al.*, 2004, equation (1)], derived by *Hill et al.* [1976] with arguments about limitations on the distortion of the outer magnetosphere by ionosphere-magnetosphere current systems and derived by *Siscoe et al.* [2004] with arguments about the limitations of the momentum of the solar wind and the amount of current that it can drive into the magnetosphere-ionosphere system. Both of those pictures yield values of $Q \propto v_A \Sigma_P$, but with differing numerical factors [e.g., *Borovsky and Denton*, 2006, equation (1)]. *Ridley* [2007] and *Kivelson and Ridley* [2008] use an Alfven wing picture [cf. *Mallinkrodt and Carlson*, 1978] to obtain expression (19); this picture yields the same numerical factor in the value of Q as does expression (22) [cf. *Borovsky et al.*, 2009. equation (3)], without the consideration of the flux tube eccentricity factors $(L/W)_{\text{ion}}$ and $(L/W)_{sw}$.

[42] For the generator-quality factor in expression (1), the quantity $(1+Q)^{-1}$ from expression (21) will be used with Q given by expression (22). In general, the height-integrated Pedersen conductivity Σ_P of the polar ionosphere is not known: equation (4) of *Ober et al.* [2003] will be used for Σ_P, which is $\Sigma_P = 0.77\ F_{10.7}{}^{1/2}$, with $F_{10.7}$ being the Earth-monitored 10.7 cm radio flux from the Sun.

2.4. Examining the Reconnection-Coupled MHD Generator

[43] Using expression (6) for the local reconnection rate, expression (15) for the effective length of the dayside reconnection X line, and from expression (21) as the generator quality factor, expression (1) for the reconnection-coupled MHD generator becomes

$$\mathcal{G} = 4.9 d_o n_{sw}{}^{1/2} u_{sw}{}^2 f(M_A, M_{ms}, \theta_{\text{clock}}, \theta_{Bn}) \left(n_{sw} u_{sw}{}^2\right)^{-1/6} M_A{}^{-0.404} (1+Q)^{-1} \tag{23}$$

with expressions (7) and (22) providing the definitions $f(M_A, M_{ms}, \theta_{\text{clock}}, \theta_{Bn})$ and $Q(v_A, \Sigma_P)$ and where $d_o = 6.81 \times 10^{10}$ cm. With $\Sigma_P = 0.77\ F_{10.7}{}^{1/2}$, all parameters in expression (23) are written in terms of solar parameters and upstream (from the bow shock) solar wind parameters.

[44] By comparing Figure 6 (top and bottom), the effect of the generator-current limit $(1+Q)^{-1}$ on the performance of the reconnection-coupled generator $\mathcal{G}$ can be seen. In Figure 6 (top) the 1 h lagged AE index AE_1 is plotted as a function of a reconnection-coupled generator without the $(1+Q)^{-1}$

Table 1. Linear Correlation Coefficients r_{corr} Between Various Driver Functions and Seven Geomagnetic Indices[a]

	$\mathscr{G}$	$\mathscr{G}_{app}$	$\mathscr{G}_{Birn}$	$\mathscr{B}$	$\mathscr{F}$	$\mathscr{G}+\mathscr{B}$	$\mathscr{G}+\mathscr{F}$
AE 1 h lagged	0.758	0.746	0.743	0.533/0.372	0.537/0.443	0.797	0.782
AU 1 h lagged	0.660	0.649	0.654	0.567/0.341	0.623/0.444	0.701	0.700
−*AL* 1 h lagged	0.729	0.718	0.712	0.439/0.350	0.409/0.397	0.763	0.745
PCI	0.719	0.712	0.709	0.351/0.340	0.316/0.424	0.752	0.743
Kp 1 h lagged	0.648	0.637	0.642	0.610/0.531	0.658/0.632	0.778	0.781
−MBI 1 h lagged	0.707	0.696	0.697	0.588/0.422	0.583/0.498	0.775	0.762
−*Dst** 2 h lagged	0.565	0.569	0.568	0.511/0.468	0.538/0.557	0.678	0.685
7-index sum	4.785	4.728	4.726	3.596/2.823	3.665/3.395	5.242	5.199

[a]The correlation coefficients are for the January 1980 to May 2012 1 h resolution OMNI2 data set. For the Bohm viscosity driver $\mathscr{B}$ and the freestream-turbulence driver $\mathscr{F}$, two sets of numbers are given: the first value is the correlation for only hours where the hourly averaged components of the solar wind magnetic field yield GSM clock angles $0° \le \theta_{clock} \le 20°$; the second value is the correlation for all values of θ_{clock}. All r_{corr} values are positive. The bottom row is the seven-index sum of the correlation coefficients.

term and (bottom) AE_1 is plotted as a function of the reconnection-coupled generator with the $(1+Q)^{-1}$ term (expression (23)). The red 300-point running averages highlight the trend in the black data points. Without the $(1+Q)^{-1}$ term, the data suffer a bendover of the AE_1 index at high values of the driver: This is the so-called polar-cap potential saturation [cf. *Wygant et al*., 1983; *Reiff and Luhmann*, 1986; *Weimer et al*., 1990]. Adding the $(1+Q)^{-1}$ term in Figure 6 (bottom) largely eliminates that bendover and linearizes the relationship between AE_1 and $\mathscr{G}$ at larger values of $\mathscr{G}$ [see also *Lavraud and Borovsky*, 2008, Figure 17]. Note that there is a strong nonlinearity at weak values of $\mathscr{G}$ where the 300-point running average in Figure 6 makes a strong bend going from a horizontal orientation to a steep slope: This nonlinearity will appear again in section 4.

[45] In Table 1 the linear correlation coefficients between the reconnection-coupled generator $\mathscr{G}$ and seven geomagnetic indices are collected. In the bottom row of Table 1 the sum of the correlation coefficients for all seven indices is displayed. The correlation coefficients for a reconnection-coupled generator function $\mathscr{G}_{Birn}$ based on the Cassak-Shay-Birn reconnection rate [see *Borovsky*, 2013] and another $\mathscr{G}_{app}$ based on the approximated version of the dayside local reconnection rate R_{2app} [*Borovsky*, 2013, equation (34)] are also displayed in Table 1. As can be seen, the three functions $\mathscr{G}$, $\mathscr{G}_{Birn}$, and $\mathscr{G}_{app}$ yield similar correlation coefficients, with those of $\mathscr{G}$ being slightly superior. For practical purposes, the function $\mathscr{G}_{app}$ is much easier to implement (see section 5).

3. The Viscous Interaction

[46] The viscous interaction is a transfer of momentum from the flowing magnetosheath plasma across the magnetopause into the magnetosphere. The mechanisms that transfer this momentum across the magnetopause are not well understood.

[47] Two approaches to developing a driver function to describe the viscous interaction between the solar wind and the Earth's magnetosphere will be taken. The first approach is to (a) try to discern the physical mechanism of viscosity in a collisionless plasma, (b) use that mechanism to calculate a flow Reynolds number for the magnetosheath flowing around the magnetosphere, and (c) use this Reynolds number in an aerodynamic viscous-drag formula. This first approach was taken, for example, by *Vasyliunas et al*. [1982]. For the mechanism of viscosity in a collisionless plasma, possibilities include Coulomb collisions [*Kaufman*, 1960; *Braginskii*, 1965], Bohm Diffusion [*Eviatar and Wolf*, 1968; *Borovsky*, 2006], Landau damping [*Borovsky and Gary*, 2009], mass diffusion by plasma waves [*LaBelle and Treumann*, 1988; *Johnson and Cheng*, 1997], Kelvin-Helmholtz interactions [*Fejer*, 1964; *Nykyri and Otto*, 2001], among other mechanisms. Bohm diffusion will be used for this first approach.

[48] The second approach to developing a viscous driver function is to exploit the "freestream turbulence effect" [*Wu and Faeth*, 1994; *Volino et al*., 2003; *Borovsky and Steinberg*, 2006a], which allows one to obtain an effective Reynolds number for the flow that is independent of the actual mechanism of viscosity. This effective Reynolds number is then used in an aerodynamic viscous drag formula.

[49] In this section both approaches will be taken, yielding a Bohm-viscosity driver function $\mathscr{B}$ in section 3.1 and a freestream-turbulence driver function $\mathscr{F}$ in section 3.3. The two viscous drivers will be examined in section 3.3.

3.1. Bohm Viscosity

[50] In laboratory experiments, plasmas are often observed to spread across the magnetic field with the Bohm-diffusion rate [*Bohm et al*., 1949; *Rynn*, 1964; *Taroni et al*., 1994]. Bohm diffusion is associated with a spatial step that is the particle gyroradius and a time step that is the particle gyroperiod: It can be thought of as the diffusion rate that results from the interruption of particle gyroorbits on a gradient.

[51] The viscous drag force F_v on the object in the wind can be written as [*Faber*, 1995]

$$F_v = 0.5\rho_o u_o^2 A\, C_v \tag{24}$$

where ρ_o is the mass density of the wind, u_o is flow velocity of the ambient wind past the object, A is the cross-sectional area of the object as seen by the flow, and C_v is the viscous drag coefficient of the object. For subsonic flow, C_v depends only on the shape of the object and the Reynolds number Re of the flow past the object. *Borovsky and Funsten* [2003a] estimated C_v for the Earth's magnetosphere, obtaining

$$C_v = 13Re^{-1/2} \tag{25}$$

[52] Expressing the cross-sectional area of the Earth's magnetosphere as $A = \pi(d/2)^2$, where d is the diameter of the magnetosphere, and using expression (25), expression (24) becomes

$$F_v = (13\pi/8)\rho_{sw} u_{sw}^2 d^2 Re^{-1/2} \tag{26}$$

where the subscript "*sw*" means the solar wind upstream of the bow shock.

[53] The dimensionless Reynolds number Re is a measure of the importance of viscous dissipation on a flow shear: It is the ratio of a flow-crossing timescale and a viscous-dissipation timescale. The Reynolds number is a property of the flow pattern, not of the fluid. For a characteristic flow velocity u, a characteristic length scale L in the flow pattern, and the kinematic (molecular) viscosity v of the fluid, Re is

$$Re = Lu/v \tag{27}$$

[e.g., *Nakayama and Boucher*, 1999]. For the magnetosheath flow around the magnetosphere, we will take L to be the diameter d of the magnetosphere and u to be bulk flow velocity of the magnetosheath. For the kinematic viscosity of a collisionless magnetized plasma we have three possibilities [*Borovsky and Gary*, 2009]: the Braginskii Coulomb collision viscosity v_{Brag} of the plasma (which for the magnetosheath will be very small, $\sim 1.3 \times 10^6$ cm^2/s), the Landau-damping shear viscosity v_{Landau} (which will be larger), or the Bohm diffusion coefficient v_{Bohm} (which will be the largest possible value, $\sim 1.0 \times 10^{13}$ cm^2/s).

[54] For this estimate, we will take the viscosity v_{Bohm} to be equal to the Bohm-diffusion coefficient $D_B = (1/16) v_{Ti}^2/\omega_{ci}$ [*Bohm et al*., 1949; *Rynn*, 1964]. (See also *Eviatar and Wolf* [1968] for an argument for Bohm diffusion acting at the magnetopause and see *Vasyliunas et al*. [1982] for a derivation of the viscous force on the magnetosphere using the assumption of Bohm diffusion for the fluid viscosity.) For the magnetosheath plasma (subscript "*s*"), this is written as

$$v_{\mathrm{Bohm}} = (1/16)\, v_{Ti}^2/\omega_{ci} = (1/16)\, ck_B T_{is}/eB_s \tag{28}$$

where T_{is} is the ion temperature of the magnetosheath plasma and B_s is the magnetic field strength in the magnetosheath. Taking $T_i >> T_e$ in the magnetosheath, the ion temperature in the magnetosheath can be expressed in terms of the plasma beta $\beta_s = 8\pi n_s k_B T_{is}/B_s^2$ and the magnetic field strength B_s:3

$$k_B T_{is} = \beta_s B_s^2/8\pi n_s \tag{29}$$

[55] Using pressure-balance arguments, the magnetic field strength in the magnetosheath adjacent to the frontside magnetopause is given by equation (5) of *Borovsky* [2008a]:

$$B_s = (8\pi m_i n_{sw})^{1/2} u_{sw} \left(1 + 0.5 M_{ms}^{-2}\right)^{1/2} (1+\beta_s)^{-1/2} \tag{30}$$

where the subscript "*sw*" stands for the solar wind upstream of the bow shock. Here M_{ms} is the magnetosonic Mach number of the solar wind. Using expressions (29) and (30) to eliminate $k_B T_{is}$ and B_s, expression (28) becomes

$$v_{\mathrm{Bohm}} = \left(c m_i^{1/2}/16(8\pi)^{1/2} e\right) \beta_s n_s^{-1/2} u_{sw} \left(1 + 0.5 M_{ms}^{-2}\right)^{1/2} (1+\beta_s)^{-1/2} \tag{31}$$

[56] Expressing the magnetosheath number density n_s at the dayside magnetopause as $n_s = C n_{sw}$ (cf. eq. (9) of *Borovsky* [2008a]) where n_{sw} is the upstream solar wind number density and C is the density compression ratio of the nose of the bow shock, expression (31) for the Bohm viscosity becomes

$$v_{\mathrm{Bohm}} = \left(c m_i^{1/2}/16(8\pi)^{1/2} e\right) n_{sw}^{-1/2} u_{sw} W \tag{32}$$

where the parameter W is defined as

$$W = \beta_s C^{-1/2} \left(1 + 0.5 M_{ms}^{-2}\right)^{1/2} (1+\beta_s)^{-1/2} \tag{33}$$

[57] Note that the plasma beta of the magnetosheath near the dayside magnetopause can be parameterized as $\beta_s = (M_A/6)^{1.92}$ [cf. *Borovsky*, 2008a, equation (7)], where M_A is the Alfven Mach number of the solar wind as seen by the Earth, and the density compression ratio of the shock C is also a function of the Mach number: hence, W is a function only of the Mach number of the solar wind.

[58] The Reynolds number for the magnetosheath flow around the magnetosphere (expression (27)) is now rewritten. Taking the characteristic scale size of the flow to be $L = d$, taking the characteristic flow speed of the magnetosheath to be $u_s = C^{-1} u_{sw}$, and taking the magnetosheath's viscosity to be the Bohm viscosity v_{Bohm}, expression (27) becomes

$$Re = dC^{-1} u_{sw}/v_{\mathrm{Bohm}} \tag{34}$$

[59] Using expression (32) for the Bohm viscosity v_{Bohm}, expression (34) for the Reynolds number of the magnetosheath flow around the magnetosphere becomes

$$Re = \left(16(8\pi)^{1/2} e/c m_i^{1/2}\right) d n_{sw}^{1/2} C^{-1} W^{-1} \tag{35}$$

[60] Note all of the velocity dependence of the Reynolds number is in the parameters C and W.

[61] The viscous force on the magnetosphere from the magnetosheath flowing over its surface (assuming Bohm diffusion acts) is given by inserting expression (35) for the Reynolds number Re into expression (26):

$$F_{v-\mathrm{Bohm}} = (13\pi/8)\, m_i \left(c\, m_i^{1/2}/16\,(8\pi)^{1/2} e\right)^{1/2} n_{sw}^{3/4} u_{sw}^2 d^{3/2} (CW)^{1/2} \tag{36}$$

[62] Dropping the constants, this is conveniently written as

$$F_{v-Bohm} \propto n_{sw}^{3/4} u_{sw}^2 d^{3/2} (CW)^{1/2} \tag{37}$$

[63] The diameter d of the Earth's magnetosphere can be estimated from the pressure-standoff of the solar wind: $d \propto (n_{sw} u_{sw}^2)^{-1/6}$ [cf. *Walker and Russell*, 1995, equation (6.21)]. Using this, expression (37) becomes

$$F_{v-\mathrm{Bohm}} \propto n_{sw}^{1/2} u_{sw}^{3/2} (CW)^{1/2} \tag{38}$$

[64] Using the parameterization from equation (10) of *Borovsky* [2008a] for the compression ratio of the nose of the bow shock $C = \{2.44 \times 10^{-4} + [1 + 1.38 \log_e(M_A)]^{-6}\}^{-1/6}$, where $M_A = u_{sw}/v_{Asw}$ is the Alfven Mach number of the upstream solar wind, and using equation (7) of *Borovsky* [2008a]

to obtain $\beta_s = (M_A/6)^{1.92}$, the viscous force on the Earth given by expression (38) can be written entirely in terms of the upstream solar wind parameters n_{sw}, u_{sw}, B_{sw}.

[65] As the Bohm-viscosity driver function $\mathscr{B}$, the power delivered to the magnetosphere by the viscous interaction can be approximated as $P_{\text{Bohm}} \sim u_s F_{v\text{-Bohm}}$: with $u_s = C^{-1} u_{sw}$, expression (38) yields

$$\mathscr{B} = P_{\text{Bohm}} \propto {n_{sw}}^{1/2} {u_{sw}}^{5/2} C^{-1/2} W^{1/2} \tag{39}$$

for the power delivered.

[66] Note that the viscous coupling functions of *Vasyliunas et al*. [1982] are also based on Bohm diffusion acting at the magnetopause. However, the derivation differs from the derivation here. Equation (1) of *Vasyliunas et al*. [1982] for the viscosity is obtained by assuming Bohm diffusion acts, with $v \propto k_B T_i/B$, with $k_B T_i$ taken to be $k_B T_i = m_i {u_{sw}}^2$ for the magnetosheath (which is appropriate for very high Mach numbers where $\beta_s \gg 1$) and with B taken to be given by $B^2 = 8\pi \rho_{sw} {u_{sw}}^2$ (which is the field strength in the magnetosphere near the magnetopause). The Reynolds number Re [*Vasyliunas et al*., 1982, equation (7)] is then take to be $Re = u_{sw} d/v$ (rather than $Re = u_s d/v$). The viscous drag coefficient C_v is assumed to vary as $C_v \propto Re^{-1/2}$ (for the Vasyliunas parameter $b = 0$) and the power delivered by the viscous interaction is taken to be $P = u_{sw} F_v$ (rather than $P = u_s F_v$), yielding, with the Re and v values described in this paragraph, the viscous power [*Vasyliunas et al*., 1982, equation (21)]

$$P_{\text{Vasyl}} \propto {n_{sw}}^{1/2} {u_{sw}}^{5/2} \tag{40}$$

[67] This expression differs by factors of the density-compression ratio of the bow shock and by Mach-number-dependent factors of the magnetosheath plasma beta from expression (39) derived here.

[68] We note that the flow of the solar wind past the Earth is supersonic. For Navier-Stokes fluids with wind speeds comparable to and above the speed of sound, the coefficient of viscous drag C_v (cf. expression (25)) has a Mach-number dependence in addition to a Reynolds number dependence. Above Mach number of unity, the viscous drag coefficient decreases with increasing Mach number [e.g., *Eckert*, 1950; *Lobb et al*., 1955; *Hill*, 1956]. The physical reasons for the Mach-number dependence of the Navier-Stokes drag coefficient are a combination of compressibility of the fluid, changes in the structure of the boundary layers, and thermal transport effects that change the fluid's kinematic viscosity. Whether or not the Mach-number dependence of C_v is the same for plasma flow as Navier-Stokes flow, and whether or not the Mach-number dependence of C_v holds for Bohm diffusion are two open questions. As a fit to multiple experiments measuring the Mach-number dependence of the viscous drag coefficient C_v, equation (12) of chapter 17 in *Hoerner* [1965] yields the empirical factor

$$F = \left(1 + 0.045M^2\right)^{-1/4} \tag{41}$$

that multiplies the drag coefficient C_v. Expression (41) was fit for Mach numbers $1 < M < 5$. Utilizing expression (41), we can write a supersonic version of expression (39) as

$$P_{\text{Bohm}} \propto {n_{sw}}^{1/2} {u_{sw}}^{5/2} C^{-1/2} W^{1/2} \left(1 + 0.045{M_A}^2\right)^{-1/4} \tag{42}$$

[69] Multiplying the Bohm driver $\mathscr{B}$ by the empirical factor $(1 + 0.045M^2)^{-1/4}$ substantially improves its ability to predict variance in all seven geomagnetic indices examined (see section 3.3). However, the physics-based justification for this factor for the supersonic flow of a collisionless magnetized plasma is weak. Hence, the Hoerning supersonic factor will not be used on the Bohm-viscous driver $\mathscr{B}$.

3.2. The Freestream-Turbulence Effect

[70] It has been established that when the solar wind magnetic field is northward (wherein the viscous interaction should dominate over the reconnection interaction), the level of geomagnetic activity is controlled to some degree by the amplitude of magnetic field fluctuations in the upstream solar wind [*Borovsky and Gosling*, 2001; *Borovsky and Funsten*, 2003a; *Borovsky and Steinberg*, 2006a; *Borovsky*, 2006, *D'Amicis et al*., 2007, 2009, 2010, 2011; *Lyons et al*., 2009; *Kim et al*., 2011]. *Borovsky and Funsten* [2003a] tested this observationally being careful to reduce the effect of solar wind turbulence amplitude acting as a proxy for other solar wind parameters.

[71] In this subsection an estimate of the viscous interaction is presented without knowledge of the mechanism of viscosity acting at the magnetopause. To do this we will make use of analogies to Navier-Stokes viscous drag processes verified in wind tunnel experiments. The three factors we will use are (1) the viscous drag on an object in a wind depends on the shape of the object and the Reynolds number of the flow of the wind past the object, (2) ambient turbulence in the wind upstream of the object enhances the viscous drag, and (3) the flow is supersonic.

[72] The first two of these factors have been considered by *Borovsky and Funsten* [2003a], *Borovsky and Steinberg* [2006a], and *Borovsky* [2006], where viscous drag coefficients for the Earth's magnetosphere were derived. We will improve on those calculations in this section and also utilize the third factor.

[73] Experiments in fluid dynamics have shown that ambient turbulence in the fluid upsteam of an object will enhance the viscous drag coupling between the wind and the object [*Blair*, 1983; *Hoffmann and Mohammadi*, 1991; *Volino et al*., 2003]. This is known as the "freestream turbulence effect" [*Kwok and Melbourne*, 1980; *Sullerey and Khan*, 1983; *Pal*, 1985; *Thole and Bogard*, 1996]. The explanation of this effect is that a turbulent fluid has an eddy viscosity v_{eddy} in addition to its kinematic viscosity v_{kin} and this eddy viscosity is much more efficient at transporting momentum across shears in the fluid than is the kinematic viscosity. Hence, the effective Reynolds number of the flow is [*Wu and Faeth*, 1994; *Volino*, 1998]

$$Re = Lu/v_{\text{eddy}} \tag{43}$$

which is much lower than $Re = Lu/v_{\text{kin}}$ as given by expression (27). In agreement with this, examination of high-Reynolds-number flows in wind tunnels with freestream turbulence finds that the morphologies of the flow patterns resemble low-Reynolds-number flows [cf. *Ko and Graf*, 1972; *Castro and Robins*, 1977; *Courchesne and Laneville*, 1982; *Hoffmann*, 1991; *Scholten and Murray*, 1998; *Saathoff and Melbourne*, 1999; *Huang and Lee*, 2000]. The argument underlying the freestream-turbulence effect on the viscous drag

is that whatever the physical viscous mechanisms that couple the momentum of the wind to the surface of the object, the eddy viscosity of the fluid will boost the momentum transfer from the distant fluid to the surface, analogous to the enhancement of momentum transport to the wall in turbulent pipe flow as compared with laminar pipe flow [cf. *Tritton*, 1977, section 22.5].

[74] Combining expressions (24) and (25) and using expression (43) for *Re*, the viscous drag force is

$$F_{v-\text{free}} = 6.5\rho_{sw}{u_{sw}}^2 A\left(v_{\text{eddy}-s}/u_s d\right)^{1/2} \tag{44}$$

where the diameter d of the magnetosphere was taken for L and where the subscripts "sw" and "s" stand for the solar wind and the magnetosheath.

[75] From eq. (7) of *Borovsky* [2006], the eddy viscosity for MHD turbulence in a collisionless plasma can be written

$$v_{\text{eddy}-s} = 0.361\left[\left(\delta{u_s}^2 + \delta{b_s}^2\right)/2\right]^{1/2} L_{bl} \tag{45}$$

[see also *Yoshizawa and Yokoi*, 1996] where L_{bl} is the scale size of an eddy (fluctuation) in the magnetosheath turbulence that has a scale size approximately equal to the thickness of the momentum-exchange boundary layer in the magnetosheath along the magnetosphere, and δu_s and δb_s are the amplitudes of the flow and magnetic field fluctuations in the magnetosheath with scale size L_{bl}. In expression (45), $b = B/(4\pi m_i n)^{1/2}$ is the magnetic field written in Alfven units, where n is the number density of the plasma.

[76] We wish to write the eddy viscosity of the magnetosheath $v_{\text{eddy-}s}$ in terms of upstream solar wind parameters that are continuously measured; so we must estimate how much the solar wind turbulence is amplified as the plasma passes through the bow shock. At the nose of the bow shock the solar wind bulk-flow velocity u_{sw} is slowed such that

$$u_s = C^{-1} u_{sw} \tag{46}$$

where C is the density compression ratio of the shock (which is a function of Mach number) and the number density of the solar wind n_{sw} is increased by

$$n_s = C\, n_{sw} \tag{47}$$

across the shock. The change in amplitude of the solar wind turbulence fluctuations in passing through the bow shock is estimated as follows. The solar wind fluctuations have δB and δu vectors. They are largely Alfvenic (i.e., $\delta u \approx \pm \delta b$) corresponding to outward propagating Alfven waves, especially in the fast wind of coronal-hole origin [*Belcher and Davis*, 1971; *Borovsky*, 2012a, Table 5]. The fluctuations are largely noncompressive with δu and δB both approximately perpendicular to the local mean field B_o [*Horbury et al.*, 2008; *Podesta*, 2009; *Podesta and Tenbarge*, 2012]. As the solar wind plasma passes through the bow shock at the nose, the two components of δB that are perpendicular to the shock normal n will be amplified by a factor of C and the third component of δB that is parallel to the shock normal is unaffected. The one component of δu that is parallel to the shock normal will be reduced by a factor C^{-1} in crossing the shock and the other two components of δu that are perpendicular to the shock normal will be unaffected. The mean field B_o will also be strengthened and bent away from the shock normal direction in crossing the shock, and the mean flow will be slowed (and also deflected [cf. *Walters*, 1964]) in crossing the nose of the bow shock. To calculate the effects of the bow shock on the fluctuations, it is convenient to define the coordinate system according to the directions of the shock normal n and the upstream mean magnetic field B_o. In the plane containing the vectors n and B_o, two directions are in-plane and parallel to the shock normal "$p_{||}$" and in-plane and perpendicular to the shock normal "$p_{\perp}$". The third direction is normal to the plane in the $n \times B_o$ cross-product direction "c." Upstream of the bow shock, the two in-plane components $\delta B_{p||}$ and $\delta B_{p\perp}$ are related to the in-plane component of the amplitude δB_p by

$$\delta B_{p||} = \delta B_p \sin(\theta_{Bn}) \tag{48a}$$

$$\delta B_{p\perp} = \delta B_p \cos(\theta_{Bn}) \tag{48b}$$

where θ_{Bn} is the upstream angle between B_o and the shock normal n. Likewise for $\delta u_{p||}$ and $\delta u_{p\perp}$. In crossing the shock from the solar wind to the magnetosheath, the three components of δB are changed by

$$\delta B_{p\perp} \rightarrow C\delta B_{p\perp} = C\delta B_p \cos(\theta_{Bn}) \tag{49a}$$

$$\delta B_{p||} \rightarrow \delta B_{p||} = \delta B_p \sin(\theta_{Bn}) \tag{49b}$$

$$\delta B_c \rightarrow C\delta B_c \tag{49c}$$

where C is the density compression ratio of the bow shock. Likewise for the three components of the solar wind velocity fluctuations δu, the transformation across the bow shock is

$$\delta u_{p\perp} \rightarrow \delta u_{p\perp} = \delta u_p \cos(\theta_{Bn}) \tag{50a}$$

$$\delta u_{p||} \rightarrow C^{-1}\delta u_{p||} = C^{-1}\delta u_p \sin(\theta_{Bn}) \tag{50b}$$

$$\delta u_c \rightarrow \delta u_c \tag{50c}$$

[77] Thus, the magnetic field energy density $\delta B^2 = (\delta {B_{p\perp}}^2 + \delta {B_{p||}}^2 + \delta {B_c}^2)$ of the magnetic field fluctuations in the magnetosheath is

$$\delta {B_s}^2 = C^2 \delta {B_p}^2 \cos^2(\theta_{Bn}) + \delta {B_p}^2 \sin^2(\theta_{Bn}) + C^2 \delta {B_c}^2 \tag{51}$$

[78] For turbulence in the solar wind that is isotropic normal to B_o, $\delta {B_p}^2 = \delta {B_c}^2 = \delta {B_{sw}}^2/2$: hence, expression (51) becomes

$$\delta {B_s}^2 = \delta {B_{sw}}^2 \left[C^2 + 0.5\left(1 - C^2\right)\, \sin^2(\theta_{Bn})\right] \tag{52}$$

[79] In Alfven units, $\delta b_s = \delta B_s/(4\pi m_i n_s)^{1/2} = \delta B_s C^{-1/2}/(4\pi m_i n_{sw})^{1/2}$, where expression (47) was utilized. With this, expression (52) becomes

$$\delta {b_s}^2 = \delta {b_{sw}}^2 C^{-1} \left[C^2 + 0.5\left(1 - C^2\right) \sin^2(\theta_{Bn})\right] \tag{53}$$

[80] Similarly, the energy density of the velocity fluctuations $\delta u^2 = (\delta {u_{p\perp}}^2 + \delta {u_{p||}}^2 + \delta {u_c}^2)$ of in the magnetosheath is

$$\delta {u_s}^2 = \delta {u_{sw}}^2 \left[1 - 0.5\left(1 - C^{-2}\right) \sin^2(\theta_{Bn})\right] \tag{54}$$

[81] In the solar wind, to within a factor of 2, $\delta u_{sw} \approx \delta b_{sw}$ [cf. *Borovsky*, 2012a, Figure 16]: This is particularly true at

the higher frequency end of the inertial subrange [*Marsch and Tu*, 1990; *Podesta et al*., 2006; *Perez and Boldyrev*, 2010] where the eddies of interest for the present calculation are. Taking $\delta u_{sw} = \delta b_{sw}$, expressions (53) and (54) yield, after some algebra,

$$\delta b_s{}^2 + \delta u_s{}^2 = \delta b_{sw}{}^2 (1 + C)\left[1 - 0.5\left(1 - C^{-2}\right)\, \sin^2(\theta_{Bn})\right] \quad (55)$$

[82] According to expression (55), the amplification of the energy density of the fluctuations in the solar wind $(\delta b_s{}^2 + \delta u_s{}^2)/(\delta b_{sw}{}^2 + \delta u_{sw}{}^2)$ varies from unity at $C = 1$ (which is at a Mach number of unity) to 1.33 (for $C = 4$ and $\theta_{Bn} = 90°$) to 2.5 (for $C = 4$ and $\theta_{Bn} = 0°$). Note in the solar wind that the velocity and magnetic field fluctuations are largely Alfvenic with δu_{sw} in equipartition with δb_{sw} as $\delta b_{sw}/\delta u_{sw} \approx \pm 1$, in the outward traveling (away from the Sun) sense. In passing through the bow shock, δu_{sh} and δb_{sh} are no longer be in equipartition: δb is amplified and δu is reduced. Expressions (53) and (54) yield $\delta \mathrm{b_s}^2/\delta \mathrm{u_s}^2 = C$. For a shock compression ratio $C = 4$, $\delta b_s = \pm 2\ \delta u_s$, independent of θ_{Bn}. This ratio represents counterpropagating Alfven fluctuations [cf. *Alfven and Falthammar*, 1963, section 3.3.1] where a fluctuation with $\delta u \gg \delta b$ is analyzed). The counterpropagating fluctuations in the magnetosheath may represent a more effective turbulence than the unbalanced fluctuations in the solar wind [cf. *Dobrowolny et al*., 1980]. Note also that in crossing the bow shock, some of the Alfvenic fluctuations of the solar wind might be converted into compressional fluctuations in the magnetosheath [cf. *Ip and McKenzie*, 1991].

[83] Inserting expression (55) into expression (45), the eddy viscosity of the magnetosheath is expressed in terms of solar wind fluctuation amplitudes as

$$\nu_{\mathrm{eddy}-s} = 0.255 \delta b_{sw} (1 + C)^{1/2} \left[1 - 0.5\left(1 - C^{-2}\right) \sin^2(\theta_{Bn})\right]^{1/2} L_{bl} \quad (56)$$

[84] Here δb_{sw} must be measured at a wave number corresponding to L_{bl} in the magnetosheath. For a $k^{-5/3}$ power spectrum of magnetic field fluctuations, the amplitude of a fluctuation δB varies as $\delta B \propto k^{-1/3}$ [cf. *Gary and Borovsky*, 2004, Appendix A]. In the solar wind, the fluctuation amplitude is monitored at a fixed timescale τ_m. (For root-mean-square (RMS) values of the vector magnetic field values going into a 1 h average, $\tau_m \sim 20$ min [*Borovsky*, 2006].) The scale size L_m in the magnetosheath that the measurement at τ_m corresponds to is $L_m = \tau_m\, u_s = \tau_m C^{-1} u_{sw}$. Hence, the amplitude in the solar wind corresponding to a spatial scale L_{bl} in the magnetosheath is given by

$$\delta B_{sw} = \delta B_m (L_{bl}/L_m)^{1/3} = \delta B_m L_{bl}{}^{1/3} C^{1/3} / \tau_m{}^{1/3} u_{sw}{}^{1/3} \quad (57)$$

[85] With the use of expression (57), expression (56) for the eddy viscosity at scale L_{bl} in the magnetosheath becomes

$$\nu_{\mathrm{eddy}-s} = 0.072\left\{\delta B_m L_{bl}{}^{4/3} / m_i{}^{1/2} n_{sw}{}^{1/2} \tau_m{}^{1/3} u_{sw}{}^{1/3}\right\} \cdot\ C^{1/3} (1 + C)^{1/2} \left[1 - 0.5\left(1 - C^{-2}\right) \sin^2(\theta_{Bn})\right]^{1/2} \quad (58)$$

where δB_m is the measured level of fluctuations in the solar wind at timescale τ_m.

[86] Inserting expression (58) for $v_{\mathrm{eddy}\text{-}s}$ into expression (44) and using expression (48) to eliminate u_s, writing $\rho_{sw} = m_p n_{sw}$, $\delta b_{sw} = \delta B_{\mathrm{sw}}/(4\pi m_i n_{sw})^{1/2}$, and $\mathrm{A} = \pi d^2/4$,the viscous drag force on the magnetosphere is written as

$$F_{v-\mathrm{free}} = 1.37 m_p{}^{3/4} n_{sw}{}^{3/4} u_{sw}{}^{4/3} d^{3/2} L_{bl}{}^{2/3} dB_m{}^{1/2} t_m{}^{-1/6} C^{2/3} (1 + C)^{1/4} \cdot \left[1 - 0.5\left(1 - C^{-2}\right) \sin^2(\theta_{Bn})\right]^{1/4} \quad (59)$$

[87] Dropping the constants, expression (59) yields

$$F_{v-\mathrm{free}} \propto n_{sw}{}^{3/4} u_{sw}{}^{4/3} \delta B_m{}^{1/2} d^{3/2} G \quad (60)$$

where $G = G(C)$ is given by

$$G = C^{2/3} (1 + C)^{1/4} \left[1 - 0.5\left(1 - C^{-2}\right) \sin^2(\theta_{Bn})\right]^{1/4} \quad (61)$$

[88] The diameter d of the Earth's magnetosphere can be estimated from the pressure-standoff of the solar wind: $d \propto (n_{sw} u_{sw}{}^2)^{-1/6}$ [cf. *Walker and Russell*, 1995, equation (6.21)]. Using this, expression (60) becomes

$$F_{v-\mathrm{free}} \propto n_{sw}{}^{1/2} u_{sw}{}^{5/6} \delta B_m{}^{1/2} G \quad (62)$$

[89] Expression (62) is similar to equation (30) of *Borovsky* [2006], except for the Mach-number-dependent factor of $G(C)$ that accounts for the change in amplitude of the solar wind fluctuations across the bow shock and the slowing down of the magnetosheath flow around the magnetosphere.

[90] Using the parameterization from equation (10) of *Borovsky* [2008a] for the compression ratio of the nose of the bow shock (cf. expression (4f)) $C_\perp = \{2.44 \times 10^{-4} + [1 + 1.38\ \log_e(M_A)]^{-6}\}^{-1/6}$, where $M_A = u_{sw}/v_{Asw}$ is the Alfven Mach number of the upstream solar wind, the viscous force on the Earth given by expression (62) can be written entirely in terms of the upstream solar wind parameters n_{sw}, u_{sw}, B_{sw}, and δB_m.

[91] For the freestream-turbulence viscous driver $\mathscr{B}$, the power delivered to the magnetosphere by the freestream-turbulence viscous interaction will be used. This power can be approximated as $P_{\mathrm{free}} \sim u_s F_{v\text{-free}}$: with $u_s = C^{-1} u_{sw}$, expression (62) yields

$$\mathscr{T} = P_{v-\mathrm{free}} \propto n_{sw}{}^{1/2} u_{sw}{}^{11/6} \delta B_m{}^{1/2} C^{-1} G \quad (63)$$

for the power delivered. The compression ratio C (which also appears in the term $G(C)$) can be parameterized by expression (4d).

[92] The *Hoerner* [1965] experimental factor for supersonic Navier-Stokes flow $F = (1 + 0.045M^2)^{-1/4}$ from expression (41) could also be used to multiply expression (63), yielding

$$P_{v-\mathrm{free}} \propto n_{sw}{}^{1/2} u_{sw}{}^{11/6} \delta B_m{}^{1/2} C^{-1} G \left(1 + 0.045 M_A{}^2\right)^{-1/4} \quad (64)$$

[93] Unlike the case for the Bohm-viscous driver $\mathscr{B}$, multiplying the freestream-turbulence driver $\mathscr{T}$ by the empirical factor $(1 + 0.045 M_A{}^2)^{-1/4}$ only improves the variance predictability for one geomagnetic index, *Dst**. Since it cannot be well justified physically for the solar wind flow, the

Hoerner supersonic factor will not be employed with the driver function $\mathscr{F}$.

3.3. Examining the Viscous Drivers

[94] In the fourth and fifth columns of Table 1, linear correlation coefficients between the viscous drivers $\mathscr{B}$ and $\mathscr{F}$ and the seven geomagnetic indices are collected. Since the viscous interaction is most dominant when the reconnection driver $\mathscr{G}$ is nearly off, the viscous drivers should have their largest correlations with the geomagnetic indices when the IMF clock angle θ_{clock} is near zero (northward IMF). Likewise, when the clock angle is unrestricted, the reconnection driver $\mathscr{G}$ should dominate the variation of the geomagnetic indices and the correlations between the viscous drivers and geomagnetic activity should be weak (since the viscous drivers are not controlling most of the variation of the indices). However, this is not the case. In the fourth and fifth columns of Table 1, two sets of correlation coefficients are displayed: the first number is the correlation coefficient for northward IMF ($0° \le \theta_{\text{clock}} \le 20°$) and the second number is the correlation coefficient for all values of θ_{clock}. If the viscous driving functions $\mathscr{B}$ and $\mathscr{F}$ were only describing the viscous interaction, the first numbers in the table would be much larger than the second numbers. For the Bohm driver $\mathscr{B}$, the first values are definitely larger than the second values: for the freestream-turbulence driver $\mathscr{F}$, the second values are on average slightly larger than the first values. The fact that the drivers $\mathscr{B}$ and $\mathscr{F}$ show strong correlation with the geomagnetic indices for all values of θ_{clock} indicates that the $\mathscr{B}$ and $\mathscr{F}$ drivers act as a proxy for the reconnection interaction; i.e., they have an ability to quantify the strength of the reconnection driver (in addition to being able to quantify the strength of the viscous interaction). This proxy effect is stronger for the freestream-turbulence driver $\mathscr{F}$ than it is for the Bohm-viscosity driver $\mathscr{B}$.

[95] Correspondingly, it is likely the case that the reconnection driver $\mathscr{G}$ also describes in part the strength of the viscous interaction.

[96] This proxy effect comes about from similarities in the functional forms of $\mathscr{G}$, $\mathscr{B}$, and $\mathscr{F}$: i.e., all increase with increasing u_{sw}. This being the case, the viscous drivers $\mathscr{B}$ and $\mathscr{F}$ are not orthogonal to the reconnection driver $\mathscr{G}$: i.e., they are not independent of each other. For all values of the clock angle θ_{clock}, the linear correlation coefficient between $\mathscr{G}$ and $\mathscr{B}$ is +0.179, the linear correlation coefficient between $\mathscr{G}$ and $\mathscr{F}$ is +0.351, and the linear correlation coefficient between $\mathscr{B}$ and $\mathscr{F}$ is +0.748. $\mathscr{G}$ and $\mathscr{B}$ are more independent of each other than are $\mathscr{G}$ and $\mathscr{F}$.

[97] Examining the northward IMF (first) number in the third and fourth columns of Table 1, the $\mathscr{B}$ and $\mathscr{F}$ driver functions have similar correlation coefficients with each of the seven geomagnetic indices. The correlations are particularly high with the 1 h lagged *Kp* index and particularly low with the PCI index.

4. Assessing the Magnetospheric Driver Functions

[98] The reconnection-coupled MHD generator $\mathscr{G}$ and the viscous drivers $\mathscr{B}$ and $\mathscr{F}$ are put together by addition, yielding two solar wind driver functions for the Earth's magnetosphere: $\mathscr{G}+\mathscr{B}$ and $\mathscr{G}+\mathscr{F}$. The values of $\mathscr{G}$, $\mathscr{B}$, and $\mathscr{F}$ come from expressions (23), (39), and (63). In this section those two drivers are statistically analyzed to gain an increased understanding of how solar wind/magnetosphere coupling works.

4.1. Correlation Coefficients

[99] The Pearson linear correlation coefficients [*Bevington and Robinson*, 1992, equation (11.17)] between the two combined driver functions $\mathscr{G}+\mathscr{B}$ and $\mathscr{G}+\mathscr{F}$ and the seven geomagnetic indices appear in Table 1. In the bottom row of the table is a seven-index sum of the correlations. Note that there is one adjusted free parameter in every correlation between $\mathscr{G}+\mathscr{B}$ and each index and between $\mathscr{G}+\mathscr{F}$ and each index that arises as follows. The derivation of the reconnection-coupled MHD generator does not calculate the level of the *AE* index as a function of upstream solar wind parameters; it calculates the total amount of dayside reconnection: There is an unknown numerical factor that connects the amount of reconnection with the level of the *AE* index. Likewise the derived viscous coupling does not calculate the level of the *AE* index; it calculates the total power delivered to the outer magnetosphere by viscous processes: an unknown numerical factor connects the outer magnetosphere power with the level of the *AE* index. When the correlation coefficient between $\mathscr{F}$ and *AE* or between $\mathscr{B}$ and *AE* is calculated, these unknown numerical factors are irrelevant. But when $\mathscr{G}$ and $\mathscr{B}$ are combined to form $\mathscr{G}+\mathscr{B}$, the two numerical factors are not irrelevant. (In fact $\mathscr{G}$ has different units than $\mathscr{B}$ and $\mathscr{F}$: $\mathscr{G}$ has units of electrical potential and $\mathscr{B}$ and $\mathscr{F}$ have units of power.) To fix this, a parameter "*a*" must be added creating $\mathscr{G}+a\mathscr{B}$, with the value of *a* adjusted to optimize the correlation of $\mathscr{G}+a\mathscr{B}$ with *AE*. Each time in Table 1 that $\mathscr{G}+\mathscr{B}$ or $\mathscr{G}+\mathscr{F}$ is correlated with one of the seven indices, a hidden parameter "*a*" has been adjusted.

[100] In Table 1 the correlation coefficients between the drivers and the geomagnetic indices are displayed. It is seen that the combined drivers $\mathscr{G}+\mathscr{B}$ and $\mathscr{G}+\mathscr{F}$ more accurately describe the variance of the indices than do the individual drivers $\mathscr{G}$, $\mathscr{B}$, or $\mathscr{F}$. The seven-index sums of the correlation coefficients in the bottom row clearly indicate this improvement.

[101] In Table 2 the mean absolute errors in the ability of the two solar wind driver functions $\mathscr{G}+\mathscr{B}$ and $\mathscr{G}+\mathscr{F}$ to predict the seven geomagnetic indices are assessed. In each case for a given driver function $\mathscr{D}$ and a given geomagnetic index $\mathscr{I}$, the analysis proceeds as follows: (1) the parameter "*a*" is adjusted in $\mathscr{G}+a\mathscr{B}$ or $\mathscr{G}+a\mathscr{F}$ to obtain the highest linear correlation coefficient between the driver $\mathscr{D}$ and the index $\mathscr{I}$, (2) a least squares linear regression fit to the index $\mathscr{I}$ as a function of the driver $\mathscr{D}$ is made with slope *m* and intercept *b*, which is $\mathscr{I}_{\text{fit}} = m\mathscr{D} + b$, (3) the individual error $\mathscr{E}$ of the driver fit $m\mathscr{D}+b$ for each 1 h data point is calculated $\mathscr{E} = (m\mathscr{D}+b) - \mathscr{I}$ from individual values of I and $\mathscr{D}$, and (4) statistics of the absolute values of the errors $|\mathscr{E}|$ are performed. In Table 2 the mean value of the absolute errors $|\mathscr{E}|$ is collected between the two driver functions and the seven geomagnetic indices. An examination of the error values in Table 2 finds that as was the case with the correlation coefficients in Table 1, the two functions $\mathscr{G}+\mathscr{B}$ and $\mathscr{G}+\mathscr{F}$ do similarly well at describing the geomagnetic indices.

4.2. Nonlinear Driver Functions

[102] In Figure 7 (top) the 1 h lagged *AE* index is plotted as a function of the solar wind driver $\mathscr{G}+\mathscr{B}$: the black points are the individual hours of data from 1980–2012. To show

Table 2. Mean Absolute Errors Between Seven Geomagnetic Indices and Linear Regression Fits to Those Seven Indices by the Two Solar Wind Drivers $\mathcal{G}+\mathcal{B}$ and $\mathcal{G}+\mathcal{F}$

	Number of Data Points	$\mathcal{G}+\mathcal{B}$ Error	$\mathcal{G}+\mathcal{F}$ Error
AE 1 h lagged	189,320	86.3 nT	88.3 nT
AU 1 h lagged	189,320	34.3 nT	34.0 nT
−*AL* 1 h lagged	189,320	65.1 nT	66.8 nT
PCI	198,000	0.455	0.462
Kp 1 h lagged	198,460	0.685	0.670
−MBI 1 h lagged	121,076	0.866°	0.885°
−*Dst** 2 h lagged	191,142	12.0 nT	11.9 nT

the trend underlying the black points, the red points are a 300-point running average of the black points. As can be seen by the red curve, the response of AE_1 to the driver $\mathcal{G}+\mathcal{B}$ is not linear: There is a strong flattening of the response at low values of $\mathcal{G}+\mathcal{B}$. All three auroral electrojet indices *AE*, *AU*, and *AL* show this flattening of the response at low values of $\mathcal{G}+\mathcal{B}$. The Dst^*_2 index shows a modest weakening of the response at low $\mathcal{G}+\mathcal{B}$, and the Kp_1 and PCI indices show slight weakenings at low $\mathcal{G}+\mathcal{B}$ values. The MBI_1 index shows no change at low $\mathcal{G}+\mathcal{B}$ values but shows a bend at high $\mathcal{G}+\mathcal{B}$ values.

[103] The response of the geomagnetic indices to the solar wind driver can be made more linear by fitting the index as a nonlinear function of the driver. In Figure 7 (bottom) such a nonlinear fit is used to straighten out the response: the nonlinear fit used is

$$NL(\mathcal{G}+\mathcal{B}, AE_1) = 1.43\times10^4 \exp((\mathcal{G}+\mathcal{B})/168)/[526+27.2\exp((\mathcal{G}+\mathcal{B})/168))] \quad (65)$$

[104] This nonlinear function approximately has the functional form $NL(\mathcal{G}+\mathcal{B}, AE_1) \approx \min(526, 27.2\exp((\mathcal{G}+\mathcal{B})/168))$. As noted in Figure 7 (bottom), the linear correlation coefficient between $NL(\mathcal{G}+\mathcal{B}, AE_1)$ and AE_1 is +0.812, slightly higher than the linear correlation coefficient of +0.797 between $\mathcal{G}+\mathcal{B}$ and AE_1. The $\exp((\mathcal{G}+\mathcal{B})/168)$ driving is flat near $\mathcal{G}+\mathcal{B}\sim0$, becomes linear around $\mathcal{G}+\mathcal{B}=168$, and eventually levels off at high values of $\mathcal{G}+\mathcal{B}$ to 526.

[105] In Table 3 the linear correlation coefficients between other nonlinear fits and the AE_1 and Kp_1 indices are displayed. The nonlinear fits are

$$NL(\mathcal{G}+\mathcal{B}, Kp_1) = 14.6\,(\mathcal{G}+\mathcal{B})^{2.01}/\left[16.6+0.877(\mathcal{G}+\mathcal{B})^{2.01}\right] \quad (66a)$$

$$NL(\mathcal{G}+\mathcal{F}, AE_1) = 2.33\times10^4 \exp((\mathcal{G}+\mathcal{F})/162)/[645+36.2\exp((\mathcal{G}+\mathcal{F})/162)] \quad (66b)$$

$$NL(\mathcal{G}+\mathcal{F}, Kp_1) = 10.7(\mathcal{G}+\mathcal{F})^{1.67}/\left[11.4+0.936(\mathcal{G}+\mathcal{F})^{1.67}\right] \quad (66c)$$

[106] As seen in Table 3, using the nonlinear functional forms improves the Pearson linear correlation coefficients between the solar wind drivers and the geomagnetic indices.

4.3. Examination of Time Series

[107] Two examples of combined drivers describing the *AE* index appear in Figures 8 and 9. The two examples are for very different types of geomagnetic activity.

[108] In Figure 8 the *AE* index (no time lag) is plotted in black for 12 days in September 2003. A coronal interaction region passes the Earth from early on Day 259 to about midday on Day 260, as labeled in the figure. The Alfven Mach number $M_A = u_{sw}/v_{Asw}$ of the upstream solar wind is plotted in orange. The Mach number is high, except during the passage of the CIR where $M_A \sim 4$. The CIR stream interface (the maximum of the vorticity of the solar wind plasma) passed the Earth at about 1:30 UT on Day 260 [cf. *Borovsky and Denton*, 2010b, Table 1]. Prior to the stream interface the solar wind plasma was of helmet-streamer origin, with a toward-to-away sector reversal passing the Earth at about 20:00 UT on Day 258 in the streamer plasma. At this time of the year (fall), away sectors tend to be Russell-McPherron

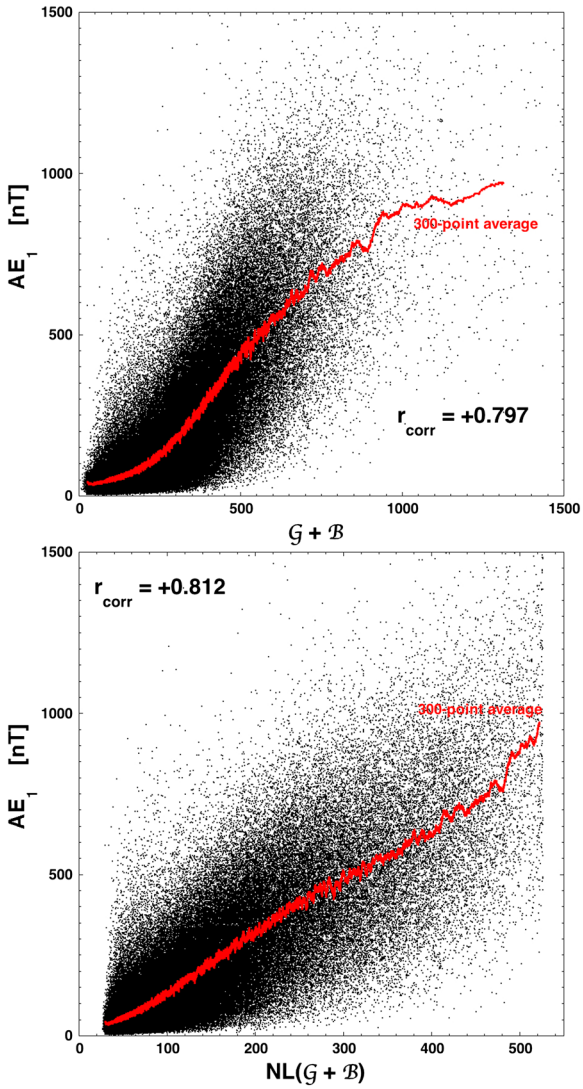

Figure 7. The AE_1 index is plotted as a function of the (top) $\mathcal{G}+\mathcal{B}$ driver and the (bottom) nonlinear $NL(\mathcal{G}+\mathcal{B})$ driver. The black points are the individual 1 h data points and the red points are 300-point running averages of the black points.

Table 3. Linear Correlation Coefficients Between the Solar Wind Drivers $\mathcal{G}+\mathcal{B}$ and $\mathcal{G}+\mathcal{F}$ and the Nonlinear Versions of the Solar Wind Drivers $NL(\mathcal{G}+\mathcal{B})$ and $NL(\mathcal{G}+\mathcal{F})$ and the Geomagnetic Indices *AE* and *Kp*

	$\mathcal{G}+\mathcal{B}$	$\mathcal{G}+\mathcal{F}$	$NL(\mathcal{G}+\mathcal{B})$	$NL(\mathcal{G}+\mathcal{F})$
AE 1 h lagged	0.797	0.782	0.812	0.799
Kp 1 h lagged	0.778	0.781	0.789	0.812

geomagnetically effective and toward sectors tend to be Russell-McPherron ineffective [*Russell and McPherron*, 1973]. After the passage of the stream interface, the solar wind plasma is of coronal-hole origin: a high-speed stream followed by the high-speed-stream trailing edge. Prior to the sector reversal there is a classic "calm before the storm" [*Borovsky and Steinberg*, 2006b] beginning at about 15:00 UT on Day 252 and ending at about 17:00 UT on Day 258. A storm commences (as determined by MBI crossing 60.7°) at about 2:00 UT on Day 259. The storm lasts for about 5 days. The nonlinear $NL(\mathcal{G}+\mathcal{B})$ driver (expression (65)) is plotted in red and the nonlinear $NL(\mathcal{G}+\mathcal{F})$ driver (expression (66b)) is plotted in blue. Also plotted in green is the *Newell et al.* [2007] universal driver function. As can be seen in Figure 8, at shorter timescales as the solar wind driver functions change amplitude, the *AE* index responds. The high peaks in *AE* are in general not captured by the behavior of the driver functions; the troughs in *AE* tend to be better captured than the peaks. The low-frequency overall level of activity seems to be well captured by the drivers.

[109] In Figure 9 *AE* is plotted (with no lag) in black for 3 days during which a coronal mass ejection and its complex sheath passed the Earth in November 2000. The coronal mass ejection contained a magnetic cloud moving with a mean speed of 530 km/s (Cloud 54 in the *Lepping et al.* [2005] catalog). The magnetic field orientation inside the cloud was south then north with a high field strength (~20 nT).

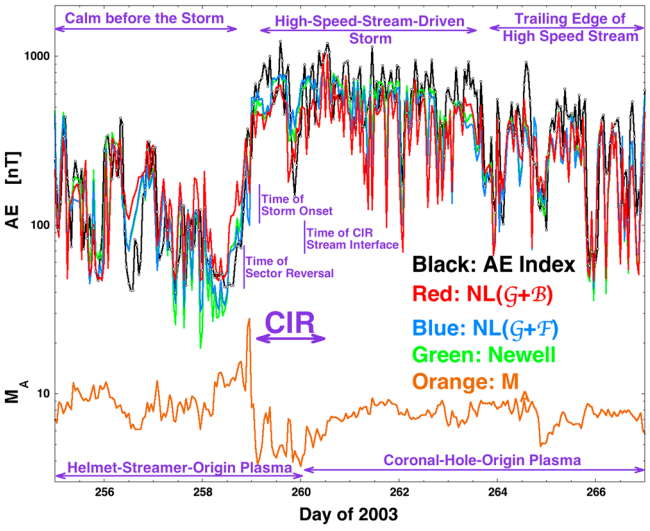

Figure 8. For 12 days in September 2003, the *AE* index and three driver functions are plotted. During this interval, a CIR passed the Earth, preceded by helmet-streamer-origin plasma, and followed by coronal-hole-origin plasma, a calm then a storm resulted.

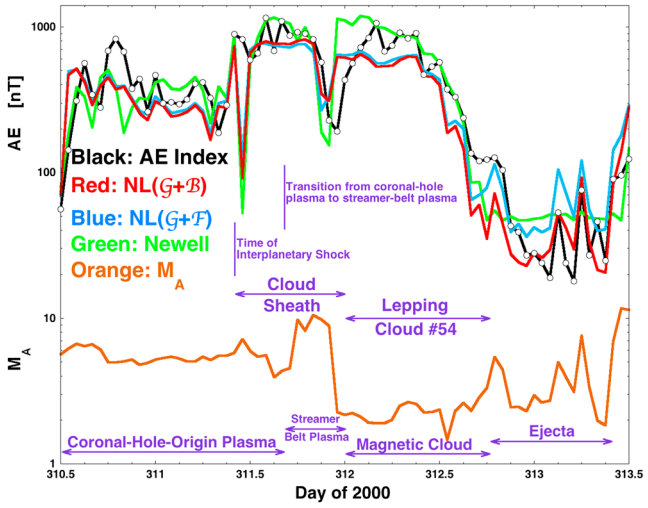

Figure 9. For 3 days in November 2000, the *AE* index and three drivers are plotted. During this interval, a magnetic cloud and its sheath passed the Earth, preceded by coronal-hole-origin plasma, and followed by ejecta-like plasma.

The cloud drove an interplanetary shock into the upstream solar wind: The shock passed the Earth at about 10:00 UT on Day 311. Between the shock and the front edge of the magnetic cloud is the CME sheath. The leading portion of this sheath (from 10:00 UT to 17:00 UT on Day 311) was shocked coronal-hole-origin plasma (as determined from its high proton-specific entropy and low O^{7+}/O^{6+} and C^{6+}/C^{5+} charge-state ratios [*Siscoe and Intriligator*, 1993; *Zhao et al.*, 2009]); the latter portion of this sheath (from 17:00 UT to 23:00 UT on Day 311) was shocked streamer-belt-origin plasma (as determined from its low proton-specific entropy and high O^{7+}/O^{6+} and C^{6+}/C^{5+} charge-state ratios [*Wang et al.*, 2012]). Ahead of the interplanetary shock the plasma was of coronal-hole origin with an IMF that was Parker-spiral orientation with an away-sector polarity. For about 16 h after the magnetic cloud passed, the plasma was ejecta-like, as determined from the presence of bidirectional electron streaming [*Gosling et al.*, 1987] and from a magnetic field inclined strongly out of the ecliptic plane (northward) [*Borovsky*, 2010a]. At about 10:00 UT on Day 312, the ejecta ceased and the plasma was of streamer-belt origin with a toward-sector Parker-spiral orientation. In Figure 9 the nonlinear $NL(\mathcal{G}+\mathcal{B})$ driver is plotted in red, the nonlinear $NL(\mathcal{G}+\mathcal{F})$ driver is plotted in blue, and the *Newell et al.* [2007] universal driver function is plotted in green. As can be seen, the *AE* index responds to the solar wind drivers with about a 1 h lag. *AE* and the drivers track each other for the low-frequency trends. The individual peaks and troughs of *AE* usually correspond to peaks and troughs in the driver functions. Note the strong deviation between all of the solar wind driver functions and *AE* at 11:00 UT on Day 311: An examination of the hourly averaged solar wind data for that hour found that the IMF clock angle based on the hourly averaged magnetic field vector was strongly northward ($\theta_{clock} = 26°$) whereas the actual magnetic field orientation during that hour had substantial variation and was not typically strongly northward. Note the variation in the Alfven Mach number of the solar wind (orange curve) during this 3 day interval,

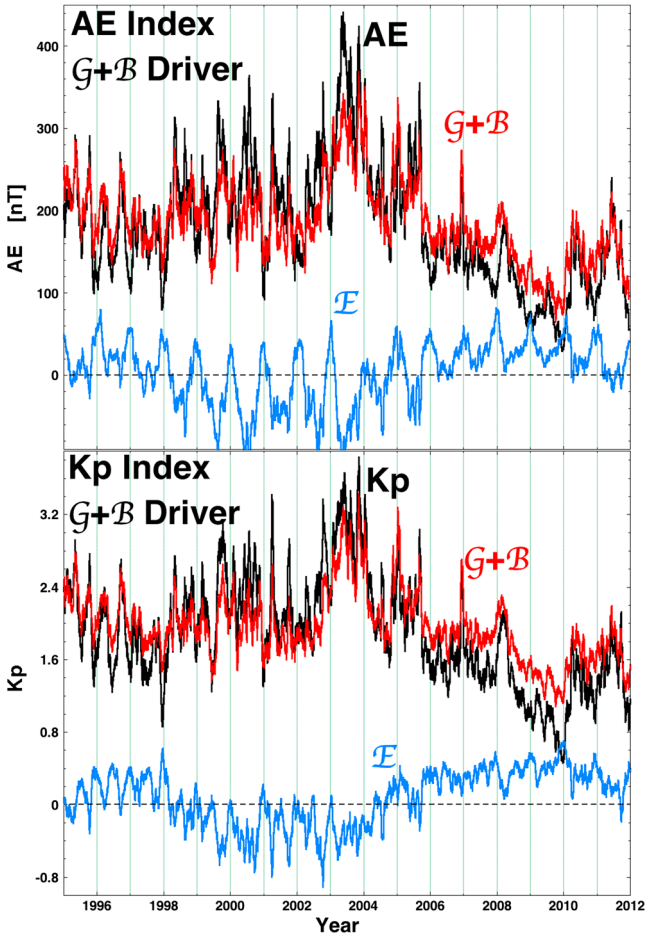

Figure 10. For the years 1995–2011, (top) the $\mathcal{G}+.\mathcal{B}$ driver function and the *AE* index and (bottom) the $\mathcal{G}+.\mathcal{B}$ driver and the *Kp* index are plotted. The difference (error) $\mathcal{E}$ between the index and the driver is plotted in blue in both panels. All curves are 27 day running averages of 1 h data.

with very low Mach numbers ($M_A = 1.4$–2.8) for the cloud plasma and modest Mach numbers for the ejecta.

[110] The trends of the solar wind driver functions $\mathcal{G}+.\mathcal{B}$ and $\mathcal{G}+.\mathcal{F}$ through the solar cycle are shown in Figures 10 and 11: the top panels are *AE* and linear-regression fits of the driver functions to AE_1 and the bottom panels are *Kp* and linear regression fits of the driver functions to Kp_1. In blue the errors $AE_{\text{fit}} - AE_1$ and $Kp_{\text{fit}} - Kp_1$ between the measured values of the indices and the linear regression fits are plotted. All curves in Figures 10 and 11 are 27 day running averages of 1 h values. Clear solar cycle dependences are seen, with the solar wind driver functions overpredicting the indices in the declining phases of the solar cycles (years 1996 and 1997 and years 2006 to 2010), where the error tends to be greater than 0. In the solar-maximum years 1998 to 2003, the solar wind driver functions tend to underpredict the geomagnetic indices. Note an annual effect to the *AE* index and a semiannual effect to the *Kp* index; for *AE*, the error tends to peak at year's end (winter) and have minima in the middle of each year (summer), whereas for *Kp*, the error has two peaks per year (winter and summer) and two minima per year (spring and fall) [*Murayama*, 1974; *Hibberd*, 1985].

4.4. Analysis of Autocorrelation Functions

[111] The autocorrelation function is a measure of persistence in the time series. In Figures 12–14 the autocorrelation functions of the $NL(\mathcal{G}+.\mathcal{B})$ and $NL(\mathcal{G}+.\mathcal{F})$ drivers, the *AE* index, and pertinent solar wind parameters are examined. The autocorrelation function $A(\tau)$ of a time series $s(t)$ of time t is constructed by first subtracting off the average value of the time series $\langle s(t)\rangle$ to produce a new function $S(t) = s(t) - \langle s(t)\rangle$; $\mathcal{A}(\tau)$ of $s(t)$ is then

$$\mathcal{A}(\tau) = \int S(t)S(t-t)\mathrm{d}t \Big/ \int S(t)S(t)\mathrm{d}t \qquad (67)$$

where the integration is over the data interval chosen. At $\tau = 0$, $A(0) = 1$.

[112] The autocorrelation functions of $NL(\mathcal{G}+.\mathcal{B})$ (red points), $NL(\mathcal{G}+.\mathcal{F})$ (green points), and *AE* (black curve) are plotted in Figure 12 from lags $\tau = 0$ to $\tau = 200$ h. All have 1 h resolution in τ (since they are created from data with 1 h temporal resolution). In Figure 12 the autocorrelation functions of the *AE* index and the two drivers all decrease from unity together at early times. At time lags of 12 h or more the autocorrelation function of the *AE* index is falling off slower than the autocorrelation functions of the $NL(\mathcal{G}+.\mathcal{B})$ and $NL(\mathcal{G}+.\mathcal{F})$ drivers: at these timescales the time series of

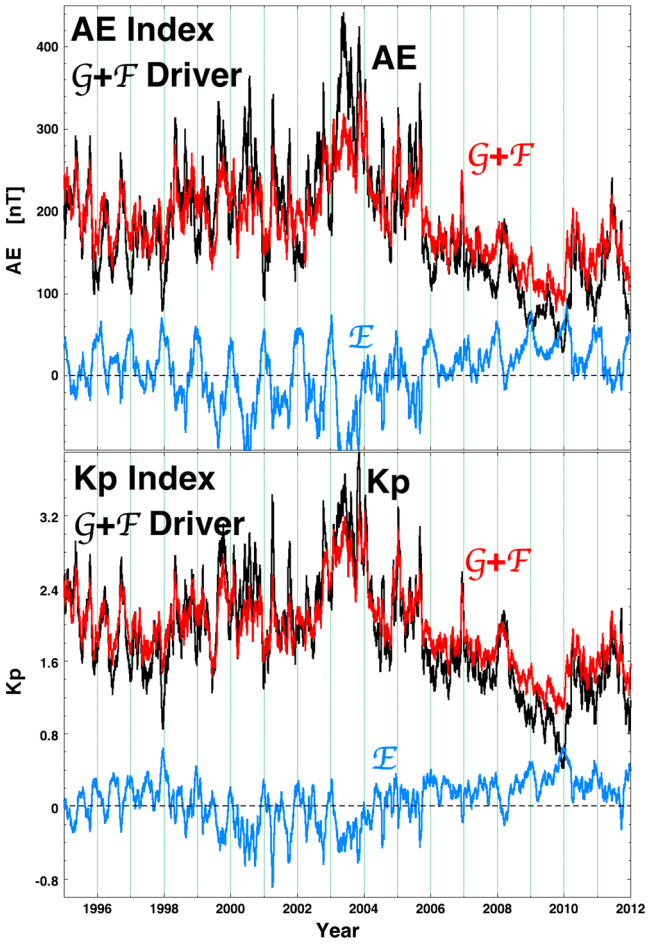

Figure 11. For the years 1995–2011 the $\mathcal{G}+.\mathcal{F}$ driver function and the *AE* index (top) and the $\mathcal{G}+.\mathcal{F}$ driver and the *Kp* index (bottom) are plotted. The difference (error) $\mathcal{E}$ between the index and the driver is plotted in blue in both panels. All curves are 27-day running averages of 1 h data.

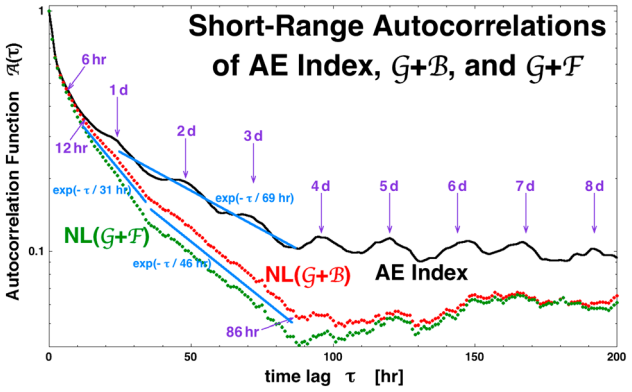

Figure 12. The autocorrelation functions of the *AE* index (black), the $NL(\mathcal{G}+.\mathcal{B})$ driver (red), and the $NL(\mathcal{G}+.\mathcal{F})$ driver (green) are plotted. Specific values of the time lag are labeled in purple and specific exponential curves are shown in blue.

AE has more persistence than the time series of $NL(\mathcal{G}+.\mathcal{B})$ and $NL(\mathcal{G}+.\mathcal{F})$. Note the 1 day periodicity of the *AE* index shown by repeated peaks in the autocorrelation function at integer numbers of days as indicated by the blue arrows. This periodicity is seen in the *AE* autocorrelation function out to about 16 days (not shown). This 1 day periodicity is not seen in the autocorrelation functions of $NL(\mathcal{G}+.\mathcal{B})$ and $NL(\mathcal{G}+.\mathcal{F})$. In Figure 12 some persistence timescales are indicated with the blue exponential curves; the autocorrelation of *AE* has a predominant $\exp(-\tau/69\text{h})$ falloff, and the autocorrelations of the $NL(\mathcal{G}+.\mathcal{B})$ and $NL(\mathcal{G}+.\mathcal{F})$ drivers have $\exp(-\tau/31\text{h})$ and $\exp(-\tau/46\text{h})$ falloffs. At $\tau \sim 86$ h, all three autocorrelation functions transition into a flat longer timescale persistence, which is explored in Figure 13.

[113] Figure 13 shows the autocorrelation functions of the $NL(\mathcal{G}+.\mathcal{B})$ driver, the $NL(\mathcal{G}+.\mathcal{F})$ driver, and the *AE* index for time shifts τ up to 2.28 years with a logarithmic axis for τ. The change in the autocorrelation functions at $\tau \sim 86$ h is clearly seen. Note the peaks in all three autocorrelations at 27 days and multiples of 27 days. These represent recurrence of the solar wind plasma types [cf. *Borovsky*, 2012a, Figure 20] with the ~27 day solar rotation. Note the 1 year periodicity in the *AE* index indicated by the localized peaks in the *AE* autocorrelation function at time lags $\tau = 1$ year

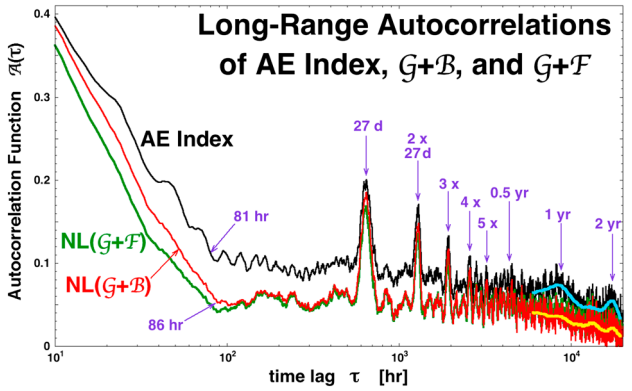

Figure 13. The autocorrelation functions of the *AE* index (black), the $NL(\mathcal{G}+.\mathcal{B})$ driver (red), and the $NL(\mathcal{G}+.\mathcal{F})$ driver (green) are plotted. Specific values of the time lag are labeled in purple.

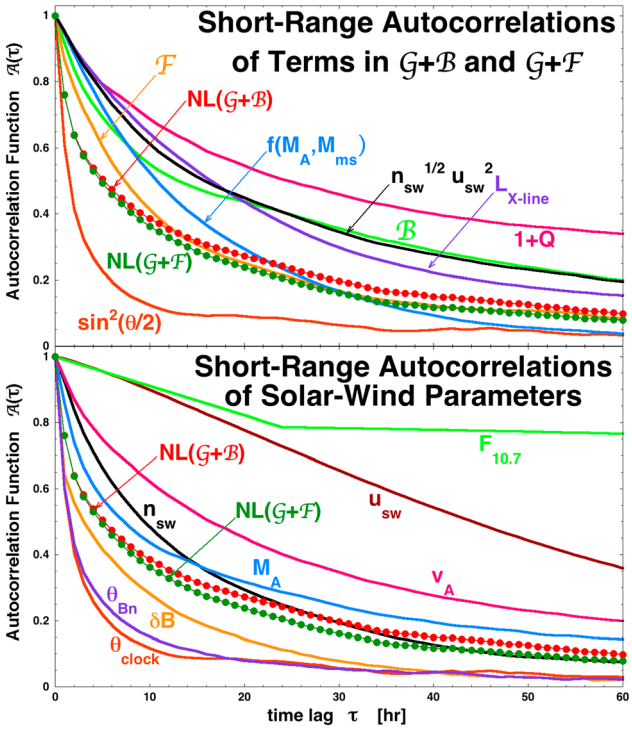

Figure 14. The autocorrelation functions of the $NL(\mathcal{G}+.\mathcal{B})$ driver and the $NL(\mathcal{G}+.\mathcal{F})$ driver are plotted as the red points and the green points in both panels. (top) The autocorrelation functions of various components of the $\mathcal{G}+.\mathcal{B}$ and $\mathcal{G}+.\mathcal{F}$ drivers are plotted. (bottom) The autocorrelation functions of several pertinent solar wind parameters are plotted.

and $\tau = 2$ years that are not in the $NL(\mathcal{G}+.\mathcal{B})$ and $NL(\mathcal{G}+.\mathcal{F})$ autocorrelation functions; this is highlighted by the light-blue 54 day average of the black *AE* index autocorrelation and the yellow 54 day average of the red $NL(\mathcal{G}+.\mathcal{B})$ autocorrelation. These peaks in the *AE* autocorrelation function are probably owed to the tilt of the Earth's North Pole toward and away from the Sun in summer and winter.

[114] In Figure 14 the autocorrelation functions of the nonlinear $NL(\mathcal{G}+.\mathcal{B})$ (red points) and $NL(\mathcal{G}+.\mathcal{F})$ (green points) drivers are compared with the autocorrelation functions of the various terms in $\mathcal{G}+.\mathcal{B}$ and $\mathcal{G}+.\mathcal{F}$ (top) and with the autocorrelation functions of key solar wind parameters (bottom). Measuring the autocorrelation time as the time lag required for the autocorrelation to drop to $1/e = 0.368$ of its original value, the $NL(\mathcal{G}+.\mathcal{B})$ driver has and autocorrelation time of ~12 h and the $NL(\mathcal{G}+.\mathcal{F})$ driver has an autocorrelation time of ~10 h. The three terms of the R_2 local reconnection rate (cf. expressions (3) and (6)) are (1) $n_{sw}^{1/2}u_{sw}^{2}$ (the ram pressure driver of reconnection and the solar wind density term in the Alfven speed) plotted in black, (2) $f(M_A,M_{ms})$ (the plasma β modification of the magnetosheath magnetic field strength) plotted in blue, and (3) $\sin^2(\theta_{clock}/2)$ (which is an approximation to the dependence of R_2 on the IMF clock angle θ_{clock} and the reconnection X line tilt angle α plotted in dark orange: $n_{sw}^{1/2}u_{sw}^{2}$ has an autocorrelation time of ~27 h, $f(M_A,M_{ms})$ has an autocorrelation time of ~16 h, and $\sin^2(\theta_{clock}/2)$ has an autocorrelation time of ~3 h. The reconnection-coupled generator G is the rate R_2 is multiplied by the length of the reconnection X line $L_{X\ line}$ (plotted in

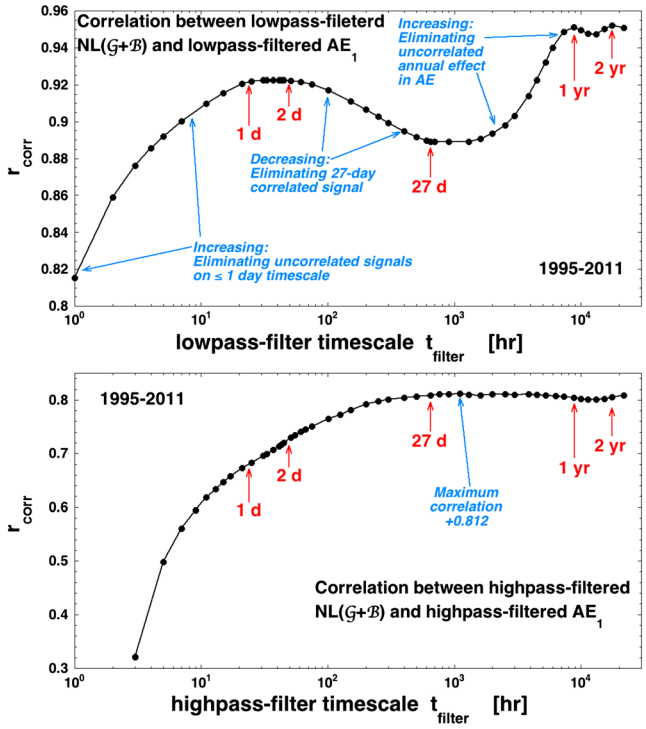

Figure 15. The correlation coefficients between AE_1 and $NL(\mathcal{G}+.\mathcal{B})$ are plotted as functions of filter timescales (top) when the two time series are both low-pass filtered and (bottom) when they are both high-pass filtered.

purple) and divided by $1+Q$ (plotted in pink). $L_{X\ line}$ and $1+Q$ have autocorrelation times of ~25 h and ~48 h. Note that the autocorrelation function of $1+Q$ does not fall to small values in Figure 14: Q has strong solar-cycle-timescale correlations. In light green, the autocorrelation function of the Bohm viscosity driver $.\mathcal{B}$ (expression (39)) is plotted and in orange the autocorrelation of the freestream-turbulence viscosity driver $.\mathcal{F}$ (expression (63)) is plotted; the $1/e$ autocorrelation time of $.\mathcal{B}$ is ~29 h and the autocorrelation time of $.\mathcal{F}$ is ~13 h. The autocorrelation times of $NL(\mathcal{G}+.\mathcal{B})$ and $NL(\mathcal{G}+.\mathcal{F})$ are shorter than the autocorrelation times of all of the components plotted in Figure 14 (top) except for $\sin^2(\theta_{clock}/2)$ which has a correlation time of 3 h: the short correlation times (12 h and 10 h) of $NL(\mathcal{G}+.\mathcal{B})$ and $NL(\mathcal{G}+.\mathcal{F})$ are owed mostly to the rapid changes of $\sin^2(\theta_{clock}/2)$. Note in Figure 14 that the shapes of the $NL(\mathcal{G}+.\mathcal{B})$ and $NL(\mathcal{G}+.\mathcal{F})$ autocorrelation functions are not determined by the temporal behavior of any single term of $\mathcal{G}+.\mathcal{B}$ or $\mathcal{G}+.\mathcal{F}$; the temporal behavior is a product of several terms.

[115] In Figure 14 (bottom) the autocorrelation functions of the fundamental plasma parameters that enter into the $NL(\mathcal{G}+.\mathcal{B})$ and $NL(\mathcal{G}+.\mathcal{F})$ drivers are plotted [see also *Borovsky*, 2012a, Figure 20 and Table 6]. The IMF orientation angles θ_{clock} (dark orange) and θ_{Bn} (purple) have short correlation times of ~3 h, the amplitude of the solar wind magnetic field fluctuations δB (orange) has a correlation time of ~7 h, the solar wind speed u_{sw} has a relatively long correlation time of ~59 h, the autocorrelation of the $F_{10.7}$ flux (light green, with 1 day time resolution) is dominated by solar cycle-timescale variations, and the parameters n_{sw} (black), M_A (blue), and v_A (pink) have correlation times of 16 h, 16 h, and 28 h. Again, the shapes of the autocorrelation functions of $NL(\mathcal{G}+.\mathcal{B})$ and $NL(\mathcal{G}+.\mathcal{F})$ are not dominated by any one solar wind parameter.

4.5. Band-Pass Filtering

[116] Low-pass and high-pass filters are applied to the time series $AE_1(t)$ and the solar wind driver function $NL(\mathcal{G}+.\mathcal{B})$, and the behavior of the correlation coefficient between AE_1 and $NL(\mathcal{G}+.\mathcal{B})$ is examined as functions of the filter cutoff timescales t_{filter}.

[117] In Figure 15 (top) the linear correlation coefficient r_{corr} between AE_1 and the nonlinear $NL(\mathcal{G}+.\mathcal{B})$ driver is plotted as a function of the low-pass-filter timescale t_{filter} [see also *Finch and Lockwood*, 2007]. For example, at a filter timescale $t_{filter}=100$ h, the correlation coefficient is +0.917. This data point is obtained by cross-correlating a 100 h running average of the AE_1 time series with a 100 h running average of the $NL(\mathcal{G}+.\mathcal{B})$ time series; the 100 h running averaging removes variations in both time series with timescales shorter than about 100 h and only variations with timescales slower than 100 h remain. Examining the curve in Figure 15 (top), at $t_{filter}=1$ h (unfiltered 1 h resolution data) the correlation coefficient is $r_{corr}=+0.815$ (for the years 1995–2001). As the low-pass-filter timescale t_{filter} increases from 1 h, the correlation coefficient between AE_1 and the $\mathcal{G}+.\mathcal{B}$ driver function increases: This increase in correlation is owed to the removal of high-frequency uncorrelated information between AE_1 and $NL(\mathcal{G}+.\mathcal{B})$. This improvement in the correlation coefficient continues as t_{filter} increases up to about $t_{filter}\sim 43$ h where a local maximum of $r_{corr}=+0.923$ is reached. As t_{filter} increases beyond 43 h, the correlation coefficient decreases reaching a local minimum value of $r_{corr}=+0.889$ at $t_{filter}\sim 27$ days. This decrease in correlation is owed to the removal of correlated information with a timescale of 27 days (the rotation period of the Sun). Increasing the low-pass-filter timescale in the range 27 days to 1 year produces another region of increase in the correlation coefficient between AE_1 and $NL(\mathcal{G}+.\mathcal{B})$ with a local peak of $r_{corr}=+0.951$ at $t_{filter}=1$ year. This increase represents the removal of the periodic 1 year signal that is in the AE index but not in the solar wind: it is the removal of an uncorrelated signal and increases r_{corr}. A second local maximum at $t_{filter}=2$ years is probably also related to the removal of the 1 year periodic signal in AE.

[118] In Figure 15 (bottom) the linear correlation coefficient between the high-pass-filtered AE_1 time series and the high-pass-filtered $NL(\mathcal{G}+.\mathcal{B})$ driver function is plotted as a function of the high-pass-filter timescale t_{filter}. For example, at $t_{filter}=100$ h, the high-pass-filtered AE_1 time series is formed by creating a 100 h running average of $AE_1(t)$ and then subtracting that 100 h running average off the original unfiltered $AE_1(t)$ time series. Likewise for creating the high-pass-filtered $NL(\mathcal{G}+.\mathcal{B})$ time series. The first data point in Figure 15 (bottom) is the correlation coefficient between AE_1 and the $NL(\mathcal{G}+.\mathcal{B})$ driver at $t_{filter}=3$ h. This data point is the correlation coefficient for the high-frequency signals with timescale shorter than 3 h in the two time series, which is mostly uncorrelated noise ($r_{corr}=+0.321$). As t_{filter} increases from 3 h, more and more correlated signal in AE_1 and $NL(\mathcal{G}+.\mathcal{B})$ is added and the correlation coefficient r_{corr} between them increases. A broad maximum in the correlation coefficient is obtained for a high-pass-filter timescale $t_{filter}\sim 1100$ h where

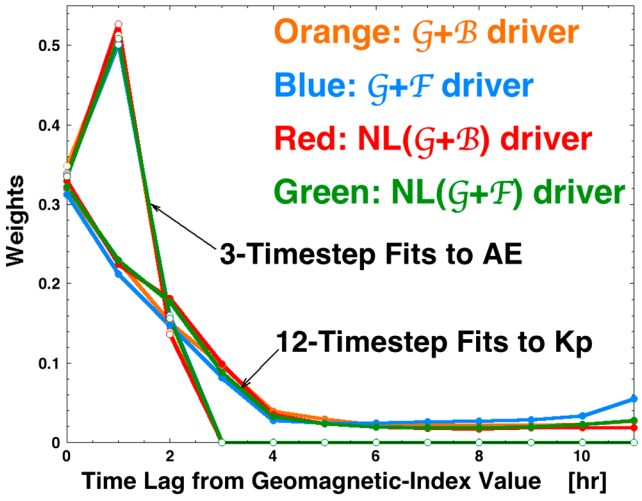

Figure 16. The weighting constants (cf. expression (68)) for multi-time step fits of the solar wind driver functions to the *AE* and the *Kp* indices. The hollow points are for three-time step fits to *AE* and the solid points are for 12-time step fits to *Kp*.

r_{corr} = +0.812. This maximum is probably owed to a combination of adding the highly correlated 27 day (648 h) timescales but not including the uncorrelated 1 year periodicity of *AE*.

[119] Much of the uncorrelated signal between the $\mathcal{G}+.\mathcal{B}$ driver and the *AE* index comes on timescales of a few hours, on timescales of 1 day (a periodicity in *AE* that is not in the solar wind), and on timescales of 1 year (a periodicity in *AE* that is not in the solar wind). Employing a wide band-pass filter on both the *AE* index and the $NL(\mathcal{G}+.\mathcal{B})$ driver function that removes variations with timescales of 1 day and shorter, and that removes variations with timescale of 1 year and longer resulted in an increase in the correlation coefficient between $NL(\mathcal{G}+.\mathcal{B})$ and *AE* to +0.916 from +0.812 for the unfiltered time series.

4.6. Multi-time Step Driver Functions

[120] For a time series of values at discrete times t_i, the correlation produced between the driver function $\mathcal{D}$ and the 1 h lagged *AE* index AE_1 is a correlation between $AE(t_i) \leftrightarrow \mathcal{D}(t_{i-1})$. Creating multi-time step solar wind driver functions improves the linear correlation between the driver and geomagnetic indices [cf. *Newell et al.*, 2007]. For example, correlation between the *AE* index and a three-time step driver would be written as

$$AE(t_i) \leftrightarrow c_0\mathcal{D}(t_i) + c_1\mathcal{D}(t_{i-1}) + c_2\mathcal{D}(t_{i-2}) \qquad (68)$$

where c_0, c_1, and c_2 are weighting constants (chosen such that $c_0 + c_1 + c_2 = 1$). To perform such multi-time step driver correlations, a computer code was written to optimally choose the weighting constants c_0, c_1,… by randomly varying the constants and only keeping the variation if it produced an increase in the correlation coefficient with the geomagnetic index time series. Driver functions with various numbers of time steps were explored. For $\mathcal{G}+.\mathcal{B}$ and $\mathcal{G}+.\mathcal{F}$ driver fits with *AE*, a three-time step fit was optimal; for $\mathcal{G}+.\mathcal{B}$ and $\mathcal{G}+.\mathcal{F}$ driver fits with *Kp*, a 12-time step fit was superior.

[121] In Figure 16 the values of the weighting constants are plotted for the fits between *AE* and *Kp* and the four driver functions $\mathcal{G}+.\mathcal{B}$, $\mathcal{G}+.\mathcal{F}$, $NL(\mathcal{G}+.\mathcal{B})$, and $NL(\mathcal{G}+.\mathcal{F})$. Note in Figure 16, for *AE* the code yielded multi-time step driver functions that were weighted heavily on the driver function value 1 h prior to the geomagnetic index value. For *Kp* the code yielded functions where the weighting is spread further back in time.

[122] In Table 4 the linear correlation coefficients between various multi-time step solar wind drivers and the *AE* and *Kp* indices are displayed. The years 1995–2011 were used (the Wind-ACE era) for better continuity of solar wind data. The first two columns of Table 4 pertain to correlations using only a single temporal value of the driver function for each temporal value of the geomagnetic index: The Pearson linear correlation coefficient r_{corr} and the fraction of the variance $1 - r_{corr}^2$ (in percent) of the index not described by the driver are displayed. The final three columns of Table 4 pertain to correlations using multiple time step values of the driver function for each value of the geomagnetic index: The third column displays the number of temporal values in the driver N_{times}, the fourth column displays the Pearson linear correlation coefficient r_{corr} between the driver and the geomagnetic index, and the fifth column displays the fraction of the variance $1 - r_{corr}^2$ (in percent) of the index not described by the driver. In every case, the multi-time step driver function substantially improves the correlation coefficient over the single-time step solar wind driver. The peak correlation with the *AE* index was found with $NL(\mathcal{G}+.\mathcal{B})$ driver using three time steps (as in expression (68)): A value r_{corr} = +0.847 was obtained, with 28.3% of the variance of *AE* unaccounted for. The peak correlation with the *Kp* index was found with $NL(\mathcal{G}+.\mathcal{F})$ driver (expression (66c)) using 12 time steps: A value r_{corr} = +0.871 was obtained, with 22.1% of the variance of *AE* unaccounted for.

4.7. Averaging the Driver Functions

[123] In section 4.6, multi-time step driver functions showed improved correlations between the driver functions and the geomagnetic indices. Using multi-time step driver functions is equivalent to using solar wind information at

Table 4. Improvement in the Linear Correlation Coefficient r_{corr}[a]

	Single Time Step		Multiple Time Step		
	r_{corr}	$1 - r_{corr}^2$	N_{times}	r_{corr}	$1 - r_{corr}^2$
Newell ↔ *AE*	0.782	38.8%	12	0.820	32.7%
Newell ↔ *Kp*	0.655	57.1%	12	0.754	43.1%
R_2 ↔ *AE*	0.773	40.2%	12	0.808	34.7%
R_2 ↔ *Kp*	0.706	50.2%	12	0.801	35.8%
$\mathcal{G}$ ↔ *AE*	0.760	42.2%	12	0.802	35.7%
$\mathcal{G}$ ↔ *Kp*	0.657	56.9%	12	0.762	41.9%
$\mathcal{G}+.\mathcal{B}$ ↔ *AE*	0.797	36.5%	3	0.829	31.3%
$\mathcal{G}+.\mathcal{B}$ ↔ *Kp*	0.782	38.8%	12	0.842	29.1%
$\mathcal{G}+.\mathcal{F}$ ↔ *AE*	0.782	38.8%	3	0.812	34.1%
$\mathcal{G}+.\mathcal{F}$ ↔ *Kp*	0.781	39.0%	12	0.844	28.8%
$NL(\mathcal{G}+.\mathcal{B})$ ↔ *AE*	0.815	33.5%	3	0.847	28.3%
$NL(\mathcal{G}+.\mathcal{B})$ ↔ *Kp*	0.793	37.1%	12	0.852	27.4%
$NL(\mathcal{G}+.\mathcal{F})$ ↔ *AE*	0.802	35.6%	3	0.833	30.6%
$NL(\mathcal{G}+.\mathcal{F})$ ↔ *Kp*	0.813	33.8%	12	0.871	24.1%

[a]Between the solar wind driver functions $\mathcal{G}+.\mathcal{B}$ and $\mathcal{G}+.\mathcal{F}$ and the geomagnetic indices *AE* and *Kp* when values of the driver from multiple time steps are used versus when the value at a single time step is used, for the years 1995–2011. The fraction $1 - r_{corr}^2$ of the variance of the indices that is not accounted for by variance of the driver is displayed in percent. For the multiple time step drivers, the number of time steps used N_{times} is also displayed.

Table 5. Pearson's Linear Correlation Coefficients r_{corr} Between Time-Averaged Driver Functions and Nonaveraged Geomagnetic Indices for the Years 1995–2011[a]

	1 Time Step	2 h Average	3 h Average	4 h Average	5 h Average
$AE_1 \leftrightarrow \mathscr{G}+.\mathscr{B}$	0.797	0.820	0.800	0.808	0.795
$AE_1 \leftrightarrow \mathscr{G}+.\mathscr{F}$	0.782	0.804	0.786	0.792	0.781
$AU_1 \leftrightarrow \mathscr{G}+.\mathscr{B}$	0.705	0.729	0.739	0.731	0.729
$AU_1 \leftrightarrow \mathscr{G}+.\mathscr{F}$	0.703	0.725	0.735	0.727	0.725
$-AL_1 \leftrightarrow \mathscr{G}+.\mathscr{B}$	0.763	0.783	0.777	0.766	0.749
$-AL_1 \leftrightarrow \mathscr{G}+.\mathscr{F}$	0.745	0.764	0.759	0.747	0.731
$\mathrm{PCI}_0 \leftrightarrow \mathscr{G}+.\mathscr{B}$	0.754	0.800	0.778	0.784	0.764
$\mathrm{PCI}_0 \leftrightarrow \mathscr{G}+.\mathscr{F}$	0.744	0.789	0.766	0.774	0.754
$Kp_1 \leftrightarrow \mathscr{G}+.\mathscr{B}$	0.782	0.814	0.830	0.840	0.843
$Kp_1 \leftrightarrow \mathscr{G}+.\mathscr{F}$	0.781	0.809	0.825	0.833	0.838
$-\mathrm{MBI}_1 \leftrightarrow \mathscr{G}+.\mathscr{B}$	0.780	0.821	0.834	0.835	0.844
$-\mathrm{MBI}_1 \leftrightarrow \mathscr{G}+.\mathscr{F}$	0.767	0.808	0.822	0.825	0.831
$-Dst^*_2 \leftrightarrow \mathscr{G}+.\mathscr{B}$	0.677	0.702	0.722	0.733	0.741
$-Dst^*_2 \leftrightarrow \mathscr{G}+.\mathscr{F}$	0.687	0.714	0.729	0.744	0.754

[a]The time averaging is performed with a running (boxcar) average. In this table the time lag between each geomagnetic index and the center time of the time averaging of the driver is preserved. All r_{corr} values are positive.

multiple time steps to describe the value of the geomagnetic index at a given time step, in a sense, adding information. Using multi-time step driver functions is also equivalent to averaging the driver function to remove high-frequency signal in the driver, in a sense, removing information. In this section, running averages of the driver functions are explored and cross-correlated with nonaveraged geomagnetic indices. The years 1995–2011 are used for their better continuity of solar wind data.

[124] In Table 5 the linear correlation coefficients r_{corr} between the $\mathscr{G}+.\mathscr{B}$ and $\mathscr{G}+.\mathscr{F}$ drivers and the seven geomagnetic indices are recorded for a one-time step value of the driver, a 2 h (two-point) running average of the driver, a 3 h running average, a 4 h running average, and a 5 h running average of the driver. The running averages are "boxcar" averages with equal weight on each time step. For example, a 5 h running average of the driver function $\mathscr{D}$ centered on time step t_i would be written as

$$[\mathscr{D}(t_{i+2}) + \mathscr{D}(t_{i+1}) + \mathscr{D}(t_i) + \mathscr{D}(t_{i-1}) + \mathscr{D}(t_{i-2})]/5 \qquad (69)$$

[125] No averaging is performed on the geomagnetic indices. In Table 5 the subscript "1" on *AE* means a 1 h lag between the time of *AE* and the center of the running average of the driver (accurate to within 0.5 h since the centers of the two-point and four-point running averages are at half time steps), the same for the subscripts on the other geomagnetic indices in Table 5. Comparing the r_{corr} values in columns 1 and 2, it is seen that a 2 h running average of the driver improves the correlation between both drivers and all seven indices. Looking at the r_{corr} values in each row of Table 5, it is found that for *AE*, *AL*, and PCI, a 2 h running average of the driver is optimal, for *AU*, a 3 h running average of the driver is optimal, and for *Kp*, MBI, and *Dst**, a 5 h or more running average of the driver is optimal. This indicates that indeed averaging away high-frequency signal in the driver functions improves the correlation with geomagnetic indices.

[126] In the cross correlations of Table 5 the time difference between the geomagnetic index and the center of the driver time average was preserved. Thus, information about the driver could be used from the past and from the future as seen from the time step of the geomagnetic index. In Table 6 correlation coefficients between the seven indices and time-averaged $\mathscr{G}+.\mathscr{B}$ and $\mathscr{G}+.\mathscr{F}$ driver functions are presented for time averaging that runs only into the past with respect to the geomagnetic index time step. For example, a 5 h running average of the driver, the geomagnetic index at time step t_i will be cross-correlated with a driver averaging that including time steps t_i, t_{i-1}, t_{i-2}, t_{i-4}, t_{i-5}. The exception is *Dst** where the averaging of the driver can be centered even further in the past: *Dst** prefers a large time lag and the preferred lag increases with the driver averaging.

[127] In Table 7 running averages that are confined to the past of the nonlinear versions $NL(\mathscr{G}+.\mathscr{B})$ and $NL(\mathscr{G}+.\mathscr{F})$ of the driver functions are cross-correlated with nonaveraged *AE* and *Kp* indices. Here it is again seen that the averaging of the driver function improves the correlation with the geomagnetic indices. This averaging is a removal of higher-frequency signal from the driver functions. For the *AE* index, 2 h or 3 h averaging of the nonlinear drivers is optimal. For the *Kp* index, 4 h averaging of the nonlinear drivers is found to be optimal.

[128] The running averages of $\mathscr{G}+.\mathscr{B}$ and $\mathscr{G}+.\mathscr{F}$ that are confined to the present and past (Tables 6 and 7) can be used as driver functions in the sense that a geomagnetic index can be predicted from solar wind measurements without requiring measurements from the future. As can be seen in Table 7, simple running averages of the $NL(\mathscr{G}+.\mathscr{B})$ and $NL(\mathscr{G}+.\mathscr{F})$ driver functions yield r_{corr} values of up to 0.832 with *AE* (for a 2 h running average of $NL(\mathscr{G}+.\mathscr{B})$) and up to 0.862 with *Kp* (for a 4 h running average of $NL(\mathscr{G}+.\mathscr{F})$).

4.8. Statistical Analysis of the Unpredicted Variance

[129] To obtain information about trends in the solar wind driver functions, the residuals (errors) between the indices I and the linear regression fits to the indices $m\mathscr{D}+b$ are examined. In this analysis the driver function is used to describe as much of the variance of the geomagnetic index as possible, and the measured value of the geomagnetic index is subtracted from that predicted variance and the residual variance of the index is analyzed. That "error" $\mathrm{E}=(m\mathscr{D}+b)-\mathrm{I}$ is a function of the time *t*. The correlation coefficients between E(*t*) and the various solar and solar wind parameters are collected into Table 8. The four columns of Table 8 are the correlations for (1) the difference between the prediction of the $\mathscr{G}+.\mathscr{B}$ driver and the 1 h lagged *AE* index, (2) the difference between the prediction of the $\mathscr{G}+.\mathscr{B}$ driver and the 1 h lagged *Kp* index, (3) the difference between the prediction of the $\mathscr{G}+.\mathscr{F}$ driver and the 1 h lagged *AE* index, and (4) the difference between the prediction of the $\mathscr{G}+.\mathscr{F}$ driver and the 1 h lagged *Kp* index. In calculating the correlation coefficients, there is typically about $N=190{,}000$ data points. Uncorrelated data would have correlation coefficients in the range of $\pm 2/N^{1/2}$ [e.g., *Beyer*, 1966; *Bendat and Piersol*, 1971], which is ±0.005. Correlation coefficients significantly larger in magnitude than 0.005 indicate a definite (but not necessarily strong) correlation or anticorrelation. Examining Table 8, very little in the sense of systematic patterns is seen. Looking at entries with correlation coefficients larger than 20% (greater than +0.20 or less than −0.20), all of the unpredicted variances of the *AE* and *Kp* indices show anticorrelations with u_{sw}, with $F_{10.7}$, and with $(1+Q)$. The solar wind driver functions tend to predict AE_1 and Kp_1 values

Table 6. Pearson's Linear Correlation Coefficients r_{corr} Between Time-Averaged Driver Functions and Nonaveraged Geomagnetic Indices for the Years 1995–2011[a]

	1 Time Step	2 h Average	3 h Average	4 h Average	5 h Average
$AE \leftrightarrow \mathscr{G}+.\mathscr{B}$	0.797	0.820	0.800	0.798	0.775
$AE \leftrightarrow \mathscr{G}+.\mathscr{F}$	0.782	0.804	0.786	0.803	0.762
$AU \leftrightarrow \mathscr{G}+.\mathscr{B}$	0.705	0.729	0.739	0.732	0.716
$AU \leftrightarrow \mathscr{G}+.\mathscr{F}$	0.703	0.725	0.735	0.728	0.714
$-AL \leftrightarrow \mathscr{G}+.\mathscr{B}$	0.763	0.783	0.777	0.751	0.727
$-AL \leftrightarrow \mathscr{G}+.\mathscr{F}$	0.745	0.764	0.759	0.734	0.710
PCI $\leftrightarrow \mathscr{G}+.\mathscr{B}$	0.754	0.800	0.787	0.764	0.736
PCI $\leftrightarrow \mathscr{G}+.\mathscr{F}$	0.744	0.789	0.777	0.756	0.729
$Kp \leftrightarrow \mathscr{G}+.\mathscr{B}$	0.782	0.814	0.830	0.833	0.828
$Kp \leftrightarrow \mathscr{G}+.\mathscr{F}$	0.781	0.809	0.825	0.829	0.825
$-$MBI $\leftrightarrow \mathscr{G}+.\mathscr{B}$	0.780	0.782	0.823	0.840	0.843
$-$MBI $\leftrightarrow \mathscr{G}+.\mathscr{F}$	0.767	0.766	0.807	0.825	0.831
$-Dst^* \leftrightarrow \mathscr{G}+.\mathscr{B}$	0.677	0.704	0.722	0.733	0.741
$-Dst^* \leftrightarrow \mathscr{G}+.\mathscr{F}$	0.687	0.714	0.731	0.744	0.754

[a]The time averaging is performed with a running (boxcar) average. In this table the time averaging is restricted to time values of the solar wind that are in the present or past relative to the time value of the geomagnetic index. All r_{corr} values are positive.

that are too low at higher values of u_{sw}, at higher values of $F_{10.7}$, and at higher values of $(1+Q)$; likewise the drivers tend to overpredict the indices when u_{sw}, $F_{10.7}$, and $(1+Q)$ are low. Hence, if the driver functions were (a) increased in strength slightly with increasing solar wind speed u_{sw}, (b) increased in strength slightly with increasing $F_{10.7}$, and (c) increased in strength slightly with $(1+Q)$, they would do better jobs at predicting the *AE* and *Kp* indices. The *Kp* residual from the $\mathscr{G}+.\mathscr{B}$ driver (second column) shows anticorrelations with $|B_{sw}|$ and δB_{vec} and positive correlation with M_A of the solar wind: The other three columns do not show significant correlation or anticorrelation with δB_{vec} or M_A.

[130] Table 9 looks at the cross correlations between the four sets of residuals (unpredicted variances) between the two solar wind drivers $\mathscr{G}+.\mathscr{B}$ and $\mathscr{G}+.\mathscr{F}$ and the two indices AE_1 and Kp_1 and finds that the residuals are not independent of each other. The correlations between the *AE* residuals from the $\mathscr{G}+.\mathscr{B}$ and the $\mathscr{G}+.\mathscr{F}$ drivers are extremely strong (+0.965) and the correlations between the *Kp* residuals from the $\mathscr{G}+.\mathscr{B}$ and the $\mathscr{G}+.\mathscr{F}$ drivers are also very strong (+0.877). The correlations between the *Kp* residuals and the *AE* residuals are quite significant (+0.510 and +0.465) but not as strong. The strong correlations between the residuals of $AE_1 \leftrightarrow \mathscr{G}+.\mathscr{B}$ and the residuals of $AE_1 \leftrightarrow \mathscr{G}+.\mathscr{F}$ indicate that the $\mathscr{G}+.\mathscr{B}$ and $\mathscr{G}+.\mathscr{F}$ drivers have very similar temporal behavior. (Likewise for the residuals of $Kp_1 \leftrightarrow \mathscr{G}+.\mathscr{B}$ and the residuals of $Kp_1 \leftrightarrow \mathscr{G}+.\mathscr{F}$). Indeed, the linear correlation coefficients between the $\mathscr{G}+.\mathscr{B}$ and $\mathscr{G}+.\mathscr{F}$ drivers for AE_1 and for Kp_1 are +0.979 and +0.921, respectively. On the contrary, the linear correlation coefficient between AE_1 and Kp_1 is +0.774.

Table 7. Linear Correlation Coefficients r_{corr} Between the Two Time-Averaged Nonlinear Driver Functions $NL(\mathscr{G}+.\mathscr{B})$ and $NL(\mathscr{G}+.\mathscr{F})$ and Nonaveraged Geomagnetic Indices *AL* and *Kp* for the Years 1995–2011[a]

	1 Time Step	2 h Average	3 h Average	4 h Average	5 h Average
$AE \leftrightarrow NL(\mathscr{G}+.\mathscr{B})$	0.815	0.838	0.837	0.813	0.790
$AE \leftrightarrow NL(\mathscr{G}+.\mathscr{F})$	0.802	0.824	0.824	0.801	0.779
$Kp \leftrightarrow NL(\mathscr{G}+.\mathscr{B})$	0.793	0.825	0.842	0.844	0.839
$Kp \leftrightarrow NL(\mathscr{G}+.\mathscr{F})$	0.813	0.844	0.860	0.862	0.857

[a]The time averaging is performed with a running (boxcar) average. In this table the time averaging is restricted to time values of the solar wind that are in the present or past relative to the time value of the geomagnetic index. All r_{corr} values are positive.

4.9. Detrending the Indices

[131] Analysis of residual errors will bring out the annual and diurnal trends that are in the indices but not in the solar wind. Detrending the indices by subtracting off those annual and diurnal trends will result in improved correlation coefficients between the solar wind drivers and the indices.

[132] As seen in Figures 10 and 11, there are strong annual and semiannual trends in the residual error between the solar wind driver functions and the indices. The amplitudes of these trends can be seen in Figure 17 for *AE* (top) and for *Kp* (bottom). In the figure, fits to the indices from the $NL(\mathscr{G}+.\mathscr{B})$ (blue) and $NL(\mathscr{G}+.\mathscr{F})$ (red) driver functions are subtracted off the measured values of the indices and 4000-point running averages are plotted as functions of the day of year. The annual trend in *AE* is clearly seen in Figure 17 (top) [see also *Allen and Kroehl*, 1975, Figures 9 and 10; *Ahn et al.*, 2000, Figure 4], with the smooth green curve being the fit to the data, given by

$$AE_{annual} = T_1 + T_2 + T_3 \tag{70}$$

where

$$T_1 = 13.1 \tag{71a}$$

$$T_2 = -49.0\ \cos^8((\text{day} - 3.7)\pi/365) \tag{71b}$$

$$T_3 = 10.2\cos((\text{day} - 163.6)2\pi/365) \tag{71c}$$

where "day" is the day of year. The annual variation of *AE* is dominated by the second term T_2 (expression (71b), which corresponds to an anomalously low *AE* during the winter season. Figure 17 (bottom) clearly shows a semiannual variation

Table 8. Linear Correlation Coefficients r_{corr} Between the Residuals (Errors) of the Two Solar Wind Driver Functions $\mathscr{G}+.\mathscr{B}$ and $\mathscr{G}+.\mathscr{F}$ and Their Target Geomagnetic Indices AE_1 and Kp_1

	Errors			
	$(\mathscr{G}+.\mathscr{B})_{fit} - AE_1$	$(\mathscr{G}+.\mathscr{B})_{fit} - Kp_1$	$(\mathscr{G}+.\mathscr{F})_{fit} - AE_1$	$(\mathscr{G}+.\mathscr{F})_{fit} - Kp_1$
u_{sw}	−0.094	−0.177	−0.206	−0.312
n_{sw}	+0.045	+0.017	+0.058	+0.065
T_p	−0.057	−0.168	−0.086	−0.138
$\lvert B_{sw}\rvert$	−0.081	−0.350	+0.024	−0.010
M_A	+0.069	+0.276	+0.069	+0.041
B_z	+0.066	−0.122	+0.098	−0.020
θ_{clock}	+0.084	+0.188	+0.047	+0.084
θ_{Bn}	−0.110	−0.061	−0.087	−0.025
P_{ram}	+0.035	+0.059	+0.002	+0.005
δB_m	−0.002	−0.003	+0.040	+0.033
δB_{vec}	−0.050	−0.283	+0.052	+0.016
$F_{10.7}$	−0.180	−0.271	−0.118	−0.181
$1+Q$	−0.178	−0.355	−0.103	−0.213

Table 9. Linear Correlation Coefficients Between the Various Sets of Residuals (Errors) Between the AE_1 and Kp_1 Indices and the Solar Wind Drivers $\mathcal{G}+\mathcal{B}$ and $\mathcal{G}+\mathcal{F}$

	Errors			
	$(\mathcal{G}+\mathcal{B})_{\rm fit}-AE_1$	$(\mathcal{G}+\mathcal{B})_{\rm fit}-Kp_1$	$(\mathcal{G}+\mathcal{F})_{\rm fit}-AE_1$	$(\mathcal{G}+\mathcal{F})_{\rm fit}-Kp_1$
Errors $(\mathcal{G}+\mathcal{B})_{\rm fit}-AE_1$	+1.000	+0.465	+0.965	+0.456
Errors $(\mathcal{G}+\mathcal{B})_{\rm fit}-Kp_1$	+0.465	+1.000	+0.395	+0.877
Errors $(\mathcal{G}+\mathcal{F})_{\rm fit}-AE_1$	+0.965	+0.395	+1.000	+0.510
Errors $(\mathcal{G}+\mathcal{F})_{\rm fit}-Kp_1$	+0.456	+0.877	+0.510	+1.000

of the residual *Kp* index [cf. *McIntosh*, 1959; *Murayama*, 1974]. The smooth green curve in Figure 17 (bottom) is a cosine fit to the data points:

$$Kp_{\rm semiannual} = -0.135\cos((\text{day}+5.4)4\pi/365) \qquad (72)$$

where again "day" is the day of year. This residual of *Kp* is high during the spring and fall seasons and low during the winter and summer. The cause of this $Kp_{\rm semiannual}$ variation might be unaccounted for physics in the solar wind driver functions and the Russell-McPherron effect; however, the Russell-McPherron effect has a diurnal pattern that varies from season to season [cf. *Russell and McPherron*, 1973, Figure 5; *Cliver et al.*, 2000, Figure 2] and, as will be seen the paragraphs below, the diurnal pattern of the *Kp* residual is the same in all four seasons. *Cliver et al.* [2000] argue that there is a semiannual variation of geomagnetic activity beyond the Russell-McPherron effect caused by the sunward-antisunward tilt of the Earth's dipole; however, again, this dipole tilt effect predicts a diurnal variation that varies with season [cf. *Cliver et al.*, 2000, Figure 1] whereas the diurnal variation of the *Kp* residual does not vary with season.

[133] The combined annual and diurnal residual errors for the *AE* index are explored in Figure 18. Here fits to the AE_1 index from the $NL(\mathcal{G}+\mathcal{B})$ and $NL(\mathcal{G}+\mathcal{F})$ driver functions are subtracted off the measured value of the *AE* index. The hourly points are separated into four seasons and then plotted as a function of universal time, where a random number between 0.0 and 1.0 is added to the hourly value of UT to spread the points. The 1001-point running averages are plotted in Figure 18. The seasons are spring (green: days 35–126), summer (blue: days 126–217), fall (red: days 217–310), and winter (black: days 310–35). As can be seen, there are strong diurnal trends to *AE* that vary from season to season, with the diurnal trend reversing from summer to winter: in summer *AE* peaks at ~5 UT and in winter *AE* peaks at ~15 UT. There are also seasonally varying offsets to the level of *AE*, with the offset value negative in winter and positive in summer. The diurnal pattern of the *AE* residual from season to season looks similar to the *AE* variation in Plate 4 of *Cliver et al.* [2000], except for the seasonal variation of the offsets. Cliver et al. attribute this *AE* variation to sunward-antisunward dipole tilt effects on the dayside reconnection rate: *Lyatsky et al.* [2001] attribute the *AE* pattern to solar illumination effects on both polar caps. The asymmetry in the annual variation of *AE* with the sharp deep minimum in winter (cf. Figure 17 (top) and expression (71b)) may indicate that illumination of the northern polar cap where the *AE* stations are located may control the diurnal and annual patterns of the *AE* residual. The four smooth curves in Figure 18 are cosine fits to the data for the four seasons. All of the points in Figure 18 can be approximately

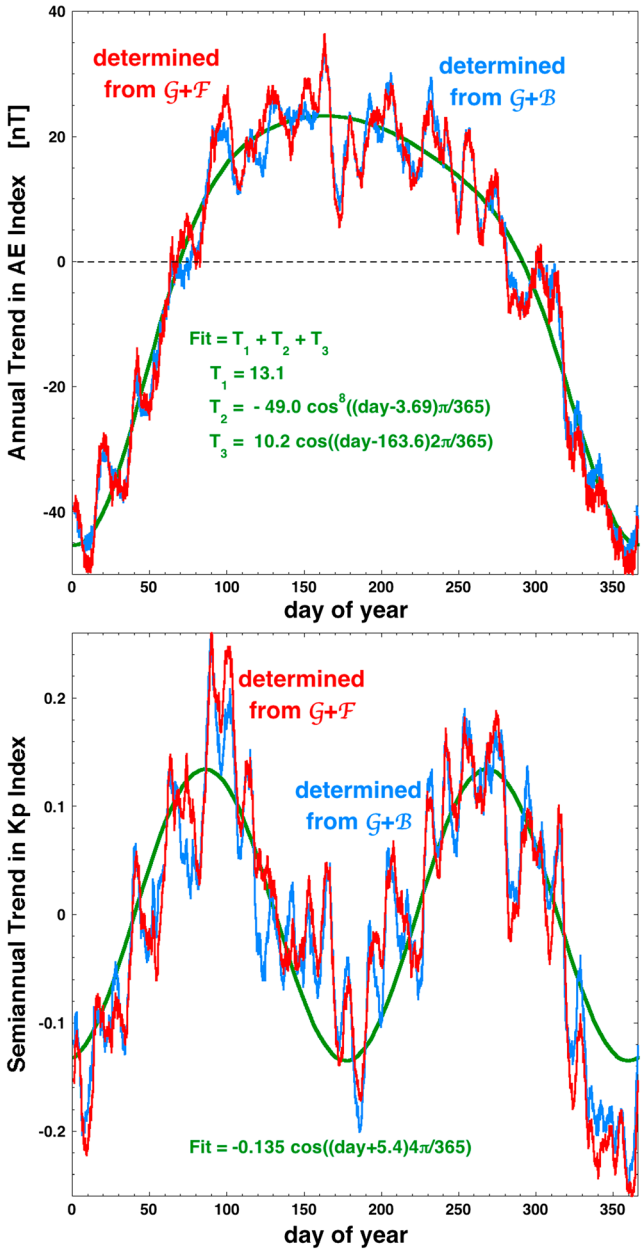

Figure 17. (top) The annual trend in the residual error for *AE* and (bottom) the semiannual trend in the residual error for *Kp* are shown. The blue and red points are 2000-point running averages in day-of-year minus the residual error for the nonlinear $\mathcal{G}+\mathcal{B}$ and nonlinear $\mathcal{G}+\mathcal{F}$ drivers, respectively. The green curves are fits to the data. Data from the years 1980–2011 are used.

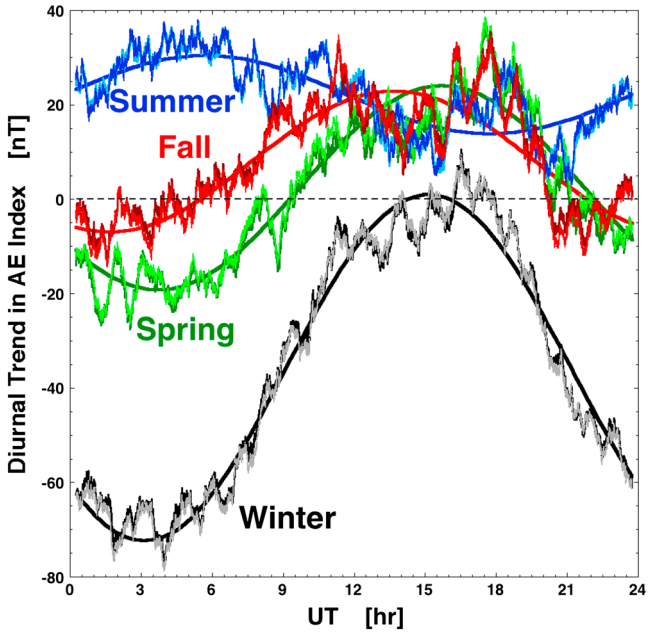

Figure 18. The diurnal trend in minus the residual error for *AE* is shown separating the 1980–2011 data into the four seasons of the year. The two shades of colors are for the nonlinear $\mathscr{G}+.\mathscr{B}$ and nonlinear $\mathscr{G}+.\mathscr{F}$ drivers. The data points plotted are 1000-point running averages in UT. The smooth curves are fits to the data.

fit by the AE_{trend} function that describes and annual and diurnal trends:

$$AE_{\text{trend}} = c_1 + c_2 \cos((\text{UT} - 3.6)2\pi/24) \tag{73}$$

where

$$c_1 = 0.530 + 28.8 \cos((\text{day} + 3.76)2\pi/365) \tag{74a}$$

$$c_2 = 15.8 + 22.5 \cos((\text{day} + 1.79)2\pi/365) \tag{74b}$$

where UT is the universal time in hours and day is the day of the year.

[134] The diurnal residual error for the *Kp* index is explored in Figure 19. Here fits to the Kp_1 index from the $NL(\mathscr{G}+.\mathscr{B})$ (blue) and $NL(\mathscr{G}+.\mathscr{F})$ (red) drivers are subtracted off the measured value of the *Kp* index. Random numbers between 0.0 and 1.0 are added to the hourly value of UT to spread the points and 1001-point running averages are plotted. In Figure 19 (top) the data are separated by season: spring (green), summer (blue), fall (red), and winter (black). As can be seen in Figure 19 (top), there are strong diurnal trends to *Kp* that are similar in every season. In Figure 19 (middle) trigonometric fits to the data in the top panel are plotted, with one fit for each season. Except for the semiannual offsets, the fits have similar shape from one season to the next. (This is very different from the *AE* residuals (cf. Figure 18) where the diurnal variations change from season to season.) In each season, *Kp* is anomalously low in the 3–12 UT band. In Figure 19 (bottom) the *Kp* residual data for all four seasons are plotted together, with a 400-point running average in UT. The blue points are the *Kp* residual for the $NL(\mathscr{G}+.\mathscr{B})$ driver and the red points are the *Kp* residual for the $NL(\mathscr{G}+.\mathscr{F})$ driver. The smooth green curve in the bottom panel is a UT trigonometric fit to all of the data. The fit has three terms:

$$Kp_{\text{diurnal}} = T_1 + T_2 + T_3 \tag{75}$$

where

$$T_1 = 0.051 \tag{76a}$$

$$T_2 = -0.191 \cos^8((\text{UT} - 8.9)\pi/24) \tag{76b}$$

$$T_3 = -0.0519 \cos((\text{UT} - 13.6)2\pi/24) \tag{76c}$$

[135] Detrending the *AE* and *Kp* indices by subtracting off AE_{trend}(UT,day) and Kp_{diurnal}(UT) given by expressions (73) and (75) improves the correlation coefficients r_{corr} between solar wind drivers and the *AE* and *Kp* indices. This is demonstrated in Tables 10 (for *AE*) and 11 (for *Kp*) where the correlation coefficients for the indices *AE* and *Kp* are compared with the correlation coefficients for the detrended indices $AE - AE_{\text{trend}}$ and $Kp - Kp_{\text{trend}}$. In Table 10 the correlation coefficients r_{corr} for *AE* all increase by a factor of from 0.77% to 1.18% when the *AE* index is detrended for the diurnal and annual variations; in Table 11 the correlation coefficients r_{corr} for *Kp* all increase by a factor of from 0.14% to 0.19% when the *Kp* index is detrended for the diurnal variation.

[136] One could also detrend *Kp* for its semiannual variation to further improve the correlation coefficients, but some of that semiannual variation could be caused by unaccounted for physics in the solar wind driver. The final column of Table 11 displays the coefficients for *Kp* detrended of both the diurnal variation Kp_{diurnal} (expression (75)) and the semiannual variation $Kp_{\text{semiannual}}$ (expression (72)). Detrending for both increases all of the correlation coefficients by a factor of from 0.27% to 0.43%.

5. Simplified Versions of the Driver Functions for Practical Use

[137] The two solar wind driver functions $\mathscr{G}+.\mathscr{B}$ and $\mathscr{G}+.\mathscr{F}$ (using expression (23) for $\mathscr{G}$) are mathematically complicated due to the complicated nature of the term $f(M_A, M_{ms}, \theta_{\text{clock}}, \theta_{Bn})$ (expression (7) and definitions given by expressions (4a)–(4k)) in the dayside reconnection rate expression. The term $f(M_A, M_{ms}, \theta_{\text{clock}}, \theta_{Bn})$ contains information about the modification of the solar wind plasma by the bow shock and by the magnetosheath flow pattern.

[138] In *Borovsky* [2013] a greatly simplified approximation of the derived dayside reconnection rate R_2 was obtained by functionally fitting the Alfven Mach number dependence of R_2 and by ignoring the twist of the X line orientation away from the $\theta_{\text{clock}}/2$ position. That resulted in the approximation [cf. *Borovsky*, 2013, equation (34)]

$$R_{2\text{app}} = 1.68 \times 10^{-2} \sin^2(\theta_{\text{clock}}/2) n_{sw}{}^{1/2} u_{sw}{}^2 M_A{}^{-0.3044} \exp\left(-[M_A/3.18]^{1/2}\right) \tag{77}$$

where all the definitions in expressions (4a)–(4k) are unnecessary. An approximated version of the reconnection-coupled generator $\mathscr{G}$ is obtained by multiplying expression (77) by

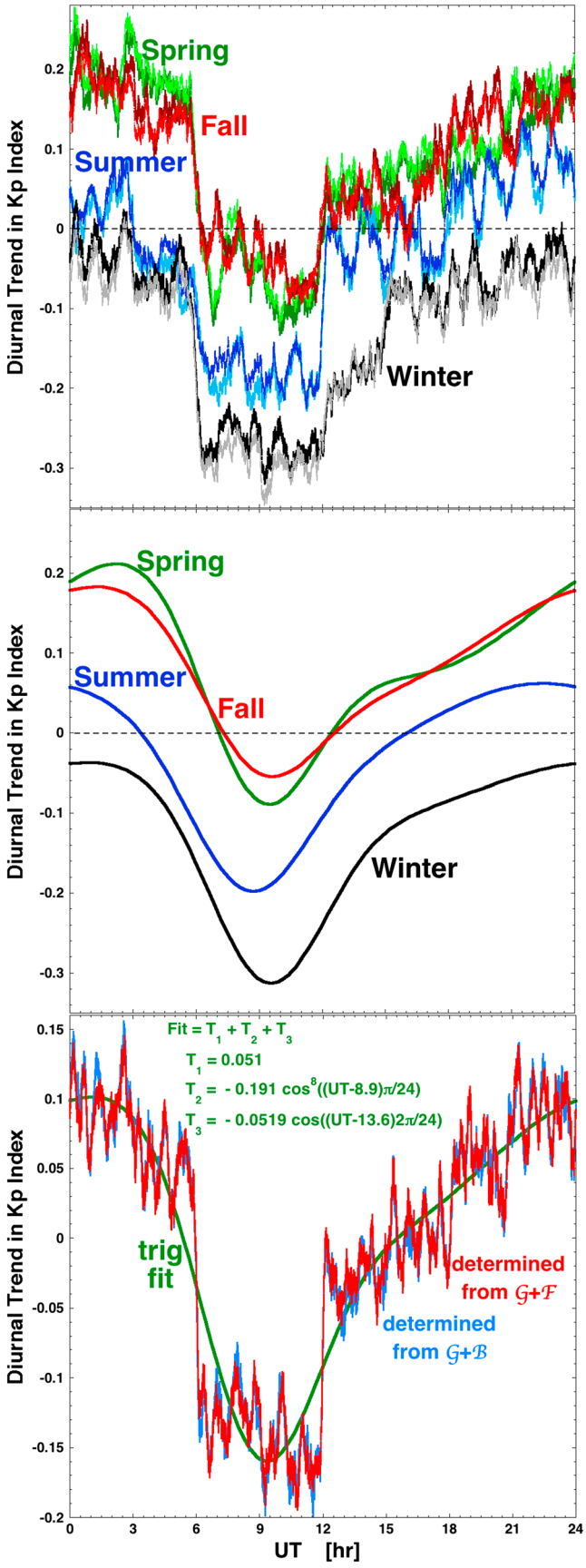

Figure 19. (top) The diurnal trend in the residual error for *Kp* is shown separating the 1980–2011 data into the four seasons of the year and running 1000-point running averages in UT; the two shades of colors are for the nonlinear $\mathcal{G}+.\mathcal{B}$ and nonlinear $\mathcal{G}+.\mathcal{F}$ drivers. (middle) Trigonometric fits to the data in the top panel are plotted. (bottom) The 1980–2011 data are plotted without separation into seasons and 4000-point running averages are applied. The green curve in the bottom panel is a trigonometric fit to the data. In all panels, minus the residual error is plotted.

expression (15) for the length of the dayside X line and by $(1+Q)^{-1}$ for the generator current saturation: dropping the constants, this results in

$$G_{app} = \sin^2(\theta_{clock}/2) n_{sw}^{1/3} u_{sw}^{5/3} M_A^{-0.7084} \exp\left(-[M_A/3.18]^{1/2}\right)(1+Q)^{-1} \quad (78)$$

where $Q = Q(n_{sw}, B_{sw}, F_{10.7})$ is given by expression (22). Correlation coefficients between $\mathcal{G}_{app}$ and the seven geomagnetic indices appear in Table 1, where the performance of $\mathcal{G}_{app}$ can be compared with the performance of $\mathcal{G}$. As can be seen $\mathcal{G}_{app}$ is slightly inferior to the full expression for $\mathcal{G}$.

[139] The simplified versions of the $\mathcal{G}+.\mathcal{B}$ and $\mathcal{G}+.\mathcal{F}$ driver functions are attained by adding the Bohm and freestream viscous drivers to expression (78), with an arbitrary constant a_{Bohm} or a_{free} (see Table 12). Writing the simplified version of the Bohm-viscosity $\mathcal{G}+.\mathcal{B}$ driver as $\mathcal{D}_{\mathcal{G}+.\mathcal{B}} = \mathcal{G}_{app} + a_{Bohm}.\mathcal{B}$ and using expressions (78) for $\mathcal{G}_{app}$ and 39 for $.\mathcal{B}$, this is

$$\mathcal{D}_{\mathcal{G}+.\mathcal{B}} = \sin^2(\theta_{clock}/2) n_{sw}^{1/3} u_{sw}^{5/3} M_A^{-0.7084} \exp\left(-[M_A/3.18]^{1/2}\right)(1+Q)^{-1} + a_{Bohm} n_{sw}^{1/2} u_{sw}^{5/2} C^{-1/2} W^{1/2} \quad (79)$$

where $C = \{2.44 \times 10^{-4} + [1 + 1.38 \log_e(M_A)]^{-6}\}^{-1/6}$ and where W is given by expression (33). Writing the simplified version of the freestream-turbulence $\mathcal{G}+.\mathcal{F}$ driver as $\mathcal{D}_{\mathcal{G}+.\mathcal{F}} = \mathcal{G}_{app} + a_{free}.\mathcal{F}$ and using expressions (78) for $\mathcal{G}_{app}$ and (63) for $.\mathcal{F}$, this is

$$\mathcal{D}_{\mathcal{G}+.\mathcal{B}} = \sin^2(\theta_{clock}/2) n_{sw}^{1/3} u_{sw}^{5/3} M_A^{-0.7084} \exp\left(-[M_A/3.18]^{1/2}\right)(1+Q)^{-1} + a_{free} n_{sw}^{1/2} u_{sw}^{11/6} \delta B_m^{1/2} C^{-1} G \quad (80)$$

with G given by expression (61). (From an examination of the similarity of the functional forms of the first and second terms in both expressions (79) and (80), one can see the proxy effect wherein the viscous driver (second term) also describes reconnection and wherein the reconnection driver (first term) also describes the viscous interaction.).

[140] In Table 12 the values of the constants a_{Bohm} and a_{free} in expressions (79) and (80) are given for use with each of the seven geomagnetic indices. Table 12 also contains the linear correlation coefficients between the simplified solar wind drivers $\mathcal{D}_{\mathcal{G}+.\mathcal{B}}$ and $\mathcal{D}_{\mathcal{G}+.\mathcal{F}}$ and the seven geomagnetic indices. Comparing the correlation coefficients of Table 12

Table 10. Linear Correlation Coefficients r_{corr} Between Various Driver Functions and the *AE* Index[a]

	r_{corr} for *AE*	r_{corr} for $AE - AE_{trend}$
$R_1 \leftrightarrow AE_1$	0.750	0.757
Newell $\leftrightarrow AE_1$	0.780	0.787
$R_2 \leftrightarrow AE_1$	0.774	0.781
$\mathscr{G} \leftrightarrow AE_1$	0.757	0.765
$\mathscr{B} \leftrightarrow AE_1$	0.372	0.375
$\mathscr{T} \leftrightarrow AE_1$	0.443	0.448
$\mathscr{G}+.\mathscr{B} \leftrightarrow AE_1$	0.797	0.804
$\mathscr{G}+.\mathscr{T} \leftrightarrow AE_1$	0.782	0.790
$NL(\mathscr{G}+.\mathscr{B}) \leftrightarrow AE_1$	0.812	0.820
$NL(\mathscr{G}+.\mathscr{T}) \leftrightarrow AE_1$	0.799	0.807
2 h ave $NL(\mathscr{G}+.\mathscr{B}) \leftrightarrow AE_0$	0.837	0.845
2 h ave $NL(\mathscr{G}+.\mathscr{T}) \leftrightarrow AE_0$	0.823	0.831
3-point $NL(\mathscr{G}+.\mathscr{B}) \leftrightarrow AE_0$	0.847	0.855
3-point $NL(\mathscr{G}+.\mathscr{T}) \leftrightarrow AE_0$	0.833	0.841

[a]In the first column the *AE* index is not detrended and in the second column the *AE* index is detrended for diurnal and annual variations. The data are from the years 1980–2011.

for $\mathscr{D}_{\mathscr{G}+.\mathscr{B}}$ and $\mathscr{D}_{\mathscr{G}+.\mathscr{T}}$ with the correlation coefficients for $\mathscr{G}+.\mathscr{B}$ and $\mathscr{G}+.\mathscr{T}$ in Table 1, one can see that the $\mathscr{D}_{\mathscr{G}+.\mathscr{B}}$ approximation to $\mathscr{G}+.\mathscr{B}$ actually performs slightly better than $\mathscr{G}+.\mathscr{B}$ and that the $\mathscr{D}_{\mathscr{G}+.\mathscr{T}}$ approximation to $\mathscr{G}+.\mathscr{T}$ performs slightly worse than $\mathscr{G}+.\mathscr{T}$ does. The simplified expressions (79) and (80) are much easier to implement than are the full expressions for $\mathscr{G}+.\mathscr{B}$ and $\mathscr{G}+.\mathscr{T}$.

6. Drawbacks, Complications, and Unknowns

[141] In this report, derived driver functions for solar wind/magnetosphere coupling were developed and tested for their ability to account for the behavior of seven geomagnetic indices. Linear correlation coefficients r_{corr} between the two solar wind drivers $\mathscr{G}+.\mathscr{B}$ and $\mathscr{G}+.\mathscr{T}$ and the indices at less than the 80% level were obtained (cf. Table 1). Nonlinear versions of the two driver functions were given and the correlation coefficients between the *AE* and *Kp* indices and those nonlinear drivers surpassed 80% (cf. Table 3). Multi-time step versions of the nonlinear solar wind drivers brought the linear correlation coefficients with the *AE* and *Kp* indices up to the 85% level (cf. Table 4). Detrending the indices for diurnal and annual variations produced further improvements.

[142] More sophistication in the mathematical connection of the solar wind driver functions to the geomagnetic indices may provide improved correlation coefficients. There are multiple time lags [cf. *Smith et al*., 1999; *Fung and Shao*, 2008] and almost certainly variable time lags [cf. *Rucker and Trattner*, 1991] between the solar wind and the magnetosphere-ionosphere system that could be explicitly accounted for in future versions of the solar wind driver functions. Utilizing solar wind measurements and geomagnetic indices at higher time resolution (minutes) instead of hourly averages should also shed new light on the abilities of the driver functions and on the physics of solar wind/magnetosphere coupling.

6.1. What Physics Is Missing?

[143] We know that there are missing physical processes in the picture of solar wind/magnetosphere coupling derived in this report. Seven examples follow:

[144] 1. The mass density of the dayside magnetosphere has been set to 0 in all of the coupling calculations in this report. However, it is known that during geomagnetically active times, the mass density of the dayside magnetosphere can be comparable to that of the magnetosheath inside of plasmaspheric drainage plumes [*Borovsky and Denton*, 2008] and across the dayside [*Takahashi et al*., 2010]. Estimates of the storm time reduction of solar wind/magnetosphere coupling by magnetospheric mass (by the plasmaspheric drainage plume, by O^+ in the ion plasma sheet, and by the warm plasma cloak) are tens of percent [*Borovsky et al*., 2013]. A parameterization of the magnetospheric mass density in terms of upstream solar wind parameters and solar parameters (although probably with a long time lag) could be used to improve the capability of the existing reconnection-coupled MHD generator portion of the physical driver functions.

[145] 2. Kelvin-Helmholtz-facilitated reconnection [*Nykyri and Otto*, 2001; *Nakamura et al*., 2006; *Chen et al*., 1997; *Zhang et al*., 2011] is not included in the present derivation of solar wind/magnetosphere coupling functions. In the calculation of the effective length of the dayside reconnection X line in section 2.2, it was argued that reconnection is hindered when the flow shear of the magnetosheath along the magnetopause becomes too large. However, at those locations of large flow shear, Kelvin-Helmholtz rollup of the magnetopause may actually increase reconnection.

[146] 3. Behind-the-cusp reconnection between the lobe magnetic field and the solar wind [*Gosling et al*., 1991; *Song et al*., 1999] is not included in our derivation of solar wind/magnetosphere coupling functions. Predominantly, under northward IMF, connection of the solar wind MHD generator to the Earth via high-latitude reconnection can occur, competing with the viscous interaction when the magnetosphere is in a quiet state.

[147] 4. The modulation of the viscous interaction between the magnetosheath flow and the magnetosphere by the presence or absence of momentum transfer in Kelvin-Helmholtz processes [e.g., *Miura*, 1984; *Farrugia and Gratton*, 2011] has not been included in the present derivation of solar wind/

Table 11. Linear Correlation Coefficients r_{corr} Between Various Driver Functions and the *Kp* Index[a]

	r_{corr} for *Kp*	r_{corr} for $Kp - Kp_{diurnal}$	r_{corr} for $Kp - Kp_{diurnal} - Kp_{semi}$
$R_1 \leftrightarrow Kp_1$	0.774	0.748	0.750
Newell $\leftrightarrow Kp_1$	0.653	0.653	0.655
$R_2 \leftrightarrow Kp_1$	0.704	0.706	0.707
$\mathscr{G} \leftrightarrow Kp_1$	0.648	0.649	0.650
$\mathscr{B} \leftrightarrow Kp_1$	0.531	0.532	0.533
$\mathscr{T} \leftrightarrow Kp_1$	0.632	0.633	0.634
$\mathscr{G}+.\mathscr{B} \leftrightarrow Kp_1$	0.778	0.779	0.780
$\mathscr{G}+.\mathscr{T} \leftrightarrow Kp_1$	0.781	0.783	0.784
$NL(\mathscr{G}+.\mathscr{B}) \leftrightarrow Kp_1$	0.789	0.790	0.791
$NL(\mathscr{G}+.\mathscr{T}) \leftrightarrow Kp_1$	0.812	0.813	0.815
2 h ave $NL(\mathscr{G}+.\mathscr{B}) \leftrightarrow Kp_0$	0.821	0.823	0.824
2 h ave $NL(\mathscr{G}+.\mathscr{T}) \leftrightarrow Kp_0$	0.843	0.845	0.846
12-point $NL(\mathscr{G}+.\mathscr{B}) \leftrightarrow Kp_0$	0.852	0.853	0.854
12-point $NL(\mathscr{G}+.\mathscr{T}) \leftrightarrow Kp_0$	0.871	0.872	0.874

[a]In the first column the *Kp* index is not detrended, in the second column *Kp* is detrended for its diurnal variation, and in the third column the *Kp* index is detrended for diurnal and semiannual variations. The data are from the years 1980–2011.

Table 12. Linear Correlation Coefficients r_{corr} Between the Two Simplified Solar Wind Drivers $\mathscr{D}_{\mathscr{G}+\mathscr{B}}$ and $\mathscr{D}_{\mathscr{G}+\mathscr{F}}$ and Seven Geomagnetic Indices[a]

	$\mathscr{D}_{\mathscr{G}+\mathscr{B}} = \mathscr{G}_{app} + a_{Bohm}\mathscr{B}$		$\mathscr{D}_{\mathscr{G}+\mathscr{F}} = \mathscr{G}_{app} + a_{free}\mathscr{F}$	
	a_{Bohm}	r_{corr}	a_{free}	r_{corr}
AE 1 h lagged	8.60×10^{-5}	0.797	1.00×10^{-3}	0.775
AU 1 h lagged	9.25×10^{-5}	0.699	1.39×10^{-3}	0.693
$-AL$ 1 h lagged	8.35×10^{-5}	0.764	8.35×10^{-4}	0.738
PCI	8.25×10^{-5}	0.756	1.01×10^{-3}	0.740
Kp 1 h lagged	1.72×10^{-4}	0.783	2.99×10^{-3}	0.779
−MBI 1 h lagged	1.16×10^{-4}	0.782	1.58×10^{-3}	0.759
$-Dst^*$ 2 h lagged	1.71×10^{-4}	0.695	2.92×10^{-3}	0.691
7-index sum		5.276		5.175

[a]The values of the constants a_{Bohm} and a_{free} in the expressions for $\mathscr{D}_{\mathscr{G}+\mathscr{B}}$ and $\mathscr{D}_{\mathscr{G}+\mathscr{F}}$ are also given for each geomagnetic index.

magnetosphere coupling functions. The conditions for Kelvin-Helmholtz-mediated reconnection could involve critical turn-on criteria expressed as functions of solar wind parameters.

[148] 5. Tilted X line effects, such as a different scaling of the reconnection X line length as the IMF clock angle varies or the draping of field lines making the actual reconnection clock angle differ from the IMF clock angle, have not been mathematically included in the present derivation of solar wind/magnetosphere coupling functions.

[149] 6. Mass transfer from the solar wind into the magnetosphere [*Borovsky et al.*, 1998; *Denton and Borovsky*, 2009] has not been factored into the present picture of the coupling. Evidence for the density of the solar wind affecting the response of the Earth during storms has been found [cf. *Smith et al.*, 1999; *Lavraud et al.*, 2006; *Singh and Badruddin*, 2012]. Solar plasma leaking into the magnetosphere from a high-density solar wind produces stronger-than-normal diamagnetic currents [*Borovsky and Denton*, 2010a] that can register in *Dst** and that may produce stronger-than-normal magnetotail activity. Such mass-coupling effects (probably with time lags of hours) could be included in a future picture of solar wind/magnetosphere coupling.

[150] 7. The freestream-turbulence effect in section 3.3 is based on an eddy-viscosity calculation that relies on a measure of the amplitude of the MHD turbulence in the upstream solar wind. For this amplitude, the RMS level of magnetic field-vector fluctuations δB_m measured in the solar wind was used. However, all of the magnetic field fluctuations in the solar wind are not turbulence: In addition to turbulent fluctuations there are also convected current sheets [*Bruno et al.*, 2007; *Borovsky*, 2008b; *Miao et al.*, 2011], steepened Alfven waves [*Vasquez and Hollweg*, 1999; *Tsurutani & Ho*, 1999; *Gosling et al.*, 2011], and other forms of tangential discontinuities [*Hollweg*, 1982; *Mariani et al.*, 1983; *Tu and Marsch*, 1995]. By taking the RMS level of magnetic field fluctuations δB_m, the amplitude of turbulence in the solar wind is probably substantially overestimated and the scalings of the turbulence amplitude with solar wind parameters may be incorrect. Developing a methodology to remove the signal of advected current sheets from the solar wind magnetic field time series to then more accurately measure the amplitude of true turbulence in the solar wind [cf. *Borovsky*, 2010b] could improve the accuracy of the freestream-turbulence driver $\mathscr{F}$.

6.2. Noise

[151] In the solar wind and geomagnetic data sets, there are sources of noise, i.e., sources of uncorrelated variations between the two data sets. Five examples follow:

[152] 1. There is error in the knowledge of the upstream solar wind conditions at Earth owed to the use of a solar wind monitor that is off the Sun-Earth line. The transverse correlation length for the magnetic structure of the solar wind is ~45 R_E [*Richardson and Paularena*, 2001] and upstream monitors are often farther than this length from the Sun-Earth line. Even if the upstream monitor were on the Sun-Earth line, the velocity vector of the solar wind varies by several degrees several times per hour [*Borovsky*, 2012b] so the sampled solar wind would not always hit the Earth. Temporal evolution of solar wind structure during the 30–80 min advection time between the upstream monitor and the Earth is another source of error in the knowledge of the solar parameters at Earth.

[153] 2. There are pitfalls to hourly averaging the solar wind measurements, particularly for the IMF clock angle θ_{clock} (see discussion of Figure 9), which is a sensitive parameter in the coupling functions.

[154] 3. The appropriateness of using geomagnetic indices as measures of the global coupling between the solar wind and the magnetosphere can be questioned [e.g., *Baumjohann*, 1986; *Kamide and Rostoker*, 2004]. The responses of geomagnetic indices may be nonlinear (cf. Figure 7 and section 4.2), and geomagnetic indices can respond to local phenomenon [*Liou et al.*, 2013] as well as to global phenomena.

[155] 4. There may be hysteresis in the behavior of the magnetosphere-ionosphere system wherein the state of the system not only depends on the recent history of the solar wind parameters but also depends on the recent history of the magnetosphere. An example of this is the preconditioning of the magnetosphere by long periods of geomagnetic calm that affects the way the magnetosphere responds to the solar wind [*Borovsky and Steinberg*, 2006b; *Borovsky and Denton*, 2013].

[156] 5. The magnetosphere, line tied to the resistive ionosphere, is a high-Reynolds-number system [*Borovsky and Funsten*, 2003b; *Borovsky and Denton*, 2008]. At high Reynolds numbers, no steady state solutions exist [*Feynman et al.*, 1964]. As such, the state of the system and any measurement in the system are irreproducible [*Tennekes and Lumley*, 1972]; consequently, for a given driving condition, the state of the magnetosphere will vary from realization to realization. The magnetosphere-ionosphere system can only be described statistically and there will always be a variance that cannot be predicted. The amplitude of that variance will depend on the timescale of the measurement and on an interplay between timescales of variation of the driver and the range of characteristic timescales of the system.

6.3. Most Immediate Improvements

[157] A significant advantage that the local control of reconnection rate picture has [cf. *Cassak and Shay*, 2007; *Borovsky and Hesse*, 2007] is that the mass density of the magnetospheric plasma can be included in the solar wind/magnetosphere coupling physics [cf. *Borovsky et al.*, 2008, 2013]. A next step in the improvement of physical solar wind driver functions for the magnetosphere is to include a parameterization of the mass density ρ_m of the dayside magnetosphere into the driver functions. This involves multiplying

the reconnection-coupled generator $\mathscr{G}$ by $(1+(\rho_m/\rho_{sw})C^{-1}[1+(M_A/6)^{1.92}]^{-1/2})^{-1/2}$ to correct for the fact that ρ_m was taken to be 0 in the denominator of the Cassak-Shay equation when the function R_2 (expression (3)) was derived. In this factor, ρ_{sw} is the mass density of the solar wind and C is the compression ratio of the bow shock (expression (4c)). Parameterization of ρ_m in terms of upstream solar wind conditions (and perhaps in terms of the time history of geomagnetic activity) is a priority.

[158] A critical lack of knowledge about reconnection is the effect of flow shear on asymmetric reconnection with a guide field. Via numerical simulations, a parametric study of the reconnection rate versus the magnitude of the velocity shear is needed, with the flow shear direction varied systematically (a) with respect to the direction of the magnetic field in the slow Alfven speed plasma, (b) with respect to the direction of the magnetic field in the fast Alfven speed plasma, and (c) with respect to the direction of the guide field. With the results of such a study, the length of the dayside X line could be better parameterized as functions of upstream solar wind parameters and in particular as a function of the IMF clock angle.

7. Summary

[159] Driver functions for the Earth's magnetosphere-ionosphere system were derived from physical principles, based on two processes acting simultaneously on the magnetosphere: a reconnection-coupled MHD generator $\mathscr{G}$ and a viscous interaction. Two possibilities for the physical processes dominating the viscous interaction were pursued, Bohm viscosity and the freestream-turbulence effect: This resulted in two viscous-interaction driver functions $\mathscr{B}$ and $\mathscr{T}$. The reconnection-coupled generator driver and a viscous driver were summed to form two combined solar wind driver functions: $\mathscr{G}+\mathscr{B}$ and $\mathscr{G}+\mathscr{T}$. The following is the summary of findings for the derivation, study, and testing of the solar wind driver functions:

[160] 1. A reconnection-coupled generator driver function $\mathscr{G}$ was derived based on the local control of the magnetic field line reconnection rate at the dayside magnetopause, on an estimate of the length of the dayside reconnection X line, and on current-saturation limits of the solar wind generator.

[161] 2. With the use of a series of global MHD computer simulations of the magnetosheath flow pattern for a large range of solar wind Mach numbers, an expression for the length of the dayside reconnection X line based on the cutoff of reconnection by flow shear at the magnetopause was derived.

[162] 3. A quality factor for the MHD generator of the solar wind was derived based on current-saturation physics for MHD generators operating in collisionless plasmas.

[163] 4. A Bohm-viscosity viscous driver function $\mathscr{B}$ was derived based on the properties of the shocked magnetosheath plasma flowing around the Earth's magnetosphere. A calculation of the viscosity led to a calculation of the flow Reynolds number which led to a calculation of the viscous drag on the magnetosphere.

[164] 5. A freestream-turbulence viscous driver function $\mathscr{T}$ was derived based on the amplification of solar wind magnetic field fluctuations and velocity fluctuations through the bow shock. The fluctuation amplitude in the magnetosheath led to a calculation of the eddy viscosity of the magnetosheath, which led to a flow Reynolds number, which led to a calculation of the viscous drag on the magnetosphere.

[165] 6. The correlations between the temporal behavior of the viscous driver functions $\mathscr{B}$ and $\mathscr{T}$ and the temporal behavior of seven geomagnetic indices were examined as function of the IMF clock angle. A proxy effect was uncovered wherein the viscous driver functions not only describe the strength of the viscous interaction but also describe the strength of the reconnection interaction between the solar wind and the magnetosphere. It is likely that the converse is also true, that the reconnection-coupled-generator function $\mathscr{G}$ also describes the strength of the viscous interaction.

[166] 7. Combined reconnection plus viscous driver functions were assembled. Two driver functions for the magnetosphere result: $\mathscr{G}+\mathscr{B}$ and $\mathscr{G}+\mathscr{T}$. Both are written in terms of solar parameters and upstream solar wind parameters.

[167] 8. The solar wind driver functions $\mathscr{G}+\mathscr{B}$ and $\mathscr{G}+\mathscr{T}$ were tested against seven geomagnetic indices using 1 h time resolution OMNI2 data for the solar wind parameters going into the driver functions.

[168] 9. The reaction of the geomagnetic indices to the solar wind driver functions $\mathscr{G}+\mathscr{B}$ and $\mathscr{G}+\mathscr{T}$ is nonlinear. Nonlinear fits between the driver functions and the *AE* and *Kp* indices were made and nonlinear versions of the solar wind driver functions $NL(\mathscr{G}+\mathscr{B})$ and $NL(\mathscr{G}+\mathscr{T})$ were supplied.

[169] 10. The $\mathscr{G}+\mathscr{B}$ and $\mathscr{G}+\mathscr{T}$ driver functions showed correlation coefficients of less than 80% with the seven geomagnetic indices. The nonlinear versions $NL(\mathscr{G}+\mathscr{B})$ and $NL(\mathscr{G}+\mathscr{T})$ of the driver functions showed correlation coefficients of approximately 80% with the *AE* and *Kp* indices.

[170] 11. Multiple time step solar wind driver functions were examined and correlation coefficients with the geomagnetic indices of approximately 85% resulted.

[171] 12. Visual inspection of the temporal plots of the solar wind driver functions $NL(\mathscr{G}+\mathscr{B})$ and $NL(\mathscr{G}+\mathscr{T})$ and of the *AE* index found that the driver functions do poorly at predicting localized peaks in the *AE* index.

[172] 13. Inspection of the time series of the driver functions $NL(\mathscr{G}+\mathscr{B})$ and $NL(\mathscr{G}+\mathscr{T})$ and the *AE* and *Kp* indices found that a signal with a 1 year periodicity occurs in the *AE* index that does not occur in the solar wind driver functions. Similarly, a semiannual variation is found in the *Kp* index that is not seen in the driver functions.

[173] 14. Autocorrelation functions of the solar wind driver functions $NL(\mathscr{G}+\mathscr{B})$ and $NL(\mathscr{G}+\mathscr{T})$, the *AE* index, and pertinent solar wind parameters were examined. It was found that the temporal persistence in the driver function time series was less than the persistence in the *AE* index time series. No single solar wind parameter had a temporal response similar to the temporal response of the driver functions.

[174] 15. The autocorrelation functions showed strong 1 day and 1 year periodicities in the *AE* index that are not in the solar wind driver functions.

[175] 16. The autocorrelation functions showed strong 27 day periodicities in the solar wind driver functions as in the *AE* index.

[176] 17. High-pass filtering and low-pass filtering of the driver functions $\mathscr{G}+\mathscr{B}$ and $\mathscr{G}+\mathscr{T}$ and of the *AE* index showed timescales of strongly correlated signal and timescales of noncorrelated signals. Twenty-seven day timescales were strongly correlated between the driver functions and the

AE index; few hours and 1 year timescales were poorly correlated between the drivers and the *AE* index.

[177] 18. Band-pass filtering the *AE* index and the *NL* ($\mathscr{G}+.\mathscr{B}$) driver function to remove variations with timescales shorter than 1 day and longer than 1 year resulted in an increase in the correlation coefficient between *NL* ($\mathscr{G}+.\mathscr{B}$) and *AE* to +0.916 from +0.812 for the unfiltered time series.

[178] 19. Multiple time step solar wind driver functions were examined with a computer code that optimized the time step weights to obtain the best correlations with geomagnetic indices. To describe the behavior of the *AE* index, solar wind driver functions with three time steps worked well, with the strongest weight on the time step 1 h prior to *AE*. For the *Kp* index, solar wind driver functions with 12 time steps worked well, with the weighting of the driver functions spread back in time at least 12 h.

[179] 20. It was argued that using multi-time step driver functions is equivalent to averaging the driver functions to remove high-frequency signal in the driver. Simple boxcar running averaging of the driver functions was found to always improve their ability to describe the variance of the geomagnetic indices. Optimal driver-averaging times could be a short as 2 h for some geomagnetic indices.

[180] 21. Improved driver functions that utilize boxcar running averages of the driver functions that did not require future values of solar wind parameters were explored: r_{corr} values of up to +0.832 with *AE* and up to +0.862 with *Kp* were obtained. For *AE*, the unaccounted for variance is $1 - r_{corr}^2 = 30.8\%$ and for *Kp* the unaccounted variance is $1 - r_{corr}^2 = 25.7\%$.

[181] 22. The residuals (also known as the errors or the unpredicted variance) between the measured geomagnetic indices and the predictions of the solar wind driver functions were analyzed. It was found that the residuals were anticorrelated with the solar wind velocity, anticorrelated with the solar $F_{10.7}$ radio flux, and anticorrelated with the solar wind current-saturation parameter. Although not physically justified, using adjustable tuning parameters on these three quantities could improve the performance of a future solar wind driving function.

[182] 23. Analysis of the residual errors finds annual and diurnal trends in *AE* and semiannual and diurnal trends in *Kp*. It is argued that the diurnal and annual trends in *AE* and the diurnal trends in *Kp* are not in the solar wind, rather they are properties intrinsic to those indices. Removal of those annual and diurnal trends from the *AE* and *Kp* indices improves the correlations between the solar wind drivers and the indices.

[183] 24. Simplified mathematical versions $\mathscr{D}_{\mathscr{G}+.\mathscr{B}}$ and $\mathscr{D}_{\mathscr{G}+.\mathscr{F}}$ of the solar wind driver functions $\mathscr{G}+.\mathscr{B}$ and $\mathscr{G}+.\mathscr{F}$ were constructed. It was found that the simplified drivers $\mathscr{D}_{\mathscr{G}+.\mathscr{B}}$ and $\mathscr{D}_{\mathscr{G}+.\mathscr{F}}$ perform approximately as well as the full drivers $\mathscr{G}+.\mathscr{B}$ and $\mathscr{G}+.\mathscr{F}$ do.

[184] 25. Physical processes that are missing from the derivations of the driver functions were discussed: The list of missing processes includes accounting for the mass density of the magnetospheric plasma (the plasmasphere effect), Kelvin-Helmholtz facilitated reconnection, reconnection behind the cusps, Kelvin-Helmholtz modulation of the viscous interaction, X line tilt effects, and the effects of the transfer of solar wind plasma into the magnetosphere.

[185] 26. Sources of errors and noise in the *AE* index and in the solar wind driver functions were discussed. Those sources include errors in the knowledge of the solar wind conditions at Earth, errors introduced by hourly averaging, questions about the validity of using geomagnetic indices as measures of the coupling of the solar wind to the magnetosphere, hysteresis in the behavior of the magnetosphere-ionosphere system, and unpredictable variance in the high-Reynolds-number magnetosphere-ionosphere system.

[186] 27. The improvements most critically needed for an advancement of the physics of the solar wind driver functions for the magnetosphere were deemed to be (1) a parameterization of the mass density of the dayside magnetosphere (which can substantially affect the dayside reconnection rate and hence affect the strength of the reconnection-coupled generator) and (2) a parametric study of the effects of flow shear on asymmetric reconnection with a guide field (which can lead to better parameterizations of the length of the dayside X line in terms of upstream-solar wind parameters).

[187] **Acknowledgments.** The author wishes to thank Derek Bingham, Joachim Birn, Paul Cassak, Michael Hesse, John Lyon, Bob McPherron, Antonius Otto, and Lutz Rastatter for their help. Global MHD simulations were performed at the CCMC. This work was supported at Space Science Institute by the NASA CCMSM-24 Program, the NSF GEM Program, and the NASA Geospace SR&T Program, at the University of Michigan by the NASA Geospace SR&T Program, and at the University of Lancaster by Science and Technology Funding Council grant ST/I000801/1.

[188] Philippa Browning thanks Michael Hesse and an anonymous reviewer for their assistance in evaluating this paper.

References

Ahn, B.-H., H. W. Kroehl, Y. Kamide, and E. A. Kihn (2000), Seasonal and solar cycle variations of the auroral electrojet indices, *J. Atmos. Sol. Terr. Phys.*, *62*, 1301.

Alfven, H., and C.-G. Falthammar (1963), *Cosmical Electrodynamics*, Oxford Univ. Press, New York.

Allen, J. H., and H. W. Kroehl (1975), Spatial and temporal distributions of magnetic effects of auroral electrojets as derived from *AE* indices, *J. Geophys. Res.*, *80*, 3667–3677.

Axford, W. I. (1964), Viscous interaction between the solar wind and the Earth's magnetosphere, *Planet. Space Sci.*, *12*, 45.

Axford, W. I. (1969), Magnetospheric convection, *Rev. Geophys.*, *7*, 421.

Baker, D. N. (1986), Statistical analyses in the study of solar wind-magnetosphere coupling, in *Solar Wind-Magnetosphere Coupling*, edited by Y. Kamide and J. A. Slavin, p. 17, Terra Scientific, Tokyo.

Baker, D. N., E. W. Hones, J. B. Payne, and W. C. Feldman (1981), A high time resolution study of interplanetary parameter correlations with *AE*, *Geophys. Res. Lett.*, *8*, 179–182.

Balikhin, M. A., R. J. Boynton, S. A. Billings, M. Gadalin, N. Ganushkina, D. Coca, and H. Wei (2010), Data based quest for solar wind-magnetosphere coupling function, *Geophys. Res. Lett.*, *37*, L24107, doi:10.1029/2010GL045733.

Baumjohann, W. (1986), Merits and limitations of the use of geomagnetic indices in solar wind-magnetosphere coupling studies, in *Solar Wind-Magnetosphere Coupling*, edited by Y. Kamide and J. A. Slavin, p. 3, Terra Scientific, Tokyo.

Belcher, J. W., and L. Davis (1971), Large-amplitude Alfven waves in the interplanetary medium, 2, *J. Geophys. Res.*, *76*, 3534–3563.

Bellaire, P. J. (2006), Community Coordinated Modeling Center 2005 Workshop report, *Space Weather*, *4*, S02004, doi:10.1029/2005SW000206.

Bendat, J. S., and A. G. Piersol (1971), *Random Data: Analysis and Measurement Procedures, Sect. 4.8.1*, John Wiley, New York.

Bevington, P. R., and D. K. Robinson (1992), *Data Reduction and Error Analysis for the Physical Sciences*, 2nd ed., McGraw-Hill, New York.

Beyer, W. H. (Ed) (1966), *Handbook of Tables for Probability and Statistics, Sect. IX*, Chem. Rubber, Cleveland, Ohio.

Birn, J., J. E. Borovsky, and M. Hesse (2008), Properties of asymmetric magnetic reconnection, *Phys. Plasmas*, *15*, 032101.

Birn, J., J. E. Borovsky, M. Hesse, and K. Schindler (2010), Scaling of asymmetric reconnection in compressible plasmas, *Phys. Plasmas*, *17*, 052108.

Birn, J., J. E. Borovsky, and M. Hesse (2012), The role of compressibility in energy release by magnetic reconnection, *Phys. Plasmas*, *19*, 082109.

Blair, M. F. (1983), Influence of free-stream turbulence on turbulent boundary layer heat transfer and mean profile development part 1: Experimental data, *J. Heat Transf.*, *105*, 33.

Bohm, D., E. H. S. Burhop, and H. S. W. Massey (1949), The use of probes for plasma exploration in strong magnetic fields, in *The Characteristics of Electrical Discharges in Magnetic Fields*, edited by A. Guthrie and R. K. Wakerling, pp. 13, McGraw-Hill, New York.

Borovsky, J. E. (2006), Eddy viscosity and flow properties of the solar wind: Co-rotating interaction regions, coronal-mass-ejection sheaths, and solar wind/magnetosphere coupling, *Phys. Plasmas*, *13*, 056505.

Borovsky, J. E. (2008a), The rudiments of a theory of solar wind/magnetosphere coupling derived from first principles, *J. Geophys. Res.*, *113*, A08228, doi:10.1029/2007JA012646.

Borovsky, J. E. (2008b), The flux-tube texture of the solar wind: Strands of the magnetic carpet at 1 AU?, *J. Geophys. Res.*, *113*, A08110, doi:10.1029/2007JA012684.

Borovsky, J. E. (2010a), On the variations of the solar wind magnetic field about the Parker-spiral direction, *J. Geophys. Res.*, *115*, A09101, doi:10.1029/2009JA015040.

Borovsky, J. E. (2010b), On the contribution of strong discontinuities to the power spectrum of the solar wind, *Phys. Rev. Lett.*, *105*, 111102.

Borovsky, J. E. (2012a), The velocity and magnetic-field fluctuations of the solar wind at 1 AU: Statistical analysis of Fourier spectra and correlations with plasma properties, *J. Geophys. Res.*, *117*, A05104, doi:10.1029/2011JA017499.

Borovsky, J. E. (2012b), The effect of sudden wind shear on the Earth's magnetosphere: Statistics of wind-shear events and CCMC simulations of magnetotail disconnections, *J. Geophys. Res.*, *117*, A06224, doi:10.1029/2012JA017623.

Borovsky, J. E. (2013), Physical improvements to the solar wind reconnection control function for the Earth's magnetosphere, *J. Geophys. Res. Space Physics*, *118*, 2113–2121, doi:10.1002/jgra.50110.

Borovsky, J. E., and M. H. Denton (2006), The differences between CME-driven storms and CIR-driven storms, *J. Geophys. Res.*, *111*, A07S08, doi:10.1029/2005JA011447.

Borovsky, J. E., and M. H. Denton (2008), A statistical look at plasmaspheric drainage plumes, *J. Geophys. Res.*, *113*, A09221, doi:10.1029/2007JA012994.

Borovsky, J. E., and M. H. Denton (2010a), The magnetic field at geosynchronous orbit during high-speed-stream-driven storms: Connections to the solar wind, the plasma sheet, and the outer electron radiation belt, *J. Geophys. Res.*, *115*, A08217, doi:10.1029/2009JA015116.

Borovsky, J. E., and M. H. Denton (2010b), Solar-wind turbulence and shear: A superposed-epoch analysis of corotating interaction regions at 1 AU, *J. Geophys. Res.*, *115*, A10101, doi:10.1029/2009JA014966.

Borovsky, J. E., and M. H. Denton (2013), The differences between storms driven by helmet-streamer CIRs and storms driven by pseudostreamer CIRs, *J. Geophys. Res. Space Physics*, *118*, doi:10.1002/jgra.50524.

Borovsky, J. E., and H. O. Funsten (2003a), The role of solar wind turbulence in the coupling of the solar wind to the Earth's magnetosphere, *J. Geophys. Res.*, *108*(A6), 1246, doi:10.1029/2002JA009601.

Borovsky, J. E., and H. O. Funsten (2003b), MHD turbulence in the Earth's plasma sheet: Dynamics, dissipation, and driving, *J. Geophys. Res.*, *108*(A7), 1284, doi:10.1029/2002JA009625.

Borovsky, J. E., and S. P. Gary (2009), On viscosity and the Reynolds number of MHD turbulence in collisionless plasmas: Coulomb collisions, Landau damping, and Bohm diffusion, *Phys. Plasmas*, *16*, 082307.

Borovsky, J. E., and M. Hesse (2007), The reconnection of magnetic fields between plasmas with different densities: Scaling relations, *Phys. Plasmas*, *14*, 102309.

Borovsky, J. E., and J. T. Gosling (2001), The level of turbulence in the solar wind and the driving of the Earth's magnetosphere, *Eos Trans. Amer. Geophys. Soc.*, *82*(20), S368.

Borovsky, J. E., and J. T. Steinberg (2006a), The freestream turbulence effect in solar wind/magnetosphere coupling: Analysis through the solar cycle and for various types of solar wind, in *Recurrent Magnetic Storms: Cororating Solar Wind Streams*, p. 59, American Geophysical Union, Washington, D.C.

Borovsky, J. E., and J. T. Steinberg (2006b), The "calm before the storm" in CIR/magnetosphere interactions: Occurrence statistics, solar wind statistics, and magnetospheric preconditioning, *J. Geophys. Res.*, *111*, A07S10, doi:10.1029/2005JA011397.

Borovsky, J. E., M. F. Thomsen, and R. C. Elphic (1998), The driving of the plasma sheet by the solar wind, *J. Geophys. Res.*, *103*, 17,617–17,639.

Borovsky, J. E., M. Hesse, J. Birn, and M. M. Kuznetsova (2008), What determines the reconnection rate at the dayside magnetosphere?, *J. Geophys. Res.*, *113*, A07210, doi:10.1029/2007JA012645.

Borovsky, J. E., B. Lavraud, and M. M. Kuznetsova (2009), Polar cap potential saturation, dayside reconnection, and changes to the magnetosphere, *J. Geophys. Res.*, *114*, A03224, doi:10.1029/2009JA014058.

Borovsky, J. E., M. H. Denton, R. E. Denton, V. K. Jordanova, and J. Krall (2013), Estimating the effects of ionospheric plasma on solar wind/magnetosphere coupling via mass loading of dayside reconnection: Ion-plasma-sheet oxygen, plasmaspheric drainage plumes, and the plasma cloak, *J. Geophys. Res. Space Physics*, doi:10.1002/jgra.50527.

Boynton, R. J., M. A. Balikhin, S. A. Billings, H. L. Wei, and N. Ganushkina (2011), Using the NARMAX OLS-ERR algorithm to obtain the most influential coupling functions that affect the evolution of the magnetosphere, *J. Geophys. Res.*, *116*, A05218, doi:10.1029/2010JA015505.

Braginskii, S. I. (1965), in *Reviews of Plasma Physics*, edited by M. A. Leontovich, pp. 205, Consultants Bureau, New York.

Bruno, R., R. D. D'Amicis, B. Bavassano, V. Carbone, and L. Sorriso-Valvo (2007), Magnetically dominated structures as an important component of the solar wind turbulence, *Ann. Geophys.*, *25*, 1913.

Cassak, P. A., and A. Otto (2011), Scaling of the magnetic reconnection rate with symmetric shear flow, *Phys. Fluids*, *18*, 074501.

Cassak, P. A., and M. A. Shay (2007), Scaling of asymmetric magnetic reconnection: General theory and collisional simulations, *Phys. Plasmas*, *14*, 102114.

Castro, I. P., and A. G. Robins (1977), The flow around a surface-mounted cube in uniform and turbulent streams, *J. Fluid Mech.*, *79*, 307.

Chen, Q., A. Otto, and L. C. Lee (1997), Tearing instability, Kelvin-Helmholtz instability, and magnetic reconnection, *J. Geophys. Res.*, *102*, 151.

Cliver, E. W., Y. Kamide, and A. G. Ling (2000), Mountains versus valleys: Semiannual variation of geomagnetic indices, *J. Geophys. Res.*, *105*, 2413–2424.

Courchesne, J., and A. Laneville (1982), An experimental evaluation of drag coefficients for rectangular cylinders exposed to grid turbulence, *J. Fluids Engin.*, *104*, 523.

D'Amicis, R., R. Bruno, and B. Bavassano (2007), Is geomagnetic activity driven by solar wind turbulence?, *Geophys. Res. Lett.*, *34*, L05108, doi:10.1029/2006GL028896.

D'Amicis, R., R. Bruno, and B. Bavassano (2009), Alfvenic turbulence in high speed solar wind steams as a driver for auroral activity, *J. Atmos. Sol. Terr. Phys.*, *71*, 1014.

D'Amicis, R., R. Bruno, and B. Bavassano (2010), Geomagnetic activity driven by solar wind turbulence, *Adv. Space Res.*, *46*, 514.

D'Amicis, R., R. Bruno, and B. Bavassano (2011), Response of the geomagnetic activity to solar wind turbulence during solar cycle 23, *J. Atmos. Sol. Terr. Phys.*, *73*, 653.

Denton, M. H., and J. E. Borovsky (2009), The superdense plasma sheet in the magnetosphere during high-speed-steam-driven storms: Plasma transport timescales, *J. Atmos. Sol. Terr. Phys.*, *71*, 1045.

De Zeeuw, D. L., T. I. Gombosi, C. P. T. Groth, K. G. Powell, and Q. F. Stout (2000), An adaptive MHD method for global space weather simulations, *IE Trans. Plasma Sci.*, *28*, 1956.

Dobrowolny, M., A. Mangeney, and P. Veltri (1980), Fully developed anisotropic turbulence in interplanetary space, *Phys. Rev. Lett.*, *45*, 144.

Dungey, J. W. (1961), Interplanetary magnetic field and the auroral zones, *Phys. Rev. Lett.*, *6*, 47.

Eckert, H. U. (1950), Characteristics of the turbulent boundary layer on a flat plate in compressible flow from measurement of friction in pipes, *J. Aeron. Sci.*, *17*, 573.

Eviatar, A., and R. A. Wolf (1968), Transfer processes in the magnetopause, *J. Geophys. Res.*, *73*, 5561.

Faber, T. E. (1995), *Fluid Dynamics for Physicists, Sect. 7.8*, Cambridge Univ. Press, Cambridge, U. K.

Farrugia, C. J., F. T. Gratton, and R. B. Torbert (2001), Viscous-type processes in the solar wind wind-magmnetosphere interaction, *Space Sci. Rev.*, *95*, 443.

Farrugia, C. J., and F. T. Gratton (2011), Aspects of magnetopause response to interplanetary discontinuities, and features of magnetopause Kelvin-Helmholtz waves, *J. Atmos. Sol. Terr. Phys.*, *73*, 40.

Feynman, R. P., R. B. Leighton, and M. Sands (1964), *Lectures on Physics, Sect. 41–4*, Addison-Wesley, Reading, Mass.

Fejer, J. A. (1964), Hydromagnetic stability at a fluid velocity discontinuity between compressible fluids, *Phys. Fluids*, *7*, 499.

Finch, I., and M. Lockwood (2007), Solar wind-magnetosphere coupling functions on timescales of 1 day to 1 year, *Ann. Geophys.*, *25*, 495.

Fung, S. F., and X. Shao (2008), Specification of multiple geomagnetic responses to variable solar wind and IMF input, *Ann. Geophys.*, *26*, 639.

Gao, Y., M. G. Kivelson, and R. J. Walker (2012), The linear dependence of polar cap index on its controlling factors in solar wind and magnetotail, *J. Geophys. Res.*, *117*, A05213, doi:10.1029/2011JA017229.

Gary, S. P., and J. E. Borovsky (2004), Alfven-cyclotron fluctuations: Linear Vlasov theory, *J. Geophys. Res.*, *109*, A06105, doi:10.1029/2004JA010399.

Goertz, C. K., L.-H. Shan, and R. A. Smith (1993), Prediction of geomagnetic activity, *J. Geophys. Res.*, *98*, 7673–7684.

Gonzalez, W. D. (1990), A unified view of solar wind-magnetosphere coupling functions, *Planet. Space Sci.*, *38*, 627.

Gosling, J. T., D. N. Baker, S. J. Bame, W. C. Feldman, R. D. Zwickl, and E. J. Smith (1987), Bidirectional solar wind electron heat flux events, *J. Geophys. Res.*, *92*, 8519–8535.

Gosling, J. T., M. F. Thomsen, S. J. Bame, R. C. Elphic, and C. T. Russell (1991), Observations of reconnection of interplanetary and lobe magnetic field lines, *J. Geophys. Res.*, *96*, 14,097–14,106.

Gosling, J. T., H. Tian, and T. D. Phan (2011), Pulsed Alfven waves in the solar wind, *Astrophys. J. Lett.*, *737*, L35.

Guo, J., X. Feng, B. A. Emery, and Y. Wang (2012), Efficiency of solar wind energy coupling to the ionosphere, *J. Geophys. Res.*, *117*, A07303, doi:10.1029/2012JA017627.

Gussenhoven, M. S., D. A. Hardy, and N. Heinemann (1983), Systematics of the equatorward diffuse auroral boundary, *J. Geophys. Res.*, *88*, 5692–5708.

Hibberd, F. H. (1985), The geomagnetic Sq variation—Annual, semi-annual and solar cycle variations and ring current effects, *J. Atmos. Sol. Terr. Phys.*, *47*, 341.

Hill, F. K. (1956), Boundary-layer measurements in hypersonic flow, *J. Aeron. Sci.*, *23*, 35.

Hill, T. W., A. Dessler, and R. A. Wolf (1976), Mercury and Mars: The role of ionospheric conductivity in the acceleration of magnetospheric particles, *Geophys. Res. Lett.*, *3*, 429–432.

Hoerner, S. F. (1965), *Fluid-Dynamic Drag*, Hoerner Fluid Dynamics, Brick Town, N. J.

Hoffmann, J. A. (1991), Effects of freestream turbulence on the performance characteristics of an airfoil, *AIAA J.*, *29*, 1353.

Hoffmann, J. A., and K. Mohammadi (1991), Velocity profiles for turbulent boundary layers under freestream turbulence, *J. Fluids Engin.*, *113*, 399.

Hollweg, J. V. (1982), Surface waves on solar wind tangential discontinuities, *J. Geophys. Res.*, *87*, 8065–8076.

Horbury, T., M. Forman, and S. Oughton (2008), Anisotropic scaling of magnetohydrodynamic turbulence, *Phys. Rev. Lett.*, *101*, 175005.

Huang, R. F., and H. W. Lee (2000), Turbulence effect on frequency characteristics of unsteady motions in wake of wing, *AIAA J.*, *38*, 87.

Ip, W.-H., and J. F. McKenzie (1991), Alfven wave amplifications and generation at cometary bow shocks, *Planet. Space Sci.*, *39*, 1045.

Johnson, J. R., and C. Z. Cheng (1997), Kinetic Alfven waves and plasma transport at the magnetopause, *Geophys. Res. Lett.*, *24*, 1423–1426.

Kamide, Y., and G. Rostoker (2004), What is the physical meaning of the *AE* index?, *Eos Trans. Amer. Geophys. Union*, *85*(19), 188.

Kaufman, A. N. (1960), Plasma viscosity in a magnetic field, *Phys. Fluids*, *3*, 610.

Kim, H.-J., L. Lyons, A. Boudouridis, V. Pilipenko, A. J. Ridley, and J. M. Weygand (2011), Statistical study of the effect of ULF fluctuations in the IM on the cross polar cap potential drop for northward IMF, *J. Geophys. Res.*, *116*, A10311, doi:10.1029/2011JA016931.

King, J. H., and N. E. Papitashvili (2005), Solar wind spatial scales in and comparisons of hourly Wind and ACE plasma and magnetic field data, *J. Geophys. Res.*, *110*, A02104, doi:10.1029/2004JA010649.

Kivelson, M. G., and A. Ridley (2008), Saturation of the polar cap potential: Inference from Alfven wing arguments, *J. Geophys. Res.*, *113*, A05214, doi:10.1029/2007JA012302.

Kuznetsova, M. M., M. Hesse, L. Rastatter, A. Taktakishvili, G. Toth, D. L. DeZeeuw, A. Ridley, and T. I. Gombosi (2007), Multiscale modeling of magnetospheric reconnection, *J. Geophys. Res.*, *112*, A10210, doi:10.1029/2007JA012316.

Ko, S. C., and W. H. Graf (1972), Drag coefficient of cylinders in turbulent flow, *J. Hydralics Div. ASCE*, *98*, 897.

Kwok, K. C. S., and W. H. Melbourne (1980), Freestream turbulence effects on galloping, *ASCE J. Engin. Mech. Div.*, *106*, 273.

LaBelle, J., and R. A. Treumann (1988), Plasma waves at the dayside magnetopause, *Space Sci. Rev.*, *47*, 175.

La Belle-Hamer, A. L., A. Otto, and L. C. Lee (1994), Magnetic reconnection in the presence of sheared plasma flow: Intermediate shock formation, *Phys. Plasmas*, *1*, 706.

Lavraud, B., and J. E. Borovsky (2008), Altered solar wind-magnetosphere interaction at low Mach numbers: Coronal mass ejections, *J. Geophys. Res.*, *113*, A00B08, doi:10.1029/2008JA013192.

Lavraud, B., M. F. Thomsen, J. E. Borovsky, M. H. Denton, and T. I. Pulkkinen (2006), Magnetosphere preconditioning under northward IMF: Evidence from the study of coronal mass ejection and corotating interaction region geoeffectiveness, *J. Geophys. Res.*, *111*, A09208, doi:10.1029/2005JA011566.

Lavraud, B., J. E. Borovsky, A. J. Ridley, E. W. Pogue, M. F. Thomsen, H. Reme, A. N. Fazakerley, and E. A. Lucek (2007), Strong bulk plasma acceleration in Earth's magnetosheath: A magnetic slingshot effect?, *Geophys. Res. Lett*, *34*, L14102, doi:10.1029/2007GL030024.

Lepping, R. P., C.-C. Wu, and D. B. Berdichevsky (2005), Automated identification of magnetic clouds and cloud-like regions at 1 AU: Occurrence rate and other properties, *Ann. Geophys.*, *23*, 2687.

Liou, K., K. Takahashi, B. J. Anderson, M. Nose, and T. Iyemori (2013), Assessment of the auroral electrojet index performance under various geomagnetic conditions, *J. Atmos. Sol. Terr. Phys.*, *92*, 31.

Lobb, R. K., E. M. Winkler, and J. Persh (1955), Experimental investigation of turbulent boundary layers in hypersonic flow, *J. Aeron. Sci.*, *22*, 1.

Lopez, R. E., V. G. Merkin, and J. G. Lyon (2011), The role of the bow shock in solar wind-magnetosphere coupling, *Ann. Geophys.*, *29*, 1129.

Luo, H., G. X. Chan, A. M. Du, and W. Y. Xu (2013), Solar wind dependence of energy coupling between solar wind and magnetosphere during intense northward IMFs, *Planet. Space Sci.*, *79–80*, 82.

Lyatsky, W., P. T. Newell, and A. Hamza (2001), Solar illumination as cause of the equinoctial preference for geomagnetic activity, *Geophys. Res. Lett.*, *28*, 2353.

Lyon, J. G., J. A. Fedder, and C. M. Mobarry (2004), The Lyon-Fedder-Mobarry (LFM) global MHD magnetospheric simulation code, *J. Atmos. Sol. Terr. Phys.*, *66*, 1333.

Lyons, L. R., et al. (2009), Evidence that solar wind fluctuations substantially affect global convection and substorm occurrence, *J. Geophys. Res.*, *114*, A11306, doi:10.1029/2009JA014281.

Lysak, R. L. (1990), Electrodynamic coupling of the magnetosphere and ionosphere, *Space Sci. Rev.*, *52*, 33.

Mallinkrodt, A. J., and C. W. Carlson (1978), Relations between transverse electric fields and field-aligned currents, *J. Geophys. Res.*, *83*, 1426–1432.

Mariani, F. B., B. Bavassano, and U. Villante (1983), A statistical study of MHD discontinuities in the inner solar system: Helios 1 and 2, *Solar Phys.*, *83*, 349.

Marsch, E., and C.-Y. Tu (1990), On the radial evolution of MHD turbulence in the inner heliosphere, *J. Geophys. Res.*, *95*, 8211.

McIntosh, D. H. (1959), On the annual variation of magnetic disturbance, *Phil. Trans. Roy. Soc. Lond. Ser. A.*, *251*, 525.

McPherron, R. L., D. N. Baker, T. I. Pulkkinen, T.-S. Hsu, J. Kissinger, and X. Chu (2013), Changes in solar wind-magnetosphere coupling with solar cycle, season, and time relative to stream interfaces, *J. Atmos. Sol. Terr. Phys.*, *99*, 1.

Miao, B., B. Peng, and G. Li (2011), Current sheets from Ulysses observation, *Ann. Geophys.*, *29*, 237.

Milan, S. E., J. S. Gosling, and B. Hubert (2012), Relationship between interplanetary parameters and the magnetopause reconnection rate quantified from observations of the expanded polar cap, *J. Geophys. Res.*, *117*, A03226, doi:10.1029/2011JA017082.

Mitchell, H. G., and J. R. Kan (1978), Merging of magnetic fields with field-aligned plasma flow components, *J. Plasma Phys.*, *20*, 31.

Miura, A. (1984), Anomalous transport by magnetohydrodynamic Kelven-Helmholtz instabilities in the soalr wind-magnetosphere interaction, *J. Geophys. Res.*, *89*, 801.

Mozer, F. S. (1984), Electric field evidence on the viscous interaction at the magnetopause, *Geophys. Res. Lett.*, *11*, 135.

Mozer, F. S., H. Hayakawa, S. Kokubun, M. Nadamura, T. Odada, T. Yamamoto, and K. Tsuruda (1994), The morningside low-latitude boundary layer as determined from electric and magnetic field measurements on Geotail, *Geophys. Res. Lett.*, *21*, 2983–2986.

Murayama, T. (1974), Origin of the semiannual variation of geomagnetic *Kp* indies, *J. Geophys. Res.*, *79*, 297.

Nakamura, T. K. M., M. Fujimoto, and A. Otto (2006), Magnetic reconnection induced by weak Kelvin-Helmholtz instability and the formation of the low-latitude boundary layer, *Geophys. Res. Lett.*, *33*, L14106, doi:10.1029/2006GL026318.

Nakayama, Y., and R. F. Boucher (1999), *Introduction to Fluid Mechanics, Sect. 4.5*, Arnold, London.

Newell, P. T., T. Sotirelis, K. Liou, C.-I. Meng, and F. J. Rich (2007), A nearly universal solar wind-magnetosphere coupling function inferred from 10 magnetospheric state variables, *J. Geophys. Res.*, *112*, A01206, doi:10.1029/2006JA012015.

Newell, P. T., T. Sotirelis, K. Liou, and F. J. Rich (2008), Pairs of solar wind-magnetosphere coupling functions: Combining a merging term with a viscous term works best, *J. Geophys. Res.*, *113*, A04218, doi:10.1029/2007JA012825.

Nykyri, K., and A. Otto (2001), Plasma transport at the magnetospheric boundary due to reconnection in Kelvin-Helmholtz vortices, *Geophys. Res. Lett.*, *28*, 3565–3568.

Ober, D. M., N. C. Maynard, and W. J. Burke (2003), Testing the Hill model of transpolar potential saturation, *J. Geophys. Res.*, *108*(A12), 1467, doi:10.1029/2003JA010154.

Pal, S. (1985), Freestream turbulence effects on wake properties of a flat plate at an incidence, *AIAA J.*, *23*, 1868.

Parker, E. N. (1979), *Cosmical Magnetic Fields, Sects. 15.6 and 15.7*, Clarendon Press, Oxford, U. K.

Perez, J. C., and S. Boldyrev (2010), Numerical simulations of imbalanced strong magnetohydrodynamic turbulence, *Astrophys. J. Lett.*, *710*, L63.

Podesta, J. J. (2009), Dependence of solar wind power spectra on the direction of the local mean magnetic field, *Astrophys. J.*, *698*, 986.

Podesta, J. J., and J. M. TenBarge (2012), Scale dependence of the variance anisotropy near the proton gyroradius scale: Additional evidence for kinetic Alfven waves in the solar wind at 1 AU, *J. Geophys. Res.*, *117*, A10106, doi:10.1029/2012JA017724.

Podesta, J. J., D. A. Roberts, and M. L. Goldstein (2006), Power spectrum of small-scale turbulent velocity fluctuations in the solar wind, *J. Geophys. Res.*, *111*, A10109, doi:10.1029/2006JA011834.

Rastatter, L., M. M. Kuznetsova, D. G. Sibeck, and D. H. Berrios (2012), Scientific visualization to study flux transfer events at the Community Coordinated Modeling Center, *Adv. Space Res.*, *49*, 1623.

Reiff, P. H., R. W. Spiro, and T. W. Hill (1981), Dependence of polar cap potential drop on interplanetary parameters, *J. Geophys. Res.*, *86*, 7639–7648.

Reiff, P. H., and J. G. Luhmann (1986), Solar wind control of the polar-cap voltage, in *Solar Wind-Magnetosphere Coupling*, edited by Y. Kamide and J. A. Slavin, pp. 453, Terra Scientific, Tokyo.

Richardson, J. D., and K. I. Paularena (2001), Plasma and magnetic field correlations in the solar wind, *J. Geophys. Res.*, *106*, 239–251.

Ridley, A. J. (2007), Alfven wings at Earth's magnetosphere under strong interplanetary magnetic fields, *Ann. Geophys.*, *25*, 533.

Ridley, A. J., T. I. Gombosi, I. V. Sokolov, G. Toth, and D. T. Welling (2010), Numerical considerations in simulating the global magnetosphere, *Ann. Geophys.*, *28*, 1589.

Rostoker, G. (1972), Geomagnetic indices, *Rev. Geophys. Space Phys.*, *10*, 935.

Rucker, H. O., and K. J. Trattner (1991), Solar wind-terrestrial magnetosphere coupling: Application of linear prediction theory, *J. Atmos. Sol. Terr. Phys.*, *53*, 1069.

Russell, C. T., and R. L. McPherron (1973), Semiannual variation of geomagnetic activity, *J. Geophys. Res.*, *78*, 92.

Rynn, N. (1964), Classical and enhanced diffusion in cesium and potassium plasmas, *Phys. Fluids*, *7*, 1084.

Saathoff, P., and W. H. Melbourne (1999), Effects of freestream turbulence on streamwise pressure measured on a square-section cylinder, *J. Wind Engin. Industr. Aerodyn.*, *79*, 61.

Scholten, J. W., and D. B. Murray (1998), Unsteady heat transfer and velocity of a cylinder in cross flow—II. High freestream turbulence, *Int. J. Heat Mass Tranfer*, *41*, 1149.

Singh, Y. P., and Badruddin (2012), Study of the influence of magnetic fluctuations and solar plasma density on the solar wind-magnetosphere coupling, *J. Atmos. Sol. Terr. Phys.*, *75–76*, 15.

Siscoe, G., J. Rader, and A. J. Ridley (2004), Transpolar potential saturation models compared, *J. Geophys. Res.*, *109*, A09203, doi:10.1029/2003JA010318.

Siscoe, G., and D. Intriligator (1993), Three views of two giant streams: Aligned observations at 1 AU, 4.6 AU, and 5.9 AU, *Geophys. Res. Lett.*, *20*, 2267–2270.

Smith, J. P., M. F. Thomsen, J. E. Borovsky, and M. Collier (1999), Solar wind density as a driver for the ring current in mild storms, *Geophys. Res. Lett.*, *26*, 1797–1800.

Song, P., D. L. DeZeeuw, T. I. Gombosi, C. P. T. Groth, and K. G. Powell (1999), A numerical study of solar wind-magnetosphere interaction for northward interplanetary magnetic field, *J. Geophys. Res.*, *104*, 28,361–28,378.

Sonnerup, B. U. O. (1974), Magnetopause reconnection rate, *J. Geophys. Res.*, *79*, 1546–1549.

Sullerey, R. K., and M. A. S. Khan (1983), Freestream turbulence effects on compressor cascade wake, *J. Aircraft*, *20*, 733.

Swisdak, M., and J. F. Drake (2007), Orientation of the reconnection X line, *Geophys. Res. Lett.*, *34*, L11106, doi:10.1029/2007GL029815.

Takahashi, K., R. E. Denton, and H. J. Singer (2010), Solar cycle variation of geosynchronous plasma mass density derived from the frequency of standing Alfven waves, *J. Geophys. Res.*, *115*, A07207, doi:10.1029/2009JA015243.

Taroni, A., M. Erba, E. Springmann, and F. Tibone (1994), Global and local energy confinement properties of simple transport coefficients of the Bohm type, *Plasma Phys. Control. Fusion*, *36*, 1629.

Tennekes, H., and J. L. Lumley (1972), *A First Course in Turbulence, Sect. 1.1*, MIT Press, Cambridge, Mass.

Thole, K. A., and D. G. Bogard (1996), High freestream turbulence effects on turbulent boundary layers, *J. Fluids Engin.*, *118*, 276.

Tritton, D. J. (1977), *Physical Fluid Dynamics*, Reinhold, Berkshire, U. K.

Troshichev, O. A., R. Y. Lukianova, V. O. Papitashvili, F. J. Rich, and O. Rasmussen (2000), Polar cap index (PC) as a proxy for ionospheric electric field in the near-pole region, *Geophys. Res. Lett.*, *27*, 3809–3812.

Tsurutani, B. T., and W. D. Gonzalez (1995), The efficiency of "viscous interaction" between the solar wind and the magnetosphere during intense northward IMF events, *Geophys. Res. Lett.*, *22*, 663–666.

Tsurutani, B. T., and C. M. Ho (1999), A review of discontinuities and Alfven waves in interplanetary space: ULYSSES results, *Rev. Geophys.*, *37*, 517–541.

Tu, C.-Y., and E. Marsch (1995), MHD structures, waves and turbulence in the solar wind, *Space Sci. Rev.*, *73*, 1.

Vasquez, B. J., and J. V. Hollweg (1999), Formation of pressure-balanced structures and fast waves from nonlinear Alfven waves, *J. Geophys. Res.*, *104*, 4681–4696.

Vasyliunas, V. M., J. R. Kan, G. L. Siscoe, and S.-I. Akasofu (1982), Scaling relations governing magnetospheric energy transfer, *Planet. Space Sci.*, *30*, 359.

Volino, R. J. (1998), A new model for free-stream turbulence effects on boundary layers, *J. Turbomach.*, *120*, 613.

Volino, R. J., M. P. Schultz, and C. M. Pratt (2003), Conditional sampling in a transitional boundary layer under high freestream turbulence conditions, *J. Fluids Engin.*, *125*, 28.

Walker, R. J., and C. T. Russell (1995), Solar-wind interactions with magnetized planets, in *Introduction to Space Physics*, edited by M. G. Kivelson and C. T. Russell, pg. 164, Cambridge Univ. Press, New York.

Walters, G. K. (1964), Effect of oblique interplanetary magnetic field on shape and behavior of the magnetosphere, *J. Geophys. Res.*, *69*, 1769–1783.

Wang, Y.-M., R. Grappin, E. Robbecht, and N. R. Sheeley (2012), On the nature of the solar wind from coronal pseudostreamers, *Astrophys. J.*, *749*, 182.

Weimer, D. R., L. A. Reinleitner, J. R. Kan, and S.-I. Akasofu (1990), Saturation of the auroral electrojet current and the polar cap potential, *J. Geophys. Res.*, *95*, 18,981–18,987.

Wiltberger, M., R. E. Lopez, and J. G. Lyon (2005), Results from magnetospheric Gedanken experiments using the LFM, *Adv. Space Res.*, *36*, 1797.

Wu, J.-S., and G. M. Faeth (1994), Sphere wakes at moderate Reynolds numbers in a turbulent environment, *AIAA J.*, *32*, 535.

Wygant, J. R., R. B. Torbert, and F. S. Mozer (1983), Comparison of S3-3 polar cap potential drops with the interplanetary magnetic field and models of magnetopause reconnection, *J. Geophys. Res.*, *88*, 5727–5735.

Yoshizawa, A., and N. Yokoi (1996), Stationary large-scale magnetic fields generated by turbulent motion in a spherical region, *Phys. Plasmas*, *3*, 3604.

Zhang, X., L. J. Li, L. C. Wang, J. H. Li, and Z. W. Ma (2011), Influences of sub-Alfvenic shear flows on nonlinear evolution of magnetic reconnection in compressible plasmas, *Phys. Plasmas*, *18*, 092,112.

Zhao, L., T. H. Zurbuchen, and L. A. Fisk (2009), Global distribution of the solar wind during solar cycle 23: ACE observations, *Geophys. Res. Lett.*, *36*, L14104, doi:10.1029/2009GL039181.